Department of Physics and Astronomy

University of Heidelberg

Diploma thesis

in Physics

submitted by

Michael Schönwald

born in Ottweiler (Saar)

September 2010

Phase-matched few-cycle high-harmonic generation:
ionisation gating and half-cycle cutoffs

This diploma thesis has been carried out by Michael Schönwald

at the

Max-Planck Institut für Kernphysik

under the supervision of

Dr. Thomas Pfeifer

(Ionisations-beschränkte, phasenangepasste Erzeugung hoher Harmonischer):

Um die Dynamik von Bindungselektronen in Molekülen, z.B. während einer chemischen Reaktion, zu erforschen, werden Lichtimpulse benötigt, deren Dauer im Bereich der Zeitskala dieser Bewegung liegt, nämlich kürzer als eine Femtosekunde. Ein konventioneller Laserimpuls kann auf Grund seiner Wellenlänge nicht zu den benötigten Impulsdauern verkürzt werden. Der Schlüssel zum Subfemtosekundenbereich liegt daher zur Zeit in der Erzeugung hoher Harmonischer, deren Wellenlänge vom extremen Ultraviolet bis in den weichen Röntgenbereich reicht und damit kurz genug ist. Die Erzeugung hoher Harmonischer ist jedoch ein sehr ineffizienter Prozess und um ein makroskopisches Signal zu erhalten, muss die erzeugte Strahlung vieler Atome phasenangepasst überlagert sein. Eine der spezifischen Eigenschaften dieser Phasenanpassung eröffnet die Möglichkeit sogar einzelne Attosekundenimpulse zu erzeugen. Es wird eine Simulation vorgestellt werden, in der gezeigt wird, wie die Phasenanpassung die Erzeugung hoher Harmonischer zeitlich beschränkt und diese nur während der aufsteigenden Flanke des treibenden Laserimpulses zulässt. Das Verhalten dieser zeitlichen Beschränkung wird für verschiedene experimentelle Bedingungen, wie Spitzenintensität der Laserimpulse, Dichte des Erzeugungsgases, sowie Abstand zwischen Fokus und dem Ort der Erzeugung, analysiert. Die Analyse der sogenannten “Half-cycle cutoff” (HCO) Signatur erlaubt einen experimentellen Zugang zu dem Beschränkungsverhalten, welches mit der Simulation verglichen wird. Darüber hinaus kann die HCO-Analyse auch zur groben Abschätzung des Halbwertsbreite des fundamentalen Laserimpulses genutzt werden. Die Positions- und Druckabhängigkeit der Erzeugung hoher Harmonischer wird ebenfalls analysiert werden.

(Phase-matched few-cycle high-harmonic generation: ionisation gating and half-cycle cutoffs):

For the direct exploration of electron dynamics in molecules, e.g. during a chemical reaction, a short pulsed radiation source is required, delivering flashes of duration less than a femtosecond. Due to their wavelengths conventional laser pulses cannot be shortened enough to reach such pulse durations. High-harmonic generation (HHG) is currently the key to the subfemtosecond regime with wavelengths in the extreme-ultraviolet and soft-X-ray range. HHG is a very inefficient process and, therefore, the radiation produced by every atom involved has to be phase-matched to obtain a macroscopic signal. The intrinsic characteristics of phase matching provide the possibility to produce even single attosecond pulses. A simulation will show, how phase matching acts as temporal gate and allows HHG only at the leading-edge of the driving laser pulse. The behaviour of the leading-edge gating will be analysed for different experimental conditions, such as peak intensity of the laser pulse, density of the gaseous generation medium and the distance between focus and generation region. Half-cycle cutoff (HCO) analysis allows an experimental access to observing the leading-edge gate, that will be compared to the simulation. The HCO-analysis can also be used to estimate the duration of the driving laser pulse. In addition the position- and pressure dependence of the HHG process will be analysed, too.

Contents

Part I

Introduction

1 Introduction

Exactly 50 years ago the laser was invented by Maiman [1]. Since this time it has found its way not only into our daily life in many applications but, moreover, it has also become an essential tool in research. The development of pulsed lasers and the quest for shorter and shorter pulses down to the femtosecond (1 fs$= 10^{-15}$ s) regime and the attainable pulse intensities of $\approx 10^{18}$ W/cm^2 [2] and higher opened up a new research field. Finally, the discovery of the generation of coherent radiation with a multiple of the frequency of the driving laser, called high-harmonic generation (HHG), led to a regime of subfemtosecond time scales, where the frontiers between physics and chemistry begin to blur. Chemical reactions are driven by electron-electron interactions. These interactions, and electron dynamics in general proceed in time scales of 10th to 100th of attoseconds (1 as$=10^{-18}$ s) and even faster. The produced harmonic radiation, in the range of extreme ultra violet wavelengths (XUV $\approx 10 \ldots 100$ nm) is emitted in trains of attosecond pulses, in which each individual pulse in the train is short enough to be used for the study of the properties of those interactions and learn more about the characteristics of the bonds in molecules. There are also efforts towards using shaped laser pulses to find a way of controlling chemical reactions. Therewith, the efficiency of chemical reactions could be increased and unwanted by-products suppressed. This work stands at the beginning of all these possibilities since the attention is paid to high-harmonic generation (HHG) itself and its dependence on the carrier-envelope phase (CEP, which is defined in the time domain as phase offset between the maximum of the electric field and the peak of the pulse envelope).

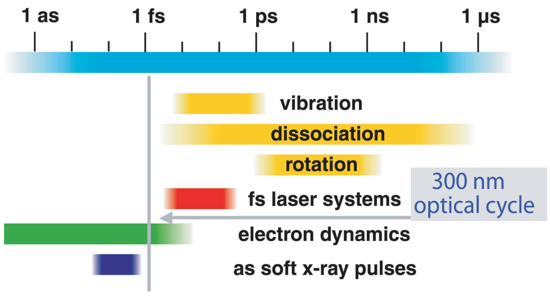

Already in 1961, the second harmonic was observed by Franken et al. [3]. Some twenty years later, the plateau, where the harmonics are generated with equal intensity and the cut-off was discovered [4–6]. For the advancement of the HHG the development of the Titanium:Sapphire laser (Ti:Al_2O_3) around 1986 [7] was an important step towards today's research. Nowadays Ti:Sa lasers provide a standard way to reach pulse durations of a few tens of femtoseconds with peak intensities of around $10^{14} - 10^{16}$ W/cm^2 and higher. The next important step was the invention of a technique to stabilise the CEP, which made it possible to control the light field itself in a range smaller than one cycle of the Ti:Sa laser's central wavelength 800 nm, which corresponds to ≈ 2.67 fs [8]. Using CEP-stabilised light fields, the dependence of processes on the CEP can be observed. For example, it was proposed to measure the absolute carrier-envelope offset-phase [9–11], based on the fact that the electric field appears in the measured harmonic spectra. Controlling the CEP also gives the possibility to produce not only attosecond pulse trains but also single attosecond pulses can be extracted out of the harmonic signal by choosing the "proper" CEP and by the properties of HHG itself.

These single pulses and the properties of the radiation, analysed in this work, are interesting for pump-probe-experiments, in which the target is first prepared by inducing a change in the system, such as excitation, dissociation, or ionisation. This is done with the first so-called pump-pulse. After a defined and experimentally variable time, a second "probe-"pulse, scans the prepared system. The shorter the pulses the better is the temporal resolution of the obtained "snapshot" of the system. By changing the delay between the pump and the probe pulse, subsequent steps of the evolution of the system can be observed.

In this work the properties of HHG will be analysed with particular attention to the phase matching of HHG radiation emitted by the individual atoms of the generating medium, which is essential for obtaining measurable intensities of high-harmonic radiation. The basic principles of phase matching will be explained and analysed with regard to its dependence on several experimental conditions. It is sensitive on the one hand to the properties of the driving laser pulse such as its duration, peak intensity and focussing into the generation area and, on the other hand it depends on the density of the gaseous generation medium and its position with respect to the focal position. A factor can be calculated that is proportional to the output intensity of the harmonic radiation, which is dependent on phase matching. The analysis of this factor allows to understand important properties of HHG and to observe different generation regimes. It is possible to find experimental conditions, in which the harmonic generation is phase-matched during the whole driving laser pulse but, more importantly, the possibility to phase-match only a small time fraction of the fundamental pulse is demonstrated. So to speak, the phase matching provides a time-gating mechanism for HHG, called ionisation gating, which was first observed 2007 [12]. This intrinsic feature of HHG supports the way to very short pulse trains and even single attosecond pulses.

The ionisation gate can also be observed in experiments. In the measured spectra, local maxima in the intensity of the harmonic radiation are visible, whose photon energies are dependent on the intensity of the driving laser pulse at each individual half cycle the radiation is generated in. These are the so called half-cycle cutoffs (HCO). By changing the CEP, the local maximum moves with the carrier wave to higher intensities until the ionisation gate inhibits the HHG and the HCO is intercepted.

This thesis presents a 1D on-axis simulation on phase matching and the ionisation gating which is compared with the measurements. In addition, the yield of the harmonic generation will be analysed for different pressures in the generation cell and different distances between the focus of the fundamental laser beam and the generation area.

This thesis is structured as follows:

Part II gives an overview of the fundamental physics needed to understand the main part of this work. At first, ultrashort laser pulses will be discussed. How these pulses are generated and how they can be provided with pulse lengths of 5-6 fs with a stable CEP will be presented. Then the process of high harmonic generation will be described. Starting with a theoretical picture of HHG at a single atom level we will proceed to consider macroscopic effects on harmonic generation.

Part III presents the simulation on phase matching. There, the influences of the intensity of the driving laser pulse, the pressure in the harmonic-generation medium and its location with respect to the focal position will be concerned.

Part IV describes the experimental setup, which was used for the experiments within this work. It also explains the next stages of this setup, which was designed and partially constructed during the work on this thesis.

Afterwards, in Part V, the first experimental results will be discussed. The harmonic yield will be investigated with regard to its dependence to the pressure in the gas cell used for HHG and its position relative to the focus. Furthermore, CEP-dependence will be shown to be a powerful tool to analyse the behaviour of the HCOs for different pressures and positions. A method will be presented to estimate the minimal pulse durations in our experiments. In the end, the measurements will be compared to the simulation.

Finally, part VI contains a summary of this work and an outlook to possible experiments of the upgraded setup, such as pump-probe experiments with simple molecules. Further ideas for the expansion of the experiment will be discussed, too, such as the insertion of a reaction microscope and a pulse shaper.

Part II

Fundamentals

2 Ultrashort Laser Pulses

The part “Fundamentals” shall give an overview of the fundamental physics needed to understand the main part of this work. At first, ultrashort laser pulses will be discussed. How these pulses are generated, how they are influenced by propagating through dispersive media and how they can be characterised and provided with pulse lengths of 5-6 fs with a stable CEP will be presented. Then the process of high-harmonic generation will be described. Starting with a theoretical picture of HHG at a single atom level we will proceed to consider macroscopic effects on harmonic generation.

2.1 Generation

Nowadays, one of the simplest methods to produce ultrashort laser pulses on the scale of femtoseconds is the usage of mode-locked lasers. The principle of mode locking has been known since the mid-sixties [13, 14]. It is based on setting a relation between the phases of many emitting longitudinal modes in the laser cavity and leads to a significant increase of the peak power in the sum over the entire modes. This can be done actively, which is called “active mode locking” or passively (“passive mode locking”). Several techniques are known in both methods [15]. In the field of attosecond pulse generation the Titanium:Sapphire laser is the common laser type, and it is based on passive Kerr-lens mode locking. Now the principles of passive mode locking and Kerr-lens mode locking shall be introduced.

2.1.1 Mode Locking

In the laser cavity standing waves are formed with a frequency ω_C, which are connected with the cavity length L according to

$$L = n\frac{\lambda_C}{2} = n\frac{\pi c}{\omega_C} \tag{2.1}$$

where c is the speed of light, λ_C the wavelengths of the nth mode and n represents an integer. These standing waves are called longitudinal modes. In general they are independent of each other, although they have a fixed frequency spacing $\Delta\omega_C = \frac{\pi c}{2L}$. In this case the amplitudes and phases are fluctuating randomly. Now, one has to establish a fixed intensity distribution in the frequency domain as well as a phase relation. This will lead to a pulse train in the time domain.

In the laser cavity it is sometimes realised by inserting a saturable absorber with decreasing absorption by increasing intensity of the light that it interacts with. This means higher intensities will experience a higher gain, which leads to an affinity of the laser to operate in a pulsed mode with higher single-shot intensities and not in a cw-mode.

Mathematically one can write the total electrical field $E(t)$ in the laser cavity as a coherent sum over all modes. In the case of $2n+1$ modes, each one to describe as a plane standing wave, one obtains [16]:

$$E(t) = \sum_{q=-n}^{n} E_0 \exp(i[(\omega_0 + q\Delta\omega)]t + q\varphi), \tag{2.2}$$

where ω_0 is the central wave length and φ is the constant phase difference between 2 modes $\varphi_{q+1} - \varphi_q = \varphi$ and the phase of the central mode is defined as 0. Now, one can solve this sum analytically (2.2) and gets:

$$E(t) = A(t)\exp(i\omega_0 t) \tag{2.3}$$

with

$$A(t) = E_0 \frac{\sin((2n+1)\frac{\Delta\omega t+\varphi}{2})}{\sin\left(\frac{\Delta\omega t+\varphi}{2}\right)}. \tag{2.4}$$

So, $E(t)$ behaves like a sine-like carrier wave with a frequency of ω_0 and a (slowly varying) time-dependent amplitude $A(t)$. For the intensity we obtain:

$$I(t) = |A(t)|^2 \tag{2.5}$$

From the requirement of a fixed phase relation, the interference of the modes results in a train of short pulses. One can calculate the maxima of equation (2.4) to find the periodicity τ_P of the pulses. When $\sin((\Delta\omega t + \varphi)/2) = 0$ is achieved the amplitude reaches its maximum, which is the case when $((\Delta\omega t + \varphi)/2) = m\pi$. Accordingly the time difference between two pulses can be calculated as

$$\frac{1}{2}\left((\Delta\omega t_1 + \varphi) - (\Delta\omega t_2 + \varphi)\right) = m\pi - (m+1)\pi \tag{2.6}$$

$$\Leftrightarrow \Delta\omega(t_1 - t_2) = 2\pi \tag{2.7}$$

$$\Leftrightarrow (t_1 - t_2) = \tau_p = \frac{2\pi}{\Delta\omega} = \frac{2L}{c}. \tag{2.8}$$

The pulse rate corresponds to the time of circulation in the laser cavity. So, there is only a single pulse, that oscillates in the cavity back and forth.

Until now, it was assumed that the phase of the central mode is constant and all amplitudes of the different modes are equal. This will not be the case in reality but, to be able to do more general calculations, it is possible to have an analogue description by switching to the frequency domain via Fourier transform. In this case a wave propagates along the z-direction is described by [17]

$$E(z,t) = \frac{1}{2\pi} \int_{-\infty}^{\infty} d\omega \cdot \tilde{E}(z,\omega) \cdot \exp(i\omega t) \tag{2.9}$$

$$\tilde{E}(z,\omega) = \frac{1}{2\pi} \int_{-\infty}^{\infty} dt \cdot E(z,t) \cdot \exp(-i\omega t). \tag{2.10}$$

Furthermore, one can split $\tilde{E}(z,\omega)$ into a spectral amplitude $a(\omega)$ and a spectral phase $\varphi(z,\omega)$:

$$\tilde{E}(z,\omega) = a(\omega) \cdot \exp(i\varphi(z,\omega)). \tag{2.11}$$

To illustrate mode locking, in figure 2.1 a calculated laser-pulse train consisting of 15 locked longitudinal modes is shown in the frequency and time domain as well as the resulting intensity distribution. Already the perfect mode locking of these few modes leads to pulses with a duration of several femtoseconds. In a real laser cavity a number of $\sim 10^6$ modes are locked (but not as perfectly as in the calculation).

Time-Bandwidth Product There is, in analogy to the Heisenberg uncertainty principle, a quantity, that gives a relation between the pulse duration and its bandwidth, the so-called time-bandwidth product. It is defined as:

$$\Delta\tau_P \cdot \Delta\omega \geq 2\pi const. \tag{2.12}$$

where $\Delta\tau_P$ is the full width at half maximum (FWHM) of the pulse and $\Delta\omega$ its bandwidth. The constant depends on the shape of the pulse (for a Gaussian pulse, which is the assumption for all pulses used in this work, this constant is 0.441 [18]). Here it can be seen, that the bandwidth confines the pulse length: the broader the spectrum the shorter the pulse can be. If the product equals this constant, the pulse is called bandwidth limited, all modes are coupled perfectly and the pulse is the shortest possible. In the other case, the phases are not optimally locked, the phases are modulated across the pulse and it is longer than it could be, this is called “chirped pulse”.

For a deeper (mathematical) look into mode locking, [18–20] shall be recommended.

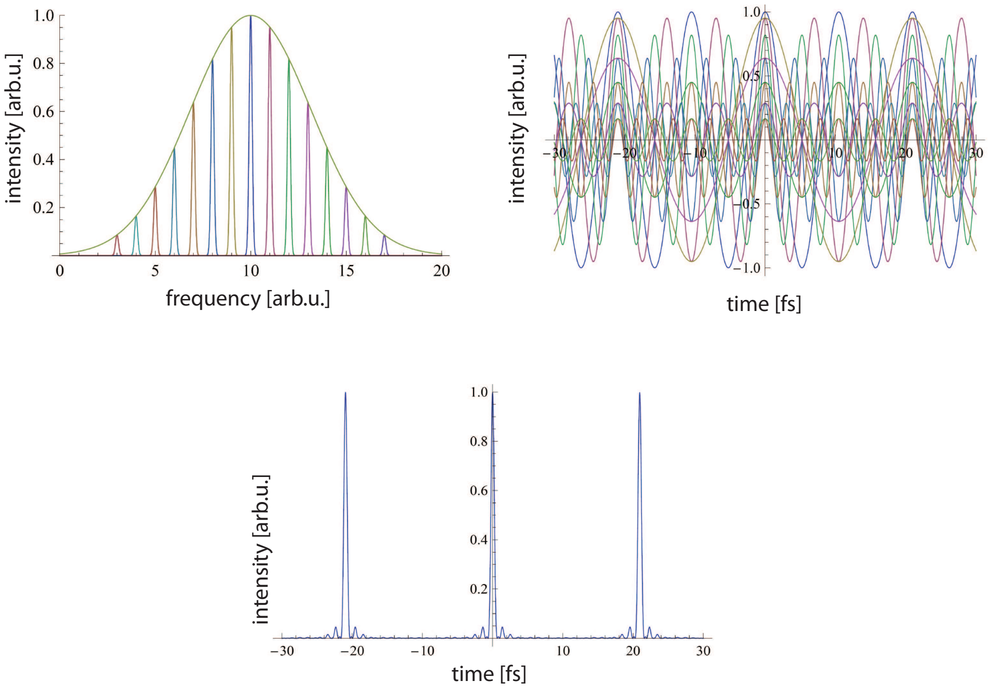

Figure 2.1: From [21]. Above, on the left side a pulse train consisting of 15 longitudinal modes is shown in the frequency domain. Their individual weights are given by the spectral gain profile of the gain medium, approximated by a Gaussian curve. Above on the right side, every single mode is plotted in the time domain and they are already phase locked with each other. As one can see, there are 3 points in time, where the 15 modes have a common maximum and in the lower plot the intensity distribution of the interfering modes is shown. The more modes participate in this process the shorter the pulses are.

2.1.2 Kerr-Lens Mode Locking

The mechanism of Kerr-lens mode locking is one of the most effective methods to provide ultrashort pulses. The Kerr-lens effect is based on the intensity dependence of the refractive index of certain media [22]:

$$n = n_0 + n_2 I(t), \tag{2.13}$$

where n_2 is the nonlinear coefficient of the refractive index. This dispersive effect is very fast and can be regarded as an instantaneous change in the refractive index, even in the fs regime. The intensity of a (Gaussian) laser beam decreases from the centre to the edges. For positive n_2 the refractive index in the centre of the beam is higher than at the edges, which leads to a self-focussing (see figure 2.2). The laser has to be adjusted in a way, that the cavity losses are reduced when the beam is focussed. In this case higher intensities and, thus, the pulsed mode of the laser are preferentially amplified.

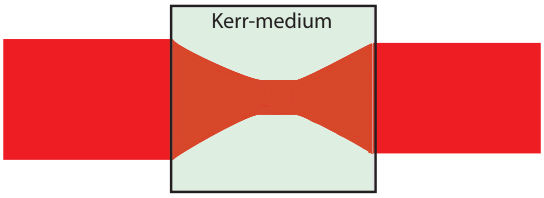

Figure 2.2: Illustration of the self-focussing of a laser beam in a Kerr-medium.

W. Sibbet and O. Spence [23] discovered this effect in 1991 in a Titanium:Sapphire (Ti:Sa) laser. The Ti:Sa crystal itself acts as a Kerr-medium. This is the reason why the Ti:Sa laser simplified the production of ultrashort laser pulses and found its way into many applications.

2.2 Propagation Effects

2.2.1 Dispersion

In matter, the phase velocity v_{ph} for an electro-magnetical wave differs from the speed of light in vacuum. In addition, the phase velocity is also dependent on the wavelength, since the refractive index $n(\lambda)$ is a function of the wavelength [16]

$$v_{ph}(\lambda) = \frac{c}{n(\lambda)}. \tag{2.14}$$

Dispersion can also be described by a frequency dependent wave number $k(\omega)$. The optical spectrum is conserved, while the spectral phase of the pulse changes. As seen before in

(2.9) the temporal- and spatial structure of the laser pulse writes as

$$E(z,t) = \frac{1}{2\pi} \int\limits_{-\infty}^{\infty} d\omega \cdot \tilde{E}(z,\omega) \cdot \exp(i\omega t) \tag{2.15}$$

$$= \frac{1}{2\pi} \int\limits_{-\infty}^{\infty} d\omega \cdot \tilde{E}(0,\omega) \cdot \exp(i\phi(z,\omega)) \cdot \exp(i\omega t), \tag{2.16}$$

where $\phi(z,\omega)$ is the spatio-spectral phase of the laser pulse. This phase describes the dispersive properties of matter. It is useful to look at the Taylor series of the total phase expanded around the central wavelength ω_0 [18, 24]

$$\phi(z,\omega) = \phi(0,\omega) + k(\omega)z \tag{2.17}$$

$$= \phi(\omega_0) + \underbrace{\frac{\partial\phi}{\partial\omega}|_{\omega_0}}_{GD}(\omega-\omega_0) + \underbrace{\frac{1}{2}\frac{\partial^2\phi}{\partial^2\omega}|_{\omega_0}}_{GDD}(\omega-\omega_0)^2 + \underbrace{\frac{1}{6}\frac{\partial^3\phi}{\partial^3\omega}|_{\omega_0}}_{TOD}(\omega-\omega_0)^3, \tag{2.18}$$

with

$$k(\omega) = k_{vac}n(\omega) = \frac{c}{\omega}n(\omega), \tag{2.19}$$

where k_{vac} is the wave vector in vacuum, $n(\omega)$ is the frequency dependent refractive index and c is the velocity of light

GD is the group delay and it is a dispersion effect of the first order. It leads to a delay of the entire pulse. There is no effect on the shaping of the pulse.

GDD is the group delay dispersion, which is a second order effect. It describes the frequency dependence of the group delay where different frequencies have a different delay. This results in a linear chirp of the pulse with frequencies increasing linearly in time from red to blue or vice versa, depending on the sign of GDD.

TOD is the third-order dispersion and also based on the frequency dependence of the group delay dispersion. It leads to higher-order (nonlinear) chirps.

As it can be seen, the role of higher dispersion parameters rises with the growing bandwidth. To generate pulses lasting only a few optical cycles, for which a bandwidth of an octave or more is needed, it is required to counterbalance the collected dispersion, the laser beam accumulates in glass and in gases the laser propagates through (such as air).

2.2.2 Dispersion Compensation

Prism Compressor

In 1984, Fork and Gordon proposed a first version of a prism compressor [25, 26]. Today, it is a very common method to introduce negative dispersion. Prism compressors have a good transmission efficiency if used at Brewster's angle but at too high intensities undesirable non-linear effects may appear.

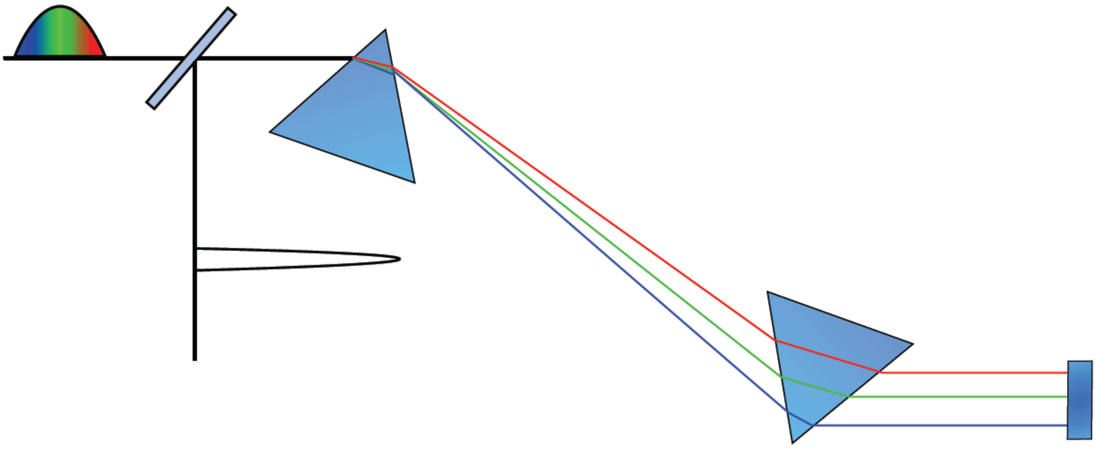

Figure 2.3: From [17]. Design of prism compressor, working with 2 prisms and a mirror.

The first setup worked with four prisms that were arranged such that the central wavelength hits all prisms at Brewster's angle. As the four-prisms setup exhibits a mirror-symmetry, one can also replace two prisms by a mirror, which reflects the light back through the same two prisms under an angle to spatially separate the two beams. This setup and its functional principle are displayed in figure 2.3. The incoming beam is split up by the first prism into its spectral components. The second one collimates the light and sends it to the mirror where it is reflecting back for a return pass. As one can easily see, the different "colours" have different optical path lengths in air as well as in the prism material. In this configuration, the red spectral components, that normally travel faster in dispersive media, are here forced to take a longer path. The right material has to be chosen for the prisms and the right distance between them for a given experimental setup to achieve the perfect compensation of GDD and to minimize TOD and higher-order terms. But it is also possible to make one prism movable back and forth to change the negative dispersion and thus to adjust the compensation.

Here, [18] shall be referred to, where a very profound description and mathematical derivation can be found.

Chirped Mirrors

Another method to create negative dispersion is the usage of so-called chirped mirrors. The basic principle remains the same, imparting different optical path lengths as a function of the frequency of the light. It is realised by arranging a stack of several semi-reflective layers of different materials. Mostly, there are two different layer-materials with a strong difference of the refractive indices. The distribution of the layers has to be chosen in a way that for short wavelengths Bragg‘s law is fulfilled in the upper layers and for longer wavelengths in the lower ones. The perfect layer distribution for any kind of high-order dispersion can be calculated by using computer algorithms but there is no possibility to adapt these multi-layer mirrors for another dispersion setting. They are very inflexible with respect to changes in the experimental setup.

As incidence medium for chirped mirrors usually fused silica are used (as SiO_2 or TiO_2) [27]. The first stage of development still had problems through unmeant reflections at the surface, which resulted in an oscillation in the phase. Today, one usually has a set of two chirped mirrors. One of them has a $\frac{\lambda}{4}$-layer evaporated, which annihilates the oscillations.

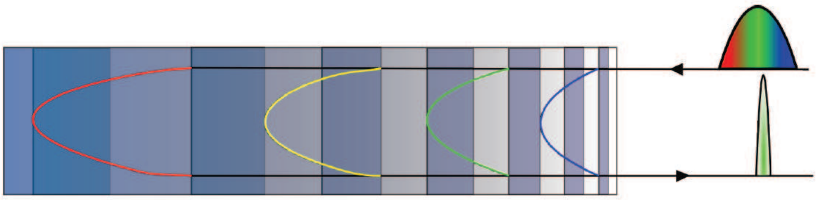

Figure 2.4: From [17]. Schematic transversal section through a chirped mirror. Depending on the local layer spacing, light of a specific wavelength is reflected at a specific depth within the material, here introducing longer optical paths for red light vs. blue light in order to reverse the effect of normal dispersion.

2.2.3 Dispersion Effects at High Intensity

Self-Phase Modulation

For harmonic generation (and especially isolated single attosecond pulse generation), the pulses have to be extremely short and very intense. Thus, amplified pulses are used, with a restricted gain bandwidth and effects as gain narrowing occur that are limiting factors for the bandwidth and, for this reason, for the minimal pulse length, too. In addition, as seen in the chapter on ultrashort pulse generation, the Kerr effect is at work in the gain crystal of a Ti:Sa laser and bandwidth limited pulses are able to reach a critical peak power in their focus. For these reasons, chirped pulses with a narrowed spectrum are usually amplified in the laser cavity, such that for generating short pulses, the spectrum has to be broadened. This can be achieved via self-phase modulation, which is a nonlinear-optical effect that leads to a broadening of the pulse spectrum and its origin lies in the induced intensity-dependent refractive index change of the medium. This change causes a phase modification on the incoming pulsed wave, induced by its own temporal intensity profile, hence the name “self-phase modulation”. To see how this arises, one can start out with the wave equation of a plane wave propagating through an isotropic medium [28]:

$$\left(\frac{\partial^2}{\partial z^2} - \frac{n_0^2}{c^2}\frac{\partial^2}{\partial t^2}\right) \cdot E = \frac{4\pi}{c^2}\frac{\partial^2}{\partial t^2} \cdot P^{(3)}, \tag{2.20}$$

where E is the electric field

$$E = A(z,t)\exp(ik_0 z - i\omega_0 t), \tag{2.21}$$

$P^{(3)}$ is the induced third-order polarisation in the medium

$$P^{(3)} = \chi^{(3)} \left|E\right|^2 E, \tag{2.22}$$

$\chi^{(3)}$ is the susceptibility of the third order and n_0 is the linear refractive index. The slowly varying amplitude approximation is used by neglecting $\frac{\partial^2 A}{\partial t^2}$ on the left side and keeping only $\frac{4\pi}{c^2}\chi^{(3)} \left|A\right|^2 A$ on the other side of the equation (2.20). This results in

$$\left(\frac{\partial}{\partial z} - \frac{n_0}{c}\frac{\partial}{\partial t}\right)A = \frac{4\pi\omega_0^2}{i2k_0c^2}\chi^{(3)} \left|A\right|^2 A. \tag{2.23}$$

With $z' \equiv z + \frac{ct}{n_0}$ and $A = |A|\exp(i\phi)$ one receives

$$\frac{\partial\left|A\right|}{\partial z'} = 0 \tag{2.24}$$

$$\frac{\partial\phi}{\partial z'} = \frac{2\pi\omega_0^2}{c^2k_0}\chi^{(3)} \left|A\right|^2. \tag{2.25}$$

The result of these equations can be easily calculated as

$$|A| = |A(t)| \tag{2.26}$$

and

$$\phi(z,t) = \phi_0 + \frac{2\pi\omega_0^2}{c^2k_0}\chi^{(3)} \left|A(t)\right|^2 z. \tag{2.27}$$

In these two equations one can see that the pulse shape is not changed but there is an additional phase shift $\mathit{\Delta}\phi(t) = \phi(z,t) - \phi_0$, while the pulse is propagating through a medium from 0 to z. The frequency of the wave can be written as

$$\omega = \omega_0 \frac{\partial(\mathit{\Delta}\phi)}{\partial t}. \tag{2.28}$$

The change of the phase $\mathit{\Delta}\phi(t)$ now leads to a frequency modulation

$$\omega - \omega_0 = \mathit{\Delta}\omega(t) = -\frac{\partial(\mathit{\Delta}\phi)}{\partial t} = -\frac{2\pi\omega_0^2}{c^2 k_0}\chi^{(3)}\frac{\partial\left|A(t)\right|^2}{\partial t} z. \tag{2.29}$$

The spectral broadening is due to the in- and decreasing intensity. While the frequency at the pulse peak is conserved, the leading edge is red-shifted and the trailing edge is blue-shifted.

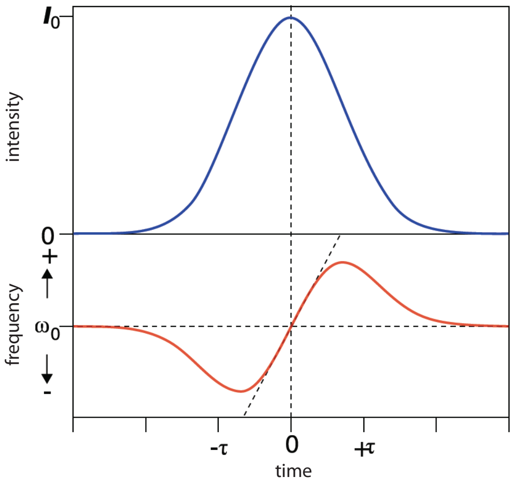

Figure 2.5: From [17]. It is illustrated in blue what the fundamental pulse envelope looks like and in red is shown the instantaneous frequency.

In the experiment one focuses the laser beam into a thin hollow fibre, which is filled with a gas (in our setup it is usually filled with 1.5 bar of neon) as we will see later in the Chapter “Experimental setup”.

2.3 Pulse Characterisation with an Autocorrelator

By virtue of the shortness of the discussed laser pulses, pulse characterisation via photo detectors and sampled scopes is not possible any more, due to the comparatively slow (picosecond) electron-response times in typical detectors. To resolve faster processes such as a few-cycle laser pulse, a shorter event is needed as measuring unit. The idea of autocorrelation is to use the pulse itself as fast gate to measure its own duration, since it is the fastest accessible event in this case.

An autocorrelator consists of a Michelson- or Mach-Zehnder-interferometer, in which the pulse is divided into two parts by a beam splitter. One arm can be extended to create and to vary a delay between both. The two beams are focussed into a non-linear optical crystal for second-harmonic generation. There are now two ways to send these two beams into the crystal. First, one could use a non-collinear geometry, i.e. sending the beams into the crystal under a non-zero angle. This method is called intensity autocorrelation. The nonlinear polarisation is expressed by the two interfering electric fields $E_1(t)$ and $E_2(t)$ convoluted with the second-order non-linear susceptibility $\chi^{(2)}$ and, therefore, with the second-order polarisation $P^{(2)}$. If the material response is instantaneous, one obtains [29]

$$P^{(2)}(t) \propto E_1(t) \cdot E_2(t) = E(t) \cdot E(t-\tau) \tag{2.30}$$

Hence, one can estimate the signal as measured on a photodiode

$$I_{AC}(\tau)dt \propto \int\limits_{-\infty}^{\infty} |A(t)A(t-\tau)|^2 \, dt \propto \int\limits_{-\infty}^{\infty} I(t)I(t-\tau)dt. \tag{2.31}$$

This gives one only a rough estimate on the temporal pulse shape, because a photo detector's response time is too slow and it integrates over several pulses. One is also able to send the beams colinearly into the non-linear crystal. The fundamental beam is filtered out and one only gets the second-harmonic signal. The total electric field is then

$$E(t,\tau) = E(t) + E(t+\tau). \tag{2.32}$$

In this case the polarisation is proportional to the square of the electric field

$$P^{(2)}(t) \propto (E(t)+E(t+\tau))^2 = \left(A(t+\tau)\exp(i\omega_0(t+\tau))\exp(i\phi_{CE}) + A(t)\exp(i\omega_0(t))\exp(i\phi_{CE})\right)^2, \tag{2.33}$$

where $A(t)$ is the complex amplitude, ω_0 is the carrier frequency and ϕ_{CE} is the carrier-offset phase of the laser pulse. The photo-detector integrates over the envelope of both pulses (the delayed and the undelayed one). For the output intensity one can write:

$$I_{IAC}(\tau) \propto \int\limits_{-\infty}^{\infty} \left|(A(t+\tau)\exp(i\omega_0(t+\tau))\exp(i\phi_{CE}) + A(t)\exp(i\omega_0(t))\exp(i\phi_{CE}))^2\right|^2 dt. \tag{2.34}$$

Evaluation of this expression shows, that the interferometric autocorrelation function is composed of the following terms [29]:

$$I_{IAC}(\tau) = I_{back} + I_{AC}(\tau) + I_{\omega}(\tau) + I_{2\omega}(\tau). \tag{2.35}$$

The signal of the interferometric autocorrelation consists of a background I_{back}, of the intensity autocorrelation I_{AC}, of a coherence term I_{ω} oscillating with ω_0 and of a coherence term $I_{2\omega}$ oscillating with $2\omega_0$. They are given by:

$$I_{back} = \int\limits_{-\infty}^{\infty} \left(|A(t+\tau)|^4 + |A(t)|^4\right) dt = 2\int\limits_{-\infty}^{\infty} I^2(t)dt \tag{2.36}$$

$$I_{AC} = 4\int\limits_{-\infty}^{\infty} \left(|A(t+\tau)|^2 + |A(t)|^2\right) dt = 4\int\limits_{-\infty}^{\infty} I(t+\tau)\cdot I(t)dt \tag{2.37}$$

$$I_{\omega}(\tau) = 4\int\limits_{-\infty}^{\infty} Re\left[(I(t) + I(t+\tau))\, A^*(t)A(t+\tau)\exp(i\omega_0\tau)\right] dt \tag{2.38}$$

$$I_{2\omega}(\tau) = 2\int\limits_{-\infty}^{\infty} Re\left[A^2(t)(A^*(t+\tau))^2\exp(i2\omega_0\tau)\right] dt. \tag{2.39}$$

The so-called interferometric autocorrelation is given by equation 2.35 that is similar to an intensity autocorrelation with an additional background. The carrier-envelope phase (CEP, which is defined as the offset between the maximum of the electric field and the peak of the pulse envelope and will be introduced in the next chapter) also drops out. Therefore, another method has to be implemented to get the phase information of the pulse as well. This technique will be discussed next. What can be gathered from an autocorrelation is only a relation between the FWHM τ_p of the pulse and τ_{AC} of the signal. It is given by [30]

$$\frac{\tau_{AC}}{\tau_p} = \sqrt{2}. \tag{2.40}$$

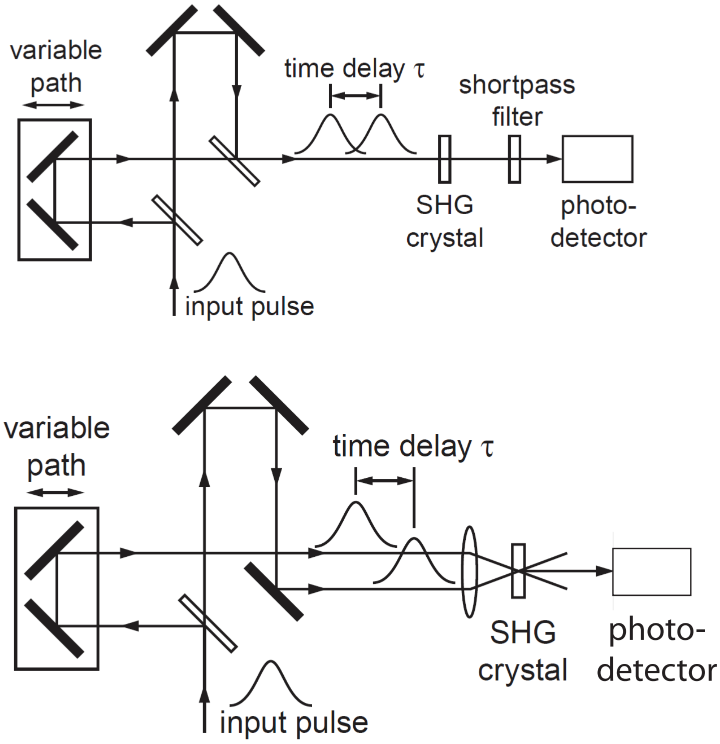

Figure 2.6: From [30]. The upper figure shows the setup for an interferometric autocorrelation, in which the split beam is recombined colinearly and the lower figure shows the setup for an intensity autocorrelation in which the beams are non-colinearly incident on the SHG-crystal.

2.4 CEP Stabilisation

As will be shown later, the stabilisation of the carrier-envelope phase (CEP) and the involving possibility of controlling it is very important in the regime of ultrashort pulses which contain only a few cycles. There, the process of high-harmonic generation that will be discussed in detail later depends strongly on the CEP. Now, I will discuss what is the CEP and how to measure and stabilise it.

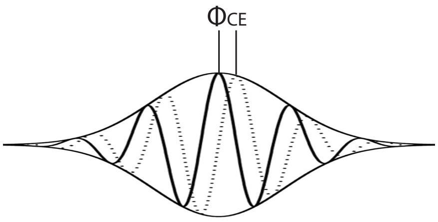

Figure 2.7: Illustration of a few-cycle pulse for two different CEP values.

2.4.1 Definition

In figure 2.7 a few-cycle pulse is shown, where ϕ_{CE} is the carrier-envelope phase (CEP). To describe this phase in the electric field, one can write the field as

$$E(t) = A(t)\cos(\omega_0 t + \phi_{CE}) \tag{2.41}$$

where $A(t)$ is the carrier envelope and ω_0 the carrier-wave frequency. The reliable periodicity of the pulse train of a mode-locked laser enables one to identify a phase between the carrier envelope and the carrier wave. The CEP may change within and outside the laser cavity. The CEP can be divided into two components [20]

$$\phi_{CE} = \phi_o + \mathit{\Delta}\phi_{CE}, \tag{2.42}$$

where ϕ_0 represents a constant offset phase and $\mathit{\Delta}\phi_{CE}$ stands for the change of the phase between two shots due to the conditions in the cavity. In reality, ϕ_0 is also fluctuating, because of dispersion effects, since the laser pulses are propagating through dispersive media as air.

The shot-to-shot changing in the phase $\mathit{\Delta}\phi_{CE}$ is also a consequence of dispersion from the optical elements within the laser cavity. There is a sampling of $\mathit{\Delta}\phi_{CE}$ one time per round trip, when the pulse hits the output coupler of the laser cavity. Only a change in the phase $modulo(2\pi)$ matters and the CEP is finally defined by

$$\phi_{CE} = (\frac{1}{v_g} - \frac{1}{v_{ph}})L\omega_c mod(2\pi), \tag{2.43}$$

where v_g is the group velocity, v_{ph} is the phase velocity, L the round-trip length and ω_c the round-trip frequency.

2.4.2 Measuring the CEP

Figure 2.8 shows an infinite pulse train in (a) the time domain as well as (b) in the frequency domain. A constant $\Delta\phi_{CE}$ is assumed, which can be seen in the time domain. In the frequency domain this pulse train is represented by a frequency comb with equal interspaces between the single tooths, giving the repetition rate f_{rep}. The whole comb has an offset, defined as f_0. The CEP can be expressed through f_0 and f_{rep}, as shown in figure 2.8:

$$\Delta\phi_{CE} = 2\pi\frac{f_0}{f_{rep}}. \tag{2.44}$$

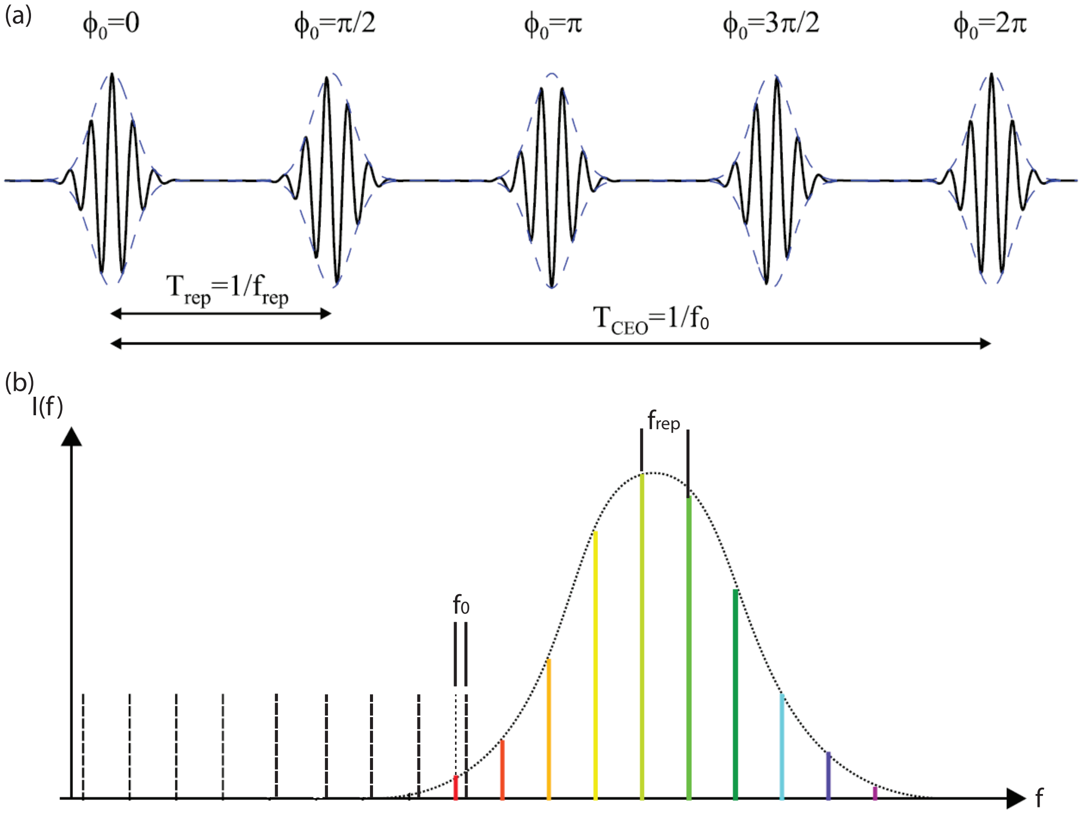

Figure 2.8: Infinite pulse train in (a) the time- and (b) the frequency domain.

To stabilise the CEP one has to fix f_0. A straight-forward method to measure this offset is to frequency-double the red side of the spectrum and interfere it with the blue parts.

Let us pick up only the n-th component of the red side. The electric field will have the phase

$$\phi_n = 2\pi(f_n + f_0)t + \phi_{0n} = 2\pi(nf_{rep} + f_0)t + \phi_{0n}, \tag{2.45}$$

where ϕ_{0n} the residual optical spectral phase is constant. For the $2n$-th component one can write analogously

$$\phi_{2n} = 2\pi(f_{2n} + f_0)t + \phi_{02n} = 2\pi(2nf_{rep} + f_0)t + \phi_{02n}. \tag{2.46}$$

The n-th part of the spectrum can be doubled with a standard second-harmonic nonlinear crystal (such as a BBO-crystal) and the optical heterodyne beating between both signals is detected by a photodiode. The detected signal will have an interference term within the phase

$$\phi_{det} = 2\pi f_0 t + 2\phi_{0n} - \phi_{02n} \tag{2.47}$$

The desired influence of f_0 is located in the radio-frequency domain and can easily be measured with common techniques [20]. This kind of interferometer, as it is used to measure the CEP, is called f-2f interferometer and is shown in 2.9.

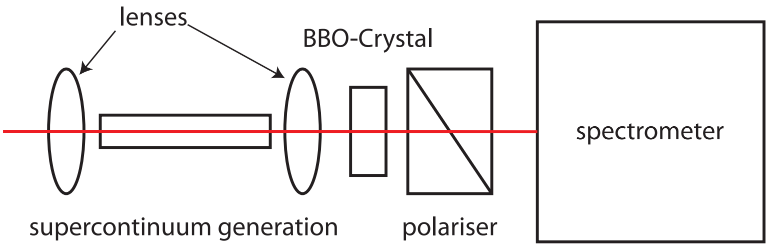

Figure 2.9: Schematic build-up of an f-2f-interferometer, where at first the spectrum of the laser is broadened by SPM to at least one octave and then it is collimated into a BBO-crystal to produce the second harmonic. To see interference between the fundamental beam and the second harmonic, the polarisation of both have to be aligned, because of their perpendicular polarisation [31].

2.4.3 Stabilising CEP

There are several possibilities to adjust f_0. One has to change the difference between the intercavity group and the phase-velocity. One possibility is the usage of a prism compressor, as discussed before. Another method is based on the modulation of the pump power. The physical mechanism is not well understood so far. Possible effects that are at the bottom of this behaviour are:

- non-linear phase shifts in the Ti:Sa-crystal
- intensity-dependent spectral drifts
- differential change in the phase- and group velocity

To change the pump power at the pump laser itself would be too slow. Instead, a acusto-optical modulator (AOM) or electro-optical modulator can be set up into the cavity or by a mirror mounted on a piezo-transductor to change the cavity length and a third possibility is the insertion of glass wedges. In general, these three methods are combined, because of their different influence strength to the CEP. The AOM can adjust the CEP in a small range but fast. In contrast, the wedges allow only a slow variation of the phase but over a larger span.

3 High Harmonic Generation

It is impossible to compress the ultrashort pulses beyond a certain frontier with the techniques discussed above. Light pulses cannot be shorter than at least one optical cycle, which corresponds to 2.67 fs at 800 nm. A new technique has to be found to gain light pulses in the sub-femtosecond regime. High-harmonic generation (HHG) has been known since the late eighties [4, 5]. Some years later Farkas and Toth realized the role of HHG for the creation of very short light pulses in a relatively simple way [32]. HHG is a non-linear- and non-perturbative process and the spectra are characterised by a decrease in the low order harmonics followed by a long plateau and completed with a fast cut-off (see fig. 3.1).

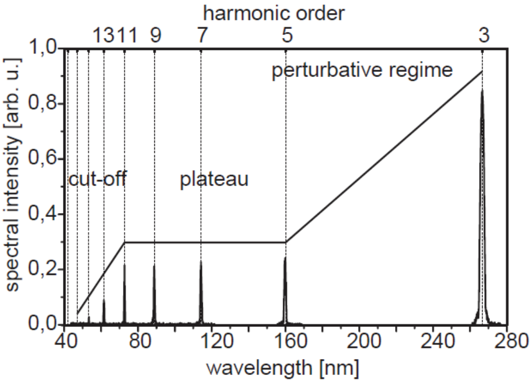

Figure 3.1: From [30]. Typical harmonic spectrum generated in xenon, showing the characteristic shape: the decreasing, the plateau and the cut-off.

The first efforts aimed on generating higher-order harmonics [33, 34] and consequently a stretching of the plateau. In 1992, Krause finally showed that the cut-off position follows an universal law [35]

$$CO - position \approx 3U_p + I_p, \tag{3.1}$$

where I_p is the ionisation potential of the atoms in the generation medium and U_p is the ponderomotive potential, which is defined as the kinetic energy collected by an electron in a laser field E with the frequency ω

$$U_p = \frac{e^2 E^2}{4 m_e \omega^2}, \tag{3.2}$$

where e and m_e are the charge and mass of an electron. Shortly after, a simple quasi static theory was developed, that described the properties of the HHG spectra very well. This theory is known as *simple man's theory* or *three-step model* [36, 37]. It can be derived from a fully quantum-mechanical theory based on the strong field approximation [38]. Both, the quasi-static and the quantum-mechanical approach shall be discussed in the next chapters.

3.1 Three-step Model

While Corkum and Kulander call it a two-step model, now the process is mostly divided into three parts. At first, an electron is ionised by the fundamental laser beam, afterwards it propagates in the laser field essentially unperturbed by the atom's Coulomb potential and finally it may recombine with its parent ion.

Step One: Ionisation

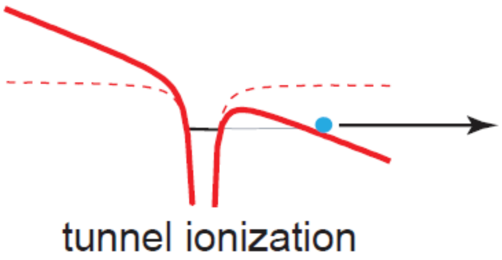

Figure 3.2: First step: The laser bends the potential and the electron is able to tunnel out.

The electric field of the high-intense laser $E(t)$ has a strong influence on the atomic potential that shall be assumed to be Coulombic. One can write for the effective potential composed by the Coulomb potential of a singly charged ion and the induced laser potential

$$V(\boldsymbol{r},t) = \frac{e^2}{4\pi\varepsilon_0 r} + e\boldsymbol{E}(t)\boldsymbol{r}. \tag{3.3}$$

This perturbation leads to a time-dependent bending of the atomic potential. At a certain time, depicted in figure 3.2, in the right-hand regime only a barrier remains, through which the electron is able to tunnel out.

Tunnel ionisation has been known for a long time; the first description was 1965 by Keldysh [39]. This model gives the ionisation rate for a hydrogen atom. Over the years, there were more detailed approaches, like ADK [40], which provides the ionisation rates for more complex atoms and, furthermore, is in good agreement with experiments [41]. The ADK ionisation rate, which is based on a quasi classical approximation, is given by

$$W = \omega_A C^2_{n^*,l} f(l,m) I_p \left(\frac{3E}{\pi (2I_p)^{\frac{3}{2}}} \right)^{\frac{1}{2}} \times [\frac{2}{E}(2I_p)^{\frac{3}{2}}]^{2n^* - |m| - 1} \cdot \exp\left(-\frac{2}{3E}(2I_p)^{\frac{3}{2}} \right), \quad (3.4)$$

where ω_A is the atomic unit of frequency, I_p the ionization potential, E the electric field of the laser, the factors $f(l,m)$ and $C_{n^*,l}$ are given by

$$f(l,m) = \frac{(2l+1)(l+|m|)!}{2^{|m|}(|m|)!(l-|m|)!} \quad (3.5)$$

and

$$C_{n^*,l} = \left(\frac{2e}{n^*} \right)^{n^*} \frac{1}{(2\pi n^*)^{\frac{1}{2}}}, \quad (3.6)$$

with l is the azimuthal quantum number, m the magnetic quantum number and n^* the effective principal quantum number. The change caused by effects, such as electron shielding, in many-electron atoms is approximated by

$$n^* = \frac{Z}{(2I_p)^{\frac{1}{2}}}, \quad (3.7)$$

where Z is the created charge of the ion. The two factors $f(l,m)$ and $C_{n^*,l}$ define the atomic structure and the term $(\frac{3E}{\pi(2I_p)^{\frac{3}{2}}})^{\frac{1}{2}}$ results from averaging over a whole laser pulse. Today, the ADK rate is the most commonly used theory to describe the first step of this three-step model.

However, tunnel ionisation only occurs in certain regimes of the laser intensity and frequency. Keldysh introduced a parameter which is an indicator showing if strong-field ionisation proceeds in the tunnel regime or not. This parameter contains the ionisation potential I_p as well as the maximum of the laser field E_0 and its central wavelength ω

$$\gamma = \sqrt{\frac{I_p}{2U_p}}. \quad (3.8)$$

For γ ≪ 1 tunnel ionisation preponderate and γ ≫ 1 represents the multi-photon regime, in which the electron can be classically ripped off or barrier-suppressed ionisation [41] may occur. As it will be pointed out, conditions supporting tunnel ionisation are the best for HHG.

Step Two: Propagation

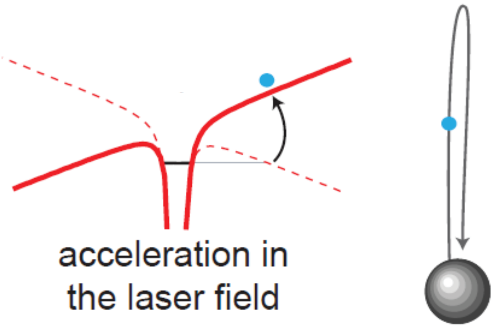

Figure 3.3: Second step: The ionised electron moves driven by the electric field of the laser.

In this step the electron is initially seen in a 1-D-model and as free particle, which is only influenced by the electric field of the laser and the ion is neglected. Initially, the electron is considered to be resting and can be found in the origin ($x_0 = 0; v_0 = 0$). In doing so, a force takes effect on the electron, that can be described as [36, 42]

$$F = -eE(t), \tag{3.9}$$

and this force results in an acceleration in the oscillating laser field $E(t) = E_0 cos(\omega t + \phi)$

$$a = \frac{F}{m} = -\frac{e}{m_e}E(t) = -\frac{e}{m_e}E_0\cos(\omega t + \phi). \tag{3.10}$$

Through a simple integration over the acceleration one can calculate the electron‘s velocity

$$v(t) = -\frac{eE_0}{m_e\omega}[\sin(\omega t + \phi) - \sin(\phi)] \tag{3.11}$$

and integrating the velocity gives the position of the electron

$$x(t) = \frac{eE_0}{m_e\omega^2}[cos(\omega t + \phi) + \omega t\sin(\phi) - \cos(\phi)]. \tag{3.12}$$

Looking more closely at equation (3.12) reveals some attributes of the electron trajectories. The first and the second terms are time-dependent. The first describes an oscillation of the electron with the laser pulse. The second term can be illustrated as a drift, whose strength is defined by ϕ. Plotting the electron trajectories (see figure 3.4) shows that only a few trajectories actually lead back to the parent ion. Only if this condition is fulfilled, the electron is able to recombine.

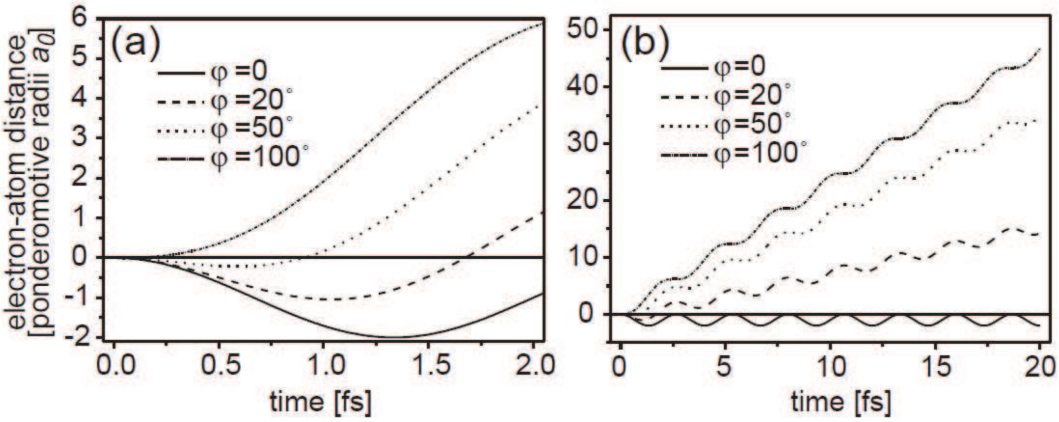

Figure 3.4: From [30]. Electron trajectories for various phases of the driving laser field. (a) shows an excerpt near to the origin from (b).

Step Three: Recombination

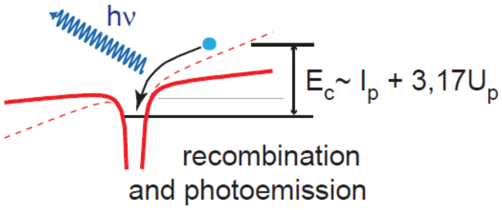

Figure 3.5: Third step: There is a probability that the electron recombines and emits harmonic radiation, if it passes the ion again.

If the electron comes back to the ion and if it recombines with it, harmonic radiation will be emitted with the energy

$$\hbar\omega = E_{kin} + I_p, \tag{3.13}$$

where E_{kin} is the kinetic energy of the returning electron and I_p the ionisation potential of the ionised atom. To maximise the energy of the harmonic radiation, one has to maximise the kinetic energy of the electron and this is tantamount with the maximal velocity.

The velocity in formula (3.11) reaches its maximum if $\omega t + \phi = \frac{3\pi}{2}$ and simultaneous $\sin(\phi)$ has to be as small as possible. Therefore, it obtains a value of $\phi = 0.08\pi \hat{=} 18°$ and $E_{kin,max} = 3.17 U_p$, what confirms the experimental observations [42].

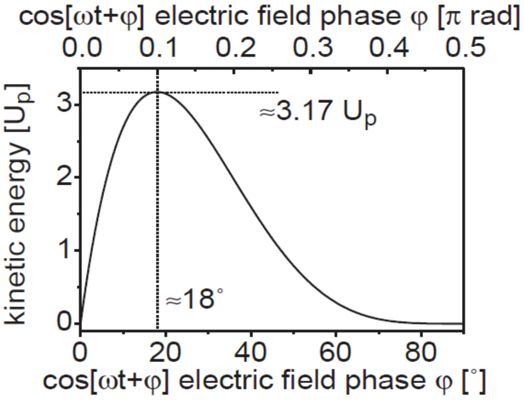

Figure 3.6: Here one sees the kinetic energy of the electrons at the recombination versus the electric field phase of the driving laser pulse at the starting point in time of the electron trajectory.

Now it also becomes obvious why tunnel ionisation is the favourite mechanism for the HHG. As one can see in equation (3.4), it is directly dependent on the electric field. The highest harmonics are generated by electrons ionised near the peaks of the electric fields at $\phi \approx 18°$, and the tunnel ionisation rate is high at the peaks, so many electrons are freed and can attend at the HHG process. Multi-photon ionisation is only sensitive on the averaged intensity and do not react to the phase. In addition, one needs a high ponderomotive potential for high-energy harmonic radiation, which is also ensured in the tunnel regime, as can be seen in the Keldysh-parameter (see equation (3.8)).

To calculate the expected spectrum of the high-harmonic radiation, Corkum proposed to evaluate the expectation value for the dipole operator $\langle\psi|er|\psi\rangle$. One obtains a frequency-dependent induced dipole moment $|d(\omega)|$, whose square is proportional to the emission intensity. This also corresponds very well to the experimental measurements of the intensity of the high harmonics and the cut-off.

3.2 Quantum Mechanical Model

This quantum mechanical approximation, equivalent to the three-step model, was first proposed by Lewenstein et al. [38]. Here, a single-electron approximation is assumed and the laser field $E_0 \cos(\omega t + \phi)$ is polarised in x-direction. For that purpose, the Schrödinger equation can be written as

$$i|\psi(\boldsymbol{x},t)\rangle = [-\frac{1}{2}\nabla^2 + V(\boldsymbol{x}) - E\cos(t)x]|\psi(\boldsymbol{x},t)\rangle \tag{3.14}$$

To solve this equation easily, three assumptions shall be fulfilled.

- The contribution of all bound states, except the ground state $|0\rangle$, can be neglected in the evolution of the system
- The depletion of the ground state can be neglected
- In the continuum the electron can be treated as a free particle only influenced by the electric field of the laser

Due to that, the electron wave function is given by

$$|\phi(t)\rangle = \exp(iI_p t)(a(t))|0\rangle + \int d^3\boldsymbol{v} b(\boldsymbol{v},t)|\boldsymbol{v}\rangle, \tag{3.15}$$

where $a(t) \approx 1$ is the ground state amplitude and $b(\boldsymbol{v},t)$ are the corresponding continuum state amplitudes of the velocity of the electron v. The Schrödinger equation can be solved exactly. With $X(t) = \langle\psi(t)|X|\psi(t)\rangle$ one can calculate the time dependent dipole moment $X(t)$:

$$X(t) = \int d^3\boldsymbol{v} d_x^*(\boldsymbol{v}) b(\boldsymbol{v},t) + c.c., \tag{3.16}$$

where $d(\boldsymbol{v}) = \langle v|X|0\rangle$ is the transition matrix element between ground and continuum state and $d_x(\boldsymbol{v})$ is its component parallel to the polarisation direction of the electric field. Here, the canonical momentum $\boldsymbol{p}$ shall be introduced

$$\boldsymbol{p} = \boldsymbol{v} + \boldsymbol{A}(t). \tag{3.17}$$

With this the dipole moment can be written as

$$X(t) = i\int_0^t dt' \int d^3\boldsymbol{p} E\cos(t') d_x(\boldsymbol{p} - \boldsymbol{A}(t')) \times d_x^*(\boldsymbol{p} - \boldsymbol{A}(t)) \exp(-iS(\boldsymbol{p},t,t')) + c.c., \tag{3.18}$$

where

$$S(\boldsymbol{p},t,t') = \int\limits_{t'}^{t} dt' \left(\frac{(\boldsymbol{p} - \boldsymbol{A}(t'))^2}{2} + I_p \right) \tag{3.19}$$

is the quasi classical action. Actually, the three steps can be recognised in equation (3.18): the first term in the integral $E\cos(t')d_x(\boldsymbol{p} - \boldsymbol{A}(t'))$ is the probability amplitude for the transition of an electron from the ground state to a continuum state at time t' and with the canonical momentum $\boldsymbol{p}$. Thereafter, the electron propagates until the time t and along the way it collects a phase factor, which is equivalent to $\exp(-S(\boldsymbol{p},t,t'))$. Finally, the last term $d_x^*(\boldsymbol{p} - \boldsymbol{A}(t))$ indicates the probability, with which the electron recombines with its parent ion at time t.

By Fourier transform the time-dependent dipole moment, i.e. the harmonic spectrum can be gained. This spectrum can be analysed further and a refined expression for the cut-off law is found:

$$\hbar\omega_c = 3.17U_p + f\,(c)\,I_p, \tag{3.20}$$

where ω_c is the cut-off frequency and $f(x)$ a function that is slowly decreasing by increasing $x = I_p/U_p$, which is in the magnitude of 1. In comparison to the quasi-static model, this correction is because of two reasons:

1. The electron may not be in the origin of the system after tunneling. In this case it can collect more or less kinetic energy, depending on whether it has appeared before or after the origin.

2. The electron wave packet is spread out during the propagation. This reduces the kinetic energy relative to the ion during recombination.

The fact that only odd-numbered harmonics are generated is (in both models) due to the symmetry of the atomic potential. The even harmonics annihilate each other.

3.3 Single-Atom Response

In the chapters above, it has been shown, how harmonic radiation is generated and how the spectra can be calculated via Fourier transform of the dipole moment. Furthermore, it has been demonstrated, that it is possible to relate certain energies to specified trajectories of an electron. In figure 3.7 one can see, that the produced energies of the high-harmonic radiation essentially come from two trajectories, except for the cut-off energy. There are also more possible trajectories that have the same energy but these trajectories are extended over more than one half-cycle. Due to the increasing spreading of the electron wave packet with the elapsed time, the distribution of these (very long) trajectories is very low.

To describe the process of HHG more precisely, a quantum mechanical theory was developed, based on the strong-field approximation [43, 44]. In this model the harmonic dipole moment is written as coherent sum. The addends are called quantum paths and reflect the electron trajectories in a generalised mould. Quantum effect as tunnel ionisation and quantum diffusion are considered in this model. Finally, the dipole d_q can be written as [45]

$$d_q = \sum_j A_q^{(j)} \exp(iS_q^{(j)}), \tag{3.21}$$

where q is the harmonic order, j is the quantum path, $A_q^{(j)}$ is a weighting factor and $S_q^{(j)}$ describes the phase and is given, as before, by the quasi-classical action, collected by the electron on the corresponding trajectory. This phase can be approximated by the product of the mean kinetic energy of the electron (ponderomotive energy) and the time of flight

$$S_q^{(j)} \approx -U_p \tau_q^{(j)} \approx -\alpha_q^{(j)} I(r,z,t) = \Phi_q^{(j)}(r,z,t), \tag{3.22}$$

where $I(r,z,t)$ is the space- and time-dependent laser intensity and $\alpha_q^{(j)}$ is the so-called reciprocal coefficient of the intensity [46] which is defined as the slope of the phase $\Phi_q^{(j)}(r,z,t)$ collected by the j-th quantum path as function of the intensity of the generating field (r is the radial distance to the center of the beam and z is the propagation axis). The quantum paths that contribute principally to the signal pertain to static action and are calculated by solving the saddle-point equations. They can easily be visualised by Fourier transform the windowed dipole moment, which is given by [47]

$$D_q(I) = A(I) \exp(i\Phi_q^{(j)}(I)), \tag{3.23}$$

where $A(I)$ is the dipole strength and $\Phi_q^{(j)} = -\alpha_q^{(j)} I$. In figure 3.7 the $\alpha(I)$-distribution is plotted against the intensity of the driving laser pulse. At low laser intensities, the main path corresponds to $I_p + 3.17U_p$, which is the cut-off energy. At higher intensities the main path is separated into two components, corresponding to the long and short quantum paths, where higher-order paths can be seen as well but they are suppressed (higher $\alpha(I)$ represents trajectories that spread over more than one cycle). Comparing the degree of strength of $\alpha(I)$ for the two main-paths, it is obvious that the short trajectory is much less effective, than the long path. They differ by a factor of ≈ 27

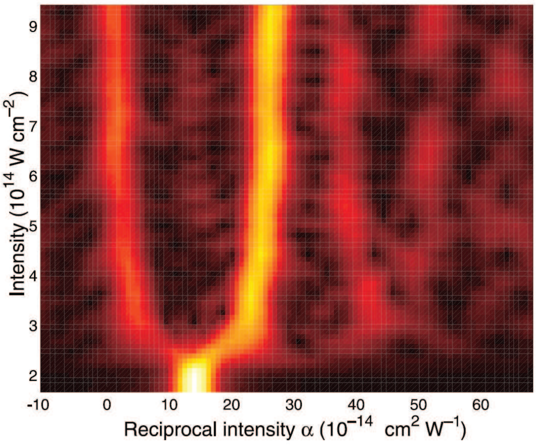

Figure 3.7: From [46]. This plot is calculated for the 45th harmonic. On the ordinate the intensity of the driving laser pulse is charted and on the abscissa the reciprocal coefficient of the intensity is plotted. The (linear) colour scale shows the magnitude of the harmonic intrinsic phase.

$$\alpha_q^{(short)} \approx \frac{1}{27} \alpha_q^{(long)} \tag{3.24}$$

This means that the change of the driving laser intensity in one half-cycle has a greater effect on the phase of the long trajectory than on the phase of the short one. Looking on the instantaneous frequency change (chirp) produced by the intensity alteration, one obtains

$$\Delta\omega_q^{(j)}(t) = -\frac{\partial S_q^{(j)}(t)}{\partial t}. \tag{3.25}$$

This leads to a spectral broadening as well as a reduction of the coherence length, which is important for phase matching, which will be introduced later. Analogously to the temporal pulse profile one can consider the influence of the radial intensity distribution of the (Gaussian) laser profile on the phase. In figure 3.8 the spatial and temporal modification of the phase and the wavelength is presented. In the figure the focus is assumed to be exactly within the harmonic generation medium, hence there is no contribution of the Gouy-phase. To consider the whole collected phase, one has to involve the changing intensity around the focus. It is given by

$$I(z) = \frac{I_0}{\sqrt{(1 + \frac{4z^2}{b^2})}}, \tag{3.26}$$

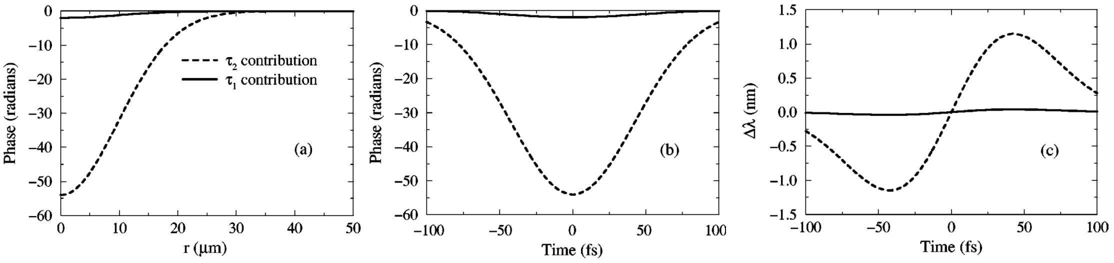

Figure 3.8: From [47]. In (a) the phase variation for the two main paths over the spatial extension of the laser beam are shown, in which r is the distance to the centre of the laser beam. τ_2 represents the long and τ_1 the short path. In (b) the phase behaviour in time is plotted over one pulse cycle. Finally, (c) shows the chirp corresponding to figure (b).

where z is the position relative to the focus and $b = \frac{2\pi w_0^2}{\lambda}$ is the confocal parameter, in which w_0 is the focus size and λ the central wavelength of the laser. Figure 3.9 presents the phase change due to the intensity change around the focus (Gouy-phase), the dipole-phase and the effective phase variation.

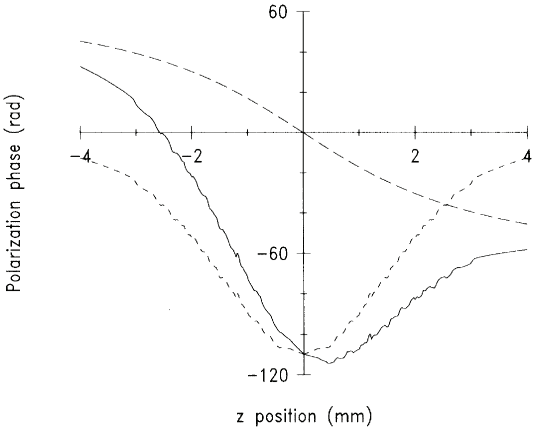

Figure 3.9: From [48]. Phase varying in dependence of the position of the generation medium, where $z = 0$ is the focus position. The long-dashed line shows the Gouy-phase and the small-dashed line represents the dipole phase as in figure 3.8(b). The solid line is the sum of the two phase effects.

In the following, the harmonic spectra in this model shall be analysed. Therefore, one has to solve the propagation equations within the slowly-varying-envelope approximation [49, 50]. With the dipole moment of equation (3.21) as source term it yields in cylindric coordinates [47]

$$\nabla_{\perp}^{2} E_q(r,z) + 2ikq\frac{\partial E_q(r,z)}{\partial z} = -\frac{q^2 k_1^2}{\varepsilon_0} P_q(r,z), \tag{3.27}$$

where $E_q(r,z)$ and k_q are the electric field and the wave vector of the q-th harmonic and P_q its polarisation field that is equivalent to the product of atomic dipole moment and atom density. This has to be calculated for several points in time. Out of it, the space- and time-dependent electric field of the q-th harmonic $E_q(r,t)$ results and the spectrum can be calculated by Fourier transform the near field profile and integration over the transverse direction:

$$I_q(\omega) = \int \left| \int_{-\infty}^{\infty} E_q(r,t) \exp(i(\omega - q\omega_0)t) dt \right|^2 2\pi r dr. \tag{3.28}$$

In figure 3.10a the harmonic spectrum of the 15th harmonic is drawn, the harmonic-generation medium is positioned before the focus and the interference between the contributing quantum paths is clearly visible. This phenomenon is called **quantum path interference**. If we now have a look at what the spectrum looks like on the other side of the focus, another effect has to be considered: the phase matching, which will be explained in the next section. The long trajectory collects too much phase and, therefore, it is suppressed. There, the interference patterns disappear and the harmonic signal seems to be purer (see figure 3.10b).

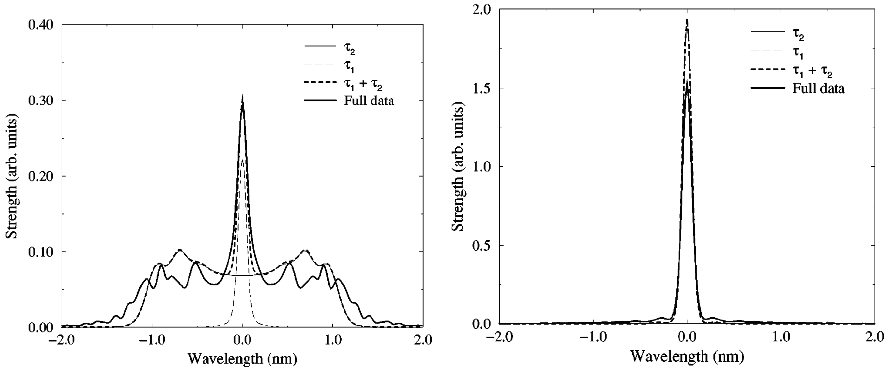

(a) Quantum Path Interference.

(b) 15th Harmonic without interference.

Figure 3.10: From [47]. The calculated spectrum of the 15th harmonic (a) generated in front of the focus. The interference between the quantum paths is clearly visible. Graph (b) shows the harmonic generated behind the focus. Only the short quantum path has a significant contribution to the spectrum.

3.4 Macroscopic Build-up

3.4.1 Phase Matching

Until now we only considered the HHG of a single atom but what is measured in the laboratory, is a macroscopic signal, consisting of many photons per laser shot. This requires that the emitted radiation is in phase with the fundamental laser field over a major part of the high-harmonic conversion volume (atomic gas cloud) and, therefore, with the signals of all contributing atoms. Then, the single microscopic waves emitted from each atom in the medium can interfere constructively with each other and increase the total intensity to a macroscopically detectable signal. For the phase-mismatch of the q-th harmonic to the fundamental field the following equation can be set up [51]

$$\Delta k = qk(\omega_f) - k(q\omega_f), \tag{3.29}$$

where ω_f is the fundamental wavelength. Several physical effects contribute to the wavelength dependence of the wave vector k. First of all, the index of refraction of the harmonic-generation medium is wavelength-dependent. Thereafter, there is a contribution of free electrons (plasma) that do not recombine to produce high harmonics. Only few electrons contribute to the HHG; the remaining free electrons form a plasma, that also affects the refractive index. Finally, the geometrical propagation and focussing of the laser leads to a change of the k-vector. To sum it up, one can write

$$k = k_{vac} + k_{disp} + k_{plasma} + k_{geom}, \tag{3.30}$$

where

$$k_{vac} = \frac{2\pi\omega}{c} \tag{3.31}$$

is the wave vector in the vacuum. For its mismatch one yields

$$\Delta k = \Delta k_{vac} + \Delta k_{disp} + \Delta k_{plasma} + \Delta k_{geom} \tag{3.32}$$

with

$$\Delta k_{vac} = q\frac{\omega_f}{c} - \frac{q\omega_f}{c} = 0. \tag{3.33}$$

Neutral Dispersion

Every medium used for HHG exhibits with a wavelength dependent refractive index $n(\omega)$. Out of this refractive index the wave vector results in

$$k_{disp}(\omega) = (n(\omega) - 1)\frac{\omega}{c} \tag{3.34}$$

and the mismatch is given by

$$\Delta k_{disp} = qk_{disp}(\omega_f) - k_{disp}(q\omega_f) = (n(\omega_f) - n(q\omega_f))\,\frac{q\omega_f}{c}. \tag{3.35}$$

Therefore, the neutral dispersion is only dependent on the difference of the two refractive indices of the generation medium. The refractive index for the near infrared is always $n_{NIR} > 1$ and the index for the extreme ultra-violet(XUV) radiation mostly $n_{XUV} < 1$ the phase mismatching is always positive

$$\Delta k_{disp} > 0 \tag{3.36}$$

For completeness it shall be mentioned, that the refractive index is also dependent on the pressure; the more atoms in the interaction region, the higher the refractive index. In a low-pressure regime, where HHG usually occurs, it can be approximated as linear dependent. So, the pressure can be used to control this contribution.

Plasma Dispersion

Unfortunately, most of the ionised electrons never recombine with their parent ion to emit high-harmonic radiation. Instead, they build a free-electron plasma. It also has a wavelength dependent refractive index and this is defined as

$$n_{pl}(\omega) = \sqrt{1 - \left(\frac{\omega_p}{\omega}\right)^2} = \sqrt{\left(1 - \left(\frac{N_e}{N_c(\omega)}\right)\right)}, \tag{3.37}$$

where ω_p is the plasma frequency $\omega_p = \sqrt{\frac{e^2 N_e}{\varepsilon_0 m_e}}$, N_e is the density of free electrons and N_c the critical plasma density. If $N_c = \frac{\varepsilon_0 m_e \omega_c^2}{e^2}$ is reached, electro-magnetic radiation at frequency ω_c is efficiently absorbed by the plasma. As in typical HHG conditions one is far away from the critical density, we can approximate eq.(3.37) by

$$n_{pl}(\omega) \approx 1 - \frac{1}{2}(\frac{\omega_p}{\omega})^2. \tag{3.38}$$

For the k-vector it yields

$$k_{pl}(\omega) = (n_{pl}(\omega) - 1)\frac{\omega}{c} = -\frac{\omega_p^2}{2c\omega} \tag{3.39}$$

and correspondingly

$$\Delta k_{pl} = q k_{pl}(\omega_f) - k_{pl}(q\omega_f) = \frac{(1-q^2)\omega_p^2}{2cq\omega_f}. \tag{3.40}$$

In general, the harmonic order is $q \gg 1$, the distribution of the plasma dispersion is negative:

$$\Delta k_{pl} < 0. \tag{3.41}$$

This component is dependent on the plasma density, which is regulated by the ionisation and the pressure. So it is sensitive for the pressure and the intensity of the laser.

Geometrical Dispersion

The geometrical distribution discussed in this paragraph, is important for HHG in a small gas cell. The fundamental laser beam has to be focussed to reach the high intensities that are required for HHG. Around the focus, the phase of the laser beam changes. As usual, a Gaussian beam is assumed. For the diameter of a focussed Gaussian beam, which is dependent on the position on the propagating axis of the laser, with $z = 0$ being the focal position, one obtains

$$w(z) = w_0 \sqrt{1 + \left(\frac{z}{z_R}\right)^2}, \tag{3.42}$$

where w_0 is the beam size in the focus and it can be calculated as

$$w_0 = \frac{f}{\pi w_l}\lambda, \tag{3.43}$$

where f is the focal length of the lense used and w_l the beam size at the lense and, finally, z_R is the Rayleigh length, which is defined as

$$z_R = \frac{\pi w_0^2}{\lambda}. \tag{3.44}$$

For the phase evolution one obtains

$$\phi_{foc} = -\arctan\left(\frac{\lambda z}{\pi w_0^2}\right) = -arctan\left(\frac{z}{z_R}\right). \tag{3.45}$$

Now, the wave vector can be derived from the phase:

$$\boldsymbol{k}(\boldsymbol{r}) = \boldsymbol{\nabla}\phi(\boldsymbol{r}). \tag{3.46}$$

In the discussed case it is

$$k_{foc}(\omega) = -\frac{d\phi_{foc}(z)}{dz} = -\frac{2}{(b + \frac{4z^2}{b})}, \tag{3.47}$$

where b is the confocal parameter and is given by $b = 2z_R$. This only affects the fundamental laser beam, therefore the phase mismatch is given by

$$\Delta k_{foc} = qk_{foc}\omega_f - \underbrace{k_{foc}(q\omega_f)}_{=0} = -\frac{2q}{(b + \frac{4z^2}{b})}. \tag{3.48}$$

This distribution is always $\Delta k_{foc} < 0$ and its strength varies with the focal position.

Total Phase Matching

With these three distributions to the phase mismatch one can write this into one equation

$$\Delta k = \Delta k_{disp} + \Delta k_{plasma} + \Delta k_{geom} \tag{3.49}$$

$$= (n(\omega_f - n(q\omega_f)))\frac{q\omega_f}{c} + \frac{(1-q^2)\omega_p^2}{2cq\omega_f} - \frac{2q}{(b + \frac{4z^2}{b})}. \tag{3.50}$$

It will be shown later, that Δk has to be as small as possible to increase the output of harmonic radiation. There are some parameters that have an influence on the wave-vector's mismatch:

- Intensity and pulse duration of the laser
- Focal length
- Position of the gas cell in relation to the focus
- Pressure in the gas cell
- Type of gas

3.4.2 Absorption and the Phase-Matching Factor

The harmonic radiation typically lies in the XUV- regime, where light is extremely well absorbed in matter. This is due to the fact that in most materials, the valence electrons are bound with energies between 10 and 100 eV. Therefore, the cross-section σ is very high for this spectral range. So the reabsorption in the generating medium may be a limiting factor. The distance after which the intensity of light, propagating through a medium, decreased to $\frac{1}{e}$, is called absorption length

$$L_a = \frac{1}{\rho\sigma}, \tag{3.51}$$

where σ is the cross-section for photo-ionisation and ρ is the particle density. The fundamental laser pulse is generating continuously new harmonic radiation. The yield of the q-th harmonic can be calculated by considering that harmonic radiation, generated at different points in the medium, has different travel distances in the medium and by integrating over the interaction distance. One obtains [52]

$$I_q \propto \left| \int\limits_0^L \rho A_q(z) \exp\left(-\frac{L-z}{2L_a}\right) \exp(i\varphi_q(z)) dz \right|^2, \tag{3.52}$$

where $A_q(z)$ is the harmonic amplitude of the single-atom response and $\varphi_q(z)$ is the phase at the exit of the medium and L the medium length. This equation can be written in a different way as

$$I_q \propto \frac{4L_a^2}{1+4\pi^2\left(\frac{L_a^2}{L_c^2}\right)} (1 + \exp\left(-\frac{L}{L_a}\right) - 2\cos\left(\frac{\pi L}{L_c}\right)\exp\left(-\frac{L}{2L_a}\right)), \tag{3.53}$$

where L_c is the coherence length. It is defined as

$$L_c = \frac{\pi}{\Delta k}, \tag{3.54}$$

with the phase-matching Δk. The equation in dependence of the interaction length L is plotted in figure 3.11 for different ratios between L_c and L_a. One can see that the coherence length is relevant. It is possible to estimate that L_c should be sufficiently high ($L_c > 5L_a$) and L_a limits the harmonic generation. The medium length should be at least $L > 3L_a$ but it does not have to be too long, because the intensity saturates with growing medium length.

In the considered geometry, where the laser is sent through a small gas cell (typically a few millimeters interaction length) to generate high harmonic radiation, the absorption length can be approximated as being longer than the medium length $L \ll L_a$. With this, one can approximate equation (3.53) by letting the absorption length go towards $L_a \to \infty$. It yields

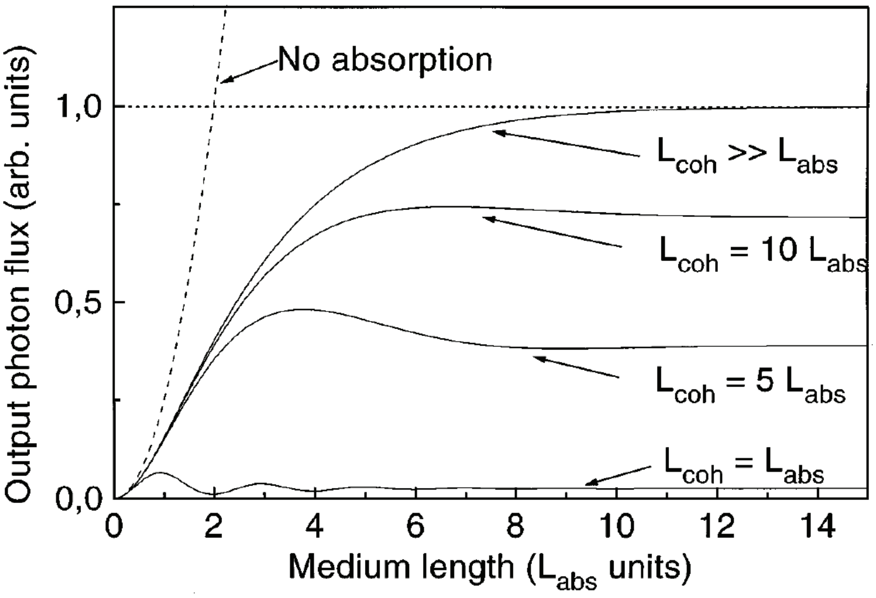

Figure 3.11: From [52]. The output intensity in arbitrary units in relation to the medium length in units of the absorption length.

$$\lim_{L\to\infty} \underbrace{\frac{4L_a^2}{1+4\pi^2(\frac{L_a^2}{L_c^2})}}_{\to\frac{L_c^2}{\pi^2}} \left(1 + \underbrace{\exp\left(-\frac{L}{L_a}\right)}_{\to 1} - \underbrace{2\cos\left(\frac{\pi L}{L_c}\right)\exp\left(-\frac{L}{2L_a}\right)}_{\to 2\cos\left(\frac{\pi L}{L_c}\right)} \right) \tag{3.55}$$

$$= \frac{L_c^2}{\pi^2}\cdot(2+2\cos\left(\frac{\pi L}{L_c}\right)). \tag{3.56}$$

With the trigonometric identity

$$\cos(2x) = 1 - 2\sin^2(x) \tag{3.57}$$

the harmonic yield can be written as [53]

$$I \propto sinc^2\left(\frac{\pi}{2}\frac{L}{L_c}\right), \tag{3.58}$$

where $sinc(x) = \frac{\sin(x)}{x}$ and L_c the coherence length as defined in equation 3.54.

The resulting formula 3.58, which is called **"phase-matching factor"** as introduced

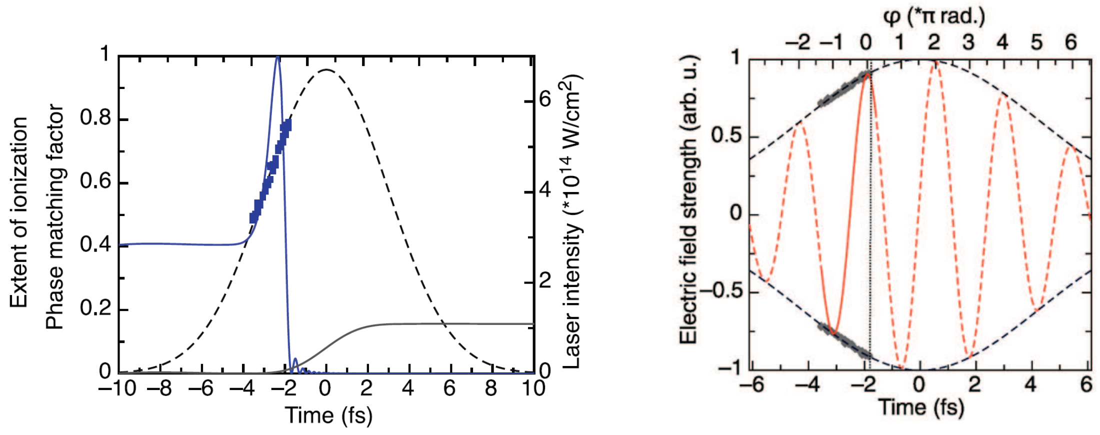

Figure 3.12: From [53]. The high-harmonic generation efficiency (blue line) on the left side for a pulse with 7 fs FWHM and 6.7×10^{14} W/cm^2(dashed line). The grey line represents the number of ionised electrons (in units of the total number of atoms in the generation medium). On the right side the electric field and its envelope of the same pulse is shown. In the region, where the electric field is drawn with a solid line, harmonic generation is observed in the experiment, and in the dashed-line region the "gate" is closed.

in [53], will be discussed in detail in the part "Simulation" but taking into account that the coherence length $L_c = \pi/\Delta k$ with Δk being the phase mismatch the analysis of this equation will tell us that settings can be found, in which the phase matching allows HHG only in a small temporal region within the laser pulse (see figure 3.12). This is because the phase-matching conditions at any given place in the generation medium change as a function of time, as a plasma builds up throughout the temporal evolution of the laser pulse. Since mostly the generated plasma-induced phase mismatch contributes, as will be shown later, this phenomenon is called **Ionisation Gating** (or phase-matching gating) and it explains some experimental observations, especially in the half-cycle cutoffs, which will be defined and explained in the upcoming chapter.

3.4.3 Half-Cycle Cutoff Observation

In the previous chapters it has been shown that in every half-cycle of the fundamental laser pulse a bunch of harmonic radiation is emitted. This leads to a broad harmonic spectrum with discrete lines, separated by $2\omega_f$. The harmonic generated with the highest photon energy for a given half-cycle within the laser pulse is called half-cycle cutoff (HCO). The resulting signal in the time domain is a pulse train consisting of the harmonic emission from all half-cycles. By using shorter and shorter pulses, it cannot be assumed anymore that the electric-field amplitude is equal in every cycle. For this reason, and in the case of a few-cycle pulse, the CEP becomes an important quantity. For instance, if the CEP is $\varphi_{CE} = 0$, the pulse is cosine-like and in this case there is only one half-cycle (the center half-cycle of the pulse) producing the highest photon energies. In contrast, at a CEP of $\varphi_{CE} = \frac{\pi}{2}$, there are two equal-amplitude half-cycles in the electric field of the laser pulse that could contribute to HHG [54].

Observing the cut-off energies of the half-cycles in figure 3.13, it can be found that these maximum energies are not dependent on the peak intensity of the driving laser pulse's envelope, but on the local peak field strength of the oscillating electric field corresponding to the half-cycle. The earlier defined cut-off law $E_{CO} = I_p + 3.17U_p$ can now be applied to every half-cycle of the laser pulse and thus reads [11]

$$E_{CO} = I_p + 3.17U_p(t) = I_p + \frac{3.17}{m_e}\left(\frac{eE_{HCM}}{2\omega_f}\right)^2 , \tag{3.59}$$

where E_{HCM} is the local peak field strength of the electric field of the considered half-cycle. In the harmonic spectra, these HCOs can be found as local maxima of HHG emission at certain photon energies.

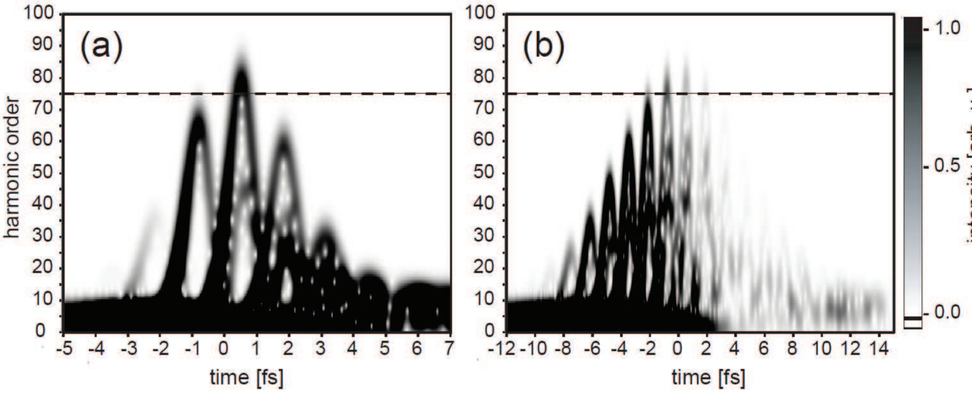

Figure 3.13: From [51]. The photon energies (in units of the harmonic order) are plotted versus time, where t=0 denotes the peak of the driving laser pulse for (a) a 4 fs and (b) a 10 fs pulse. It becomes clear that the maximum photon energies emitted within each half-cycle follow the local field strength of the laser pulse.

So, the individual half-cycle cutoff energies are correlated with the electric field strength of the corresponding half-cycle (see figure 3.13 and 3.14). Now, changing the CEP moves the carrier wave under the envelope and thus the HCO photon energies vary as they follow the local intensity given by the square of the electric-field envelope of the driving laser pulse. One has to note that the actual electric field and the energy of the HCO are separated by a constant phase difference $\Delta\varphi$ that is based on the effect that the highest E_{kin} is not associated with a certain electric-field strength, at which the electron is ionised or recombined, but from the evolution of the electric field that accelerates the electron on its trajectory until it recombines [53, 54].

It was proposed to use the HCOs as possibility to measure the absolute CEP [11, 55] instead of the f-2f-method, previously explained, and with which only a relative CEP can be determined. In the CEP-dependence of the HCOs also the ionisation gating is visible. The measurements show a behaviour of a sudden determination of the evolution of the HCOs at a certain photon energy. This can be explained by the strong dependence of phase matching on the number of ionised electrons (plasma density), which affect the plasma dispersion. Is the electron density too high the "ionisation gate" closes and no more harmonic radiation is generated at later times.

Isolated Attosecond Pulses In figure 3.15, two calculated harmonic spectra are plotted for two different CEPs. In one case a continuum region is produced. In this calculation, a very short cosine-like pulse produces this spectrum (without ionisation gating). A broadband isolated attosecond pulse can then be obtained by spectrally selecting the continuum range of photon energies by a suitable filter.

For longer pulses the available bandwidth for an isolated pulse is much smaller (cp. figure 3.16(a)) and the continuum will not appear in a full spectrum. For such pulses only ionisation gating (coupled with a suitable spectral filter) enables the production of broadband isolated attosecond pulses as illustrated in figure 3.16(b).

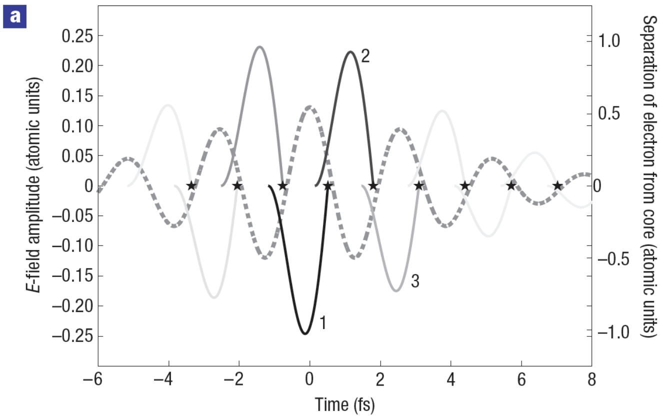

Figure 3.14: From [11]. The dashed line shows a few-cycle pulse and the solid lines represent the trajectories of the electrons leading to the HCOs, which are calculated with the strong field approximation. They have their origin at a phase of the driving laser pulse of ≈ 18° and the recombination point in time, which is denoted by the stars, is at the zero-crossing of the electric field, thus leading to the highest-kinetic recollision energy for any given half-cycle. The grey scale is proportional to the generation-efficiency for the process discussed in [11].

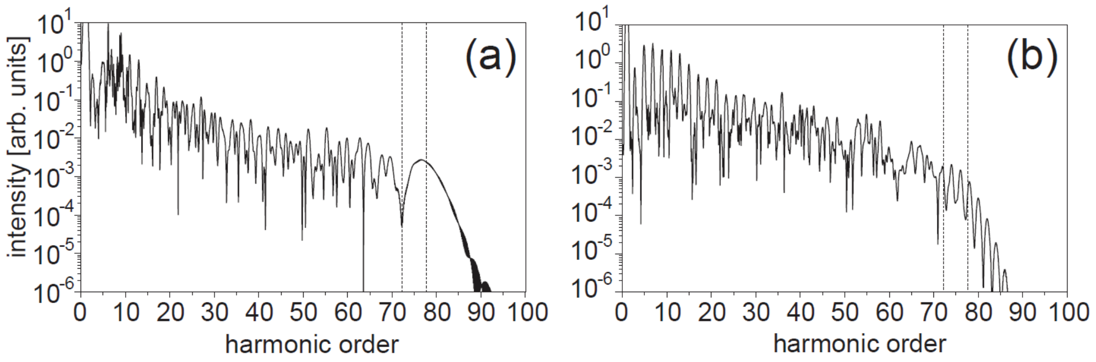

Figure 3.15: From [30]. Simulated harmonic spectra for a two-dimensional H-atom for (a) a 4 fs pulse and (b) for a 10 fs pulse. In the cut-off region a continuum structure is visible for the shorter pulse, whereas for the longer pulse fringes appear, modulated with twice the fundamental frequency. The vertical dashed-lines represent the FWHM of a band-pass filter. In case (a), a single attosecond pulse is generated and in case (b) several pulses appear.

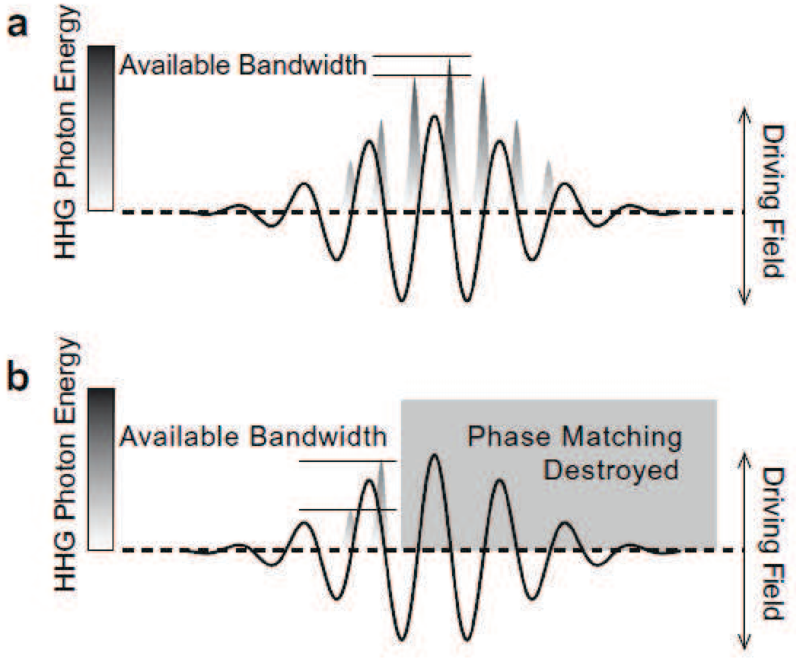

Figure 3.16: From [56]. Two pulses can be seen: (a) without ionisation gating and (b) with ionisation gating. If the lower photon energies are filtered out to get a single attosecond pulse, the resulting bandwidth is significantly greater in the case of the gating and with that the pulse can be shorter.

Part III

Simulation
Phase Matching

4 Simulation - Phase Matching

4.1 Basic Simulation

In this part, a simulation on phase matching will be presented. The theoretical background was discussed in the last part. The simulation is based on the relation between the output intensity of the harmonic radiation generated in a medium with length L and the coherence length [53]

$$I \propto sinc^2\left(\frac{\pi}{2}\frac{L}{L_c}\right), \tag{4.1}$$

called the phase-matching factor, as given earlier, where $L_c = \frac{\pi}{\Delta k}$ is the coherence length which is inversely correlated to the phase-mismatch Δk. It is calculated as introduced above as

$$\begin{aligned} \Delta k &= \Delta k_{disp} + \Delta k_{plasma} + \Delta k_{geom} & (4.2)\\ &= (n(\omega_f) - n(q\omega_f))\frac{q\omega_f}{c} + \frac{(1-q^2)\omega_p^2}{2cq\omega_f} - \frac{2q}{(b+\frac{4z^2}{b})}, & (4.3) \end{aligned}$$

where Δk_{disp} is the phase-mismatch due to the different refractive indices of the generation medium for the driving laser pulse and the harmonic radiation, Δk_{plasma} comes from the effects of the produced free-electron plasma with the plasma frequency ω_p, Δk_{geom} is based on the influence of the focussing geometry of the fundamental beam with its centre frequency ω_f, q is the harmonic order, n is the refractive index, b stands for the confocal parameter and, finally, z is the position of the generation medium, where $z = 0$ is the position of the focus. In addition, there is no difference in the simulation between placing the generation region in front of or behind the focus, since only z^2 appears in equation 4.3.

In the simulation, dispersion effects on the focussing are neglected, it is assumed to be independent of the pressure in the harmonic-generation area. In the experiment, effects such as self-focussing, or plasma defocussing may occur and change the propagation and the phase evolution of the fundamental laser beam within the gas cell, which will cause problems by comparing the calculated results with the measured data.

The simulation was implemented in LabView [57]. It is achieved for the propagation axis only and atomic units are used throughout. As driving laser pulse the envelope of a 6 fs pulse is assumed with a central wavelength of 800 nm and a tunable intensity.

In the simulation we can switch between the actual CEP-stabilised oscillating and the temporal-averaged electric field. In the case the real electric field is used, the ionisation gates are much sharper in time and it is not clear (and not yet studied) if in reality the involved processes react fast enough to follow the actual field or if they only see an averaged field. For a better analysability we decided to do the simulations with the averaged electric field and since both settings lead to very similar results. The simulation will be presented for neon as medium for the HHG but with the used ADK-equation to calculate the tunnel-ionisation rate, other gases could be easily inserted. The refractive indices for the driving laser wavelength were taken from [58] and those for the soft X-ray regime were found in reference [59]. The ionisation potentials are from [60]. The generating-medium length is set as 3 mm, which is similar to the experimental setup used for this work. The presented results are calculated for the 81st harmonic order and the given peak field strengths are in general the field strengths in the generation medium if not declared otherwise.

4.2 Phase-Matching Factor

First, the phase-matching factor will be looked at. As seen in the previous part, apart from the generating medium, the laser intensity, the pressure in the generation medium and the position of the cell are the three main properties, which influence the phase mismatch and can be varied in the experiment more or less easily.

One can see in figure 4.1 that settings can be found where phase matching is given at the leading edge of the driving laser pulse and only very well fulfilled in a small time window. After the steep rising a fast decreasing of the harmonic yield can be observed. This behaviour of the phase matching is responsible for the possibility to produce single attosecond pulses with a broad spectrum and the visibility of the half-cycle cutoffs only for a short region of the leading edge of the pulse, as described in [53, 55]. On the other hand, it is also possible to find settings, where phase matching is achieved all over the driving laser pulse. Also, adjustments can be found where only at the trailing edge a good phase matching is reached and the production of harmonic radiation at the leading edge is suppressed. This is visualised in figure 4.2, which shows in addition, how sensitive the trailing edge gating is against intensity fluctuations. In principle, with these adjustments it should be possible to see the half-cycle cutoffs at the trailing edge, but this has never been observed yet.

In the following chapters, the influence of intensity, pressure and cell-position will be analysed more exactly.

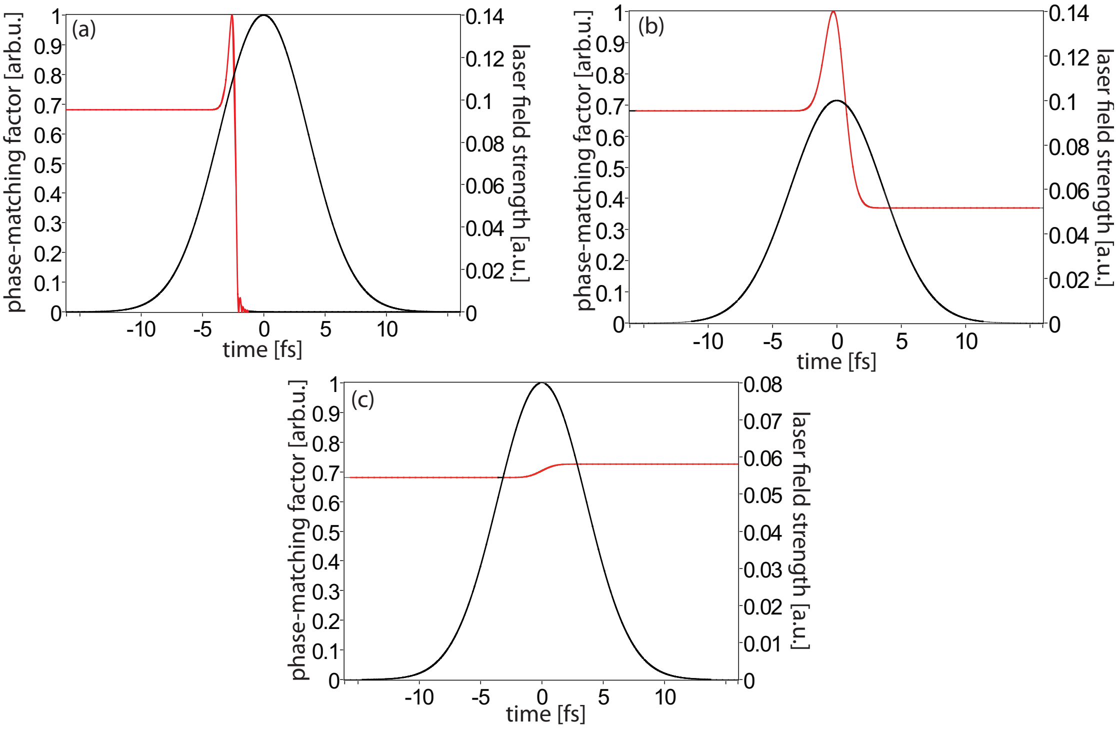

Figure 4.1: Simulated phase-matching factor (red line) for 125 mbar neon filled in the gas-cell positioned 6.8 mm behind the focus for (a) a peak field strength of I=0.14 a.u., (b) for I=0.10 a.u. and for (c) a peak field strength of I=0.08 a.u. of the envelope of the driving laser pulse (black line).

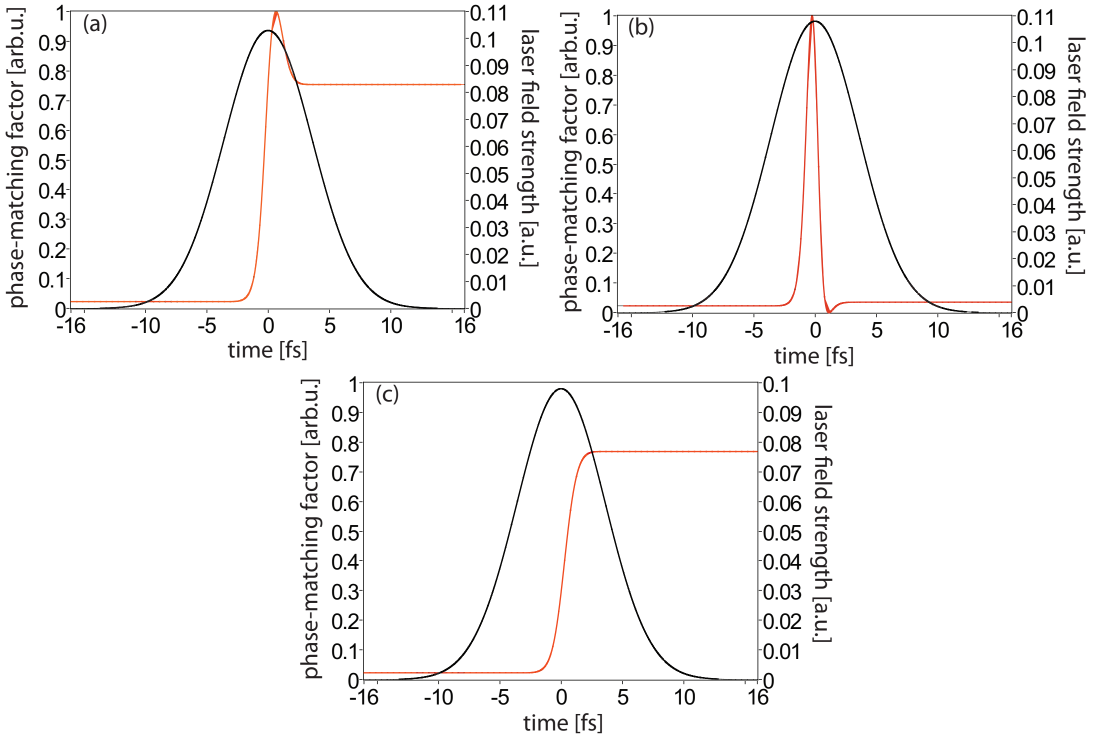

Figure 4.2: Phase-matching factor (red line) for 113 mbar pressure of neon in the gas cell, which is placed 9 mm behind the focus and a pulse (black line) with (a) 0.103 a.u. (b) 0.108 a.u. and (c) 0.098 a.u. peak field strength.

4.3 Intensity-, Pressure-, and Position-Dependence

For the analysis of the influence of the three parameters, in this section two of the parameters are fixed and the third is varied. The results are plotted in an intensity map, where the colour-scale represents the phase-matching factor. Figure 4.3 shows such plots for a fixed cell-position as a function of the pressure for several field strengths. As can be seen, by changing only the pressure, the existence or the absence of the gating behaviour cannot be effected. At low field strengths, phase matching is achieved over the whole pulse. With increasing field strength, the right side of the cut-off region needs higher pressure to come in a phase-matched regime. In contrast to the leading-edge side of the cut-off, where the phase-matched region is not influenced by increasing field strength (apart from times that are near the cut-off-time), the needed pressure increases fast. At a sufficiently high field strength, it is no longer possible to reach phase matching on the trailing edge. Leading-edge gating is always possible when the peak field strengths exceeds a certain limit.

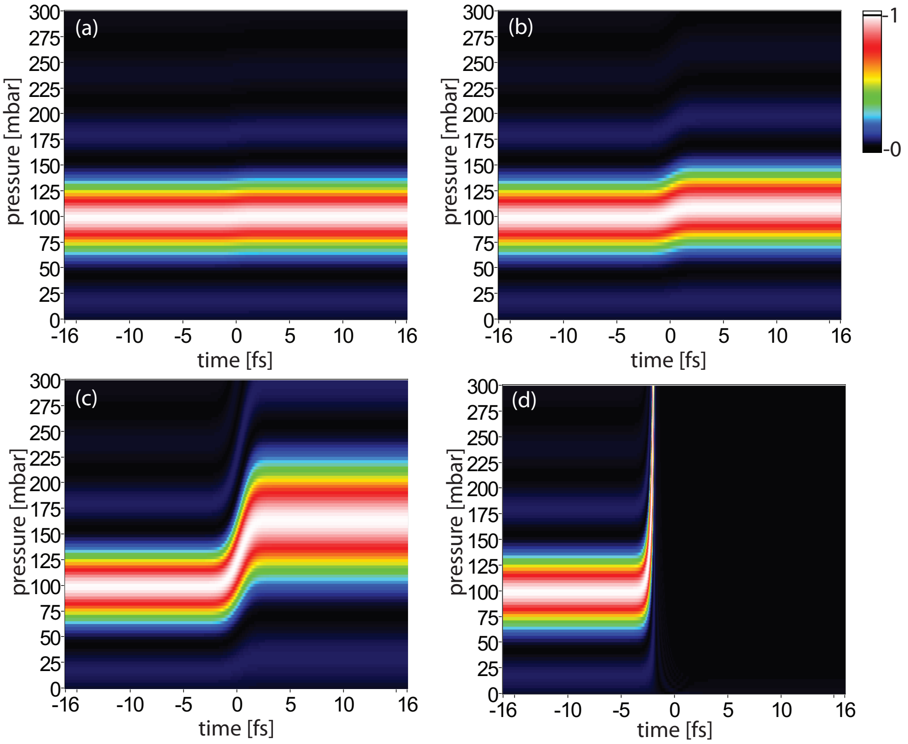

Figure 4.3: Phase-matching factor plotted as colour-scale for different pressures between 0 and 300 mbar and several driving laser pulse peak field strengths (a) 0.08 a.u. (b) 0.09 a.u. (c) 0.10 a.u. (d) 0.14 a.u. field peak strength and a fixed cell position 7 mm behind the focus.

Next, the same graphs can be plotted for different cell positions relative to the focus and fixed peak field strength, shown in figure 4.4. There are plots for two different distances between the cell and the focus. It can be seen that the variation in the position leads to a changing of the pressure, where phase matching is achieved but only the pressure-regime alternates as systematic investigations at different intensities show (not presented here). A cut-off or an overall phase matching cannot be generated by changing the cell's position alone.

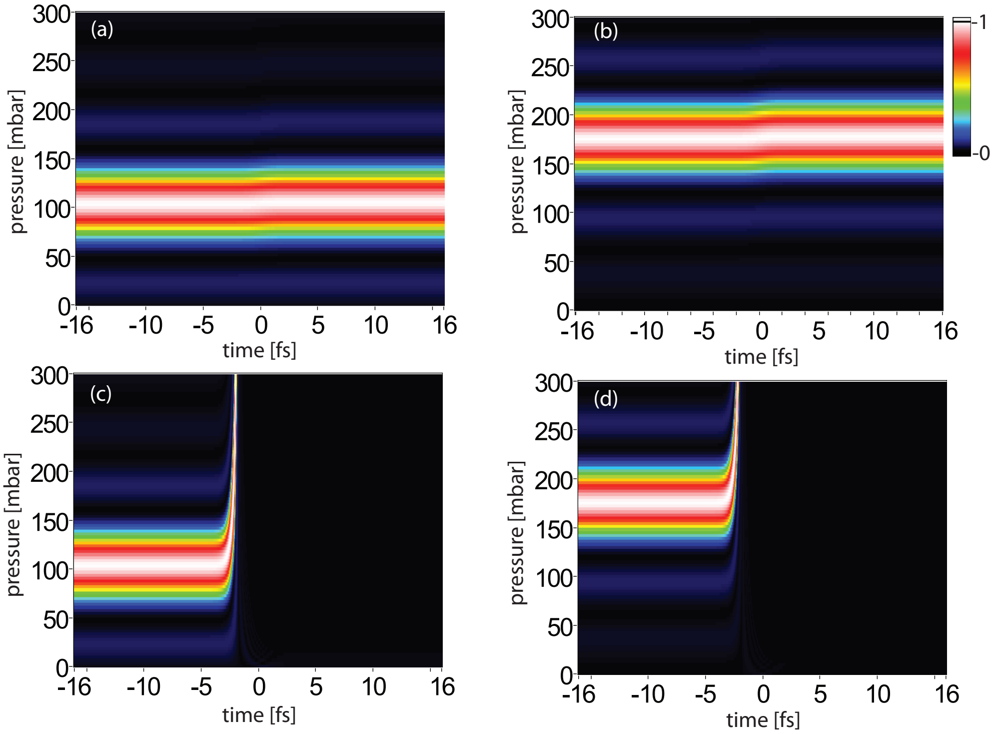

Figure 4.4: Phasematching-factor plotted as colour-scale for different pressures between 0 and 300 mbar, with 0.08 a.u. field peak strength at (a) 6.8 mm and (b) 5 mm and with 0.14 a.u. peak field strength at (c) 6.8 mm and (d) 5 mm distance to the focus.

Similar to the colour maps above, now the position of the cell can be varied and the field strength as well as the pressure in the cell are fixed (shown in figure 4.5). The same behaviour as above turns out. A change in the pressure only affects a change of the position where phase matching is achieved, and the chosen field strength decides if there is phase matching all over the pulse, or if there is a cut-off, or if there is a region where at the leading and trailing edge phase matching can be reached.

Changing the field strength determines not only the run of the phase-matching factor‘s curve, it can also be observed that the temporal position of the cut-off varies. With

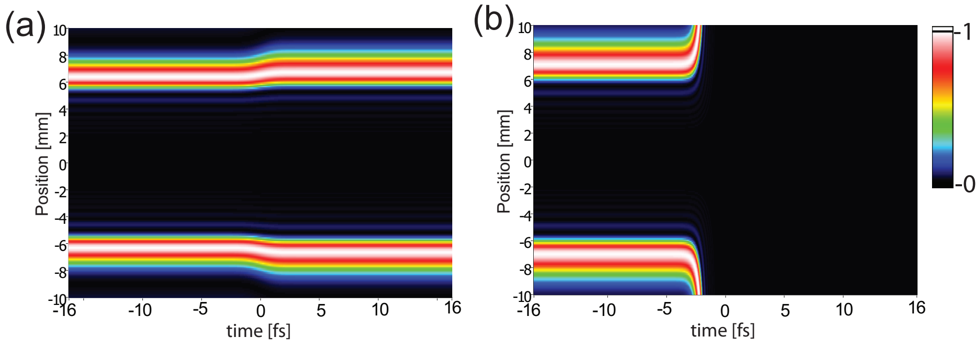

Figure 4.5: Phase-matching factor plotted as colour-scale for different cell positions for 100 mbar neon and (a) 0.09 a.u. and (b) 0.14 a.u. field peak strength of the laser pulses.

growing intensity, the cut-off-position moves towards earlier times. This behaviour is due to the growing ionisation rate at higher intensities. The stronger the driving laser pulse the faster the free-electron density is rising and the increasing plasma frequencies rises the phase mismatch, due to its dependence to the plasma dispersion. In figure 4.6 the peak field strength is plotted versus the corresponding field strength of the pulse at which the gate closes. The cut-off position is determined by inspecting the derivative of the phase-matching factor and finding the maximal negative slope of the function. At lower intensities, before a cut-off exists, this method delivers a wrong number, but the wrong positions can be filtered adequately out (for the prospective cases) in defining a minimal slope to accept it as cut-off. For every setting, the intensity, at which the gate closes, approaches a constant value for higher peak field strengths. The lower the pressure, the higher this approached field strength and the higher the peak field strength that is necessary to realise a gate. By moving away from the focal position, the gate is influenced in a similar way as going to higher pressures.

It was shown earlier that the pressure and the cell position define the degree of phase matching independent of the field strength of the driving laser field. To any (for experiments reasonable) pressure a cell position exists, in which phase matching is fulfilled and vice versa. To visualise this behaviour, a value of the phase-matching factor is picked out at a certain leading-edge-sided time, which is (far) before the cut-off region in any case. Plotted is the highest pressure, where at the chosen point in time more than 90 percent phase matching is achieved (see figure 4.7). This shows that the result is independent of the field strength chosen. The highest pressure, under which phase matching can occur is around 900 mbar when the cell is in the focus. If one looks at positions far away from the focus it can be seen that at some point the pressure for perfect phase matching is not significantly changing anymore. Here, the phase matching is due to the geometrical properties of the setup and this regime is called **geometrically phase-matched**.

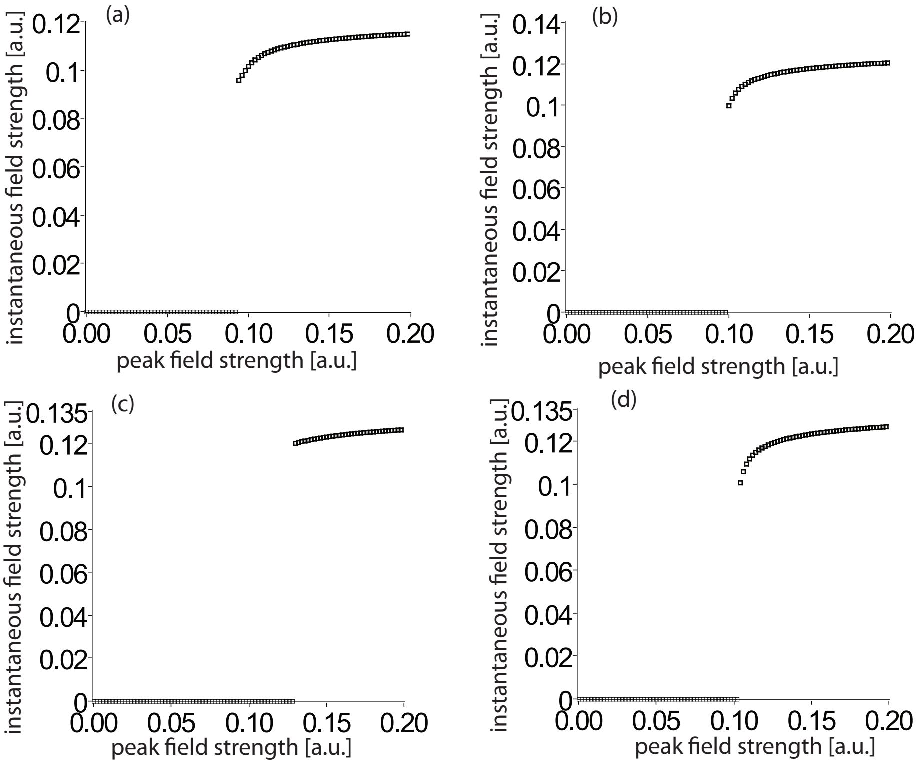

Figure 4.6: Field strength at which the gate closes as function of the peak field strength of the pulse (a) for 100 mbar (b) for 80 mbar (c) for 60 mbar neon at a distance of 6.8 mm to the focus and (d) for 100 mbar and 12 mm.

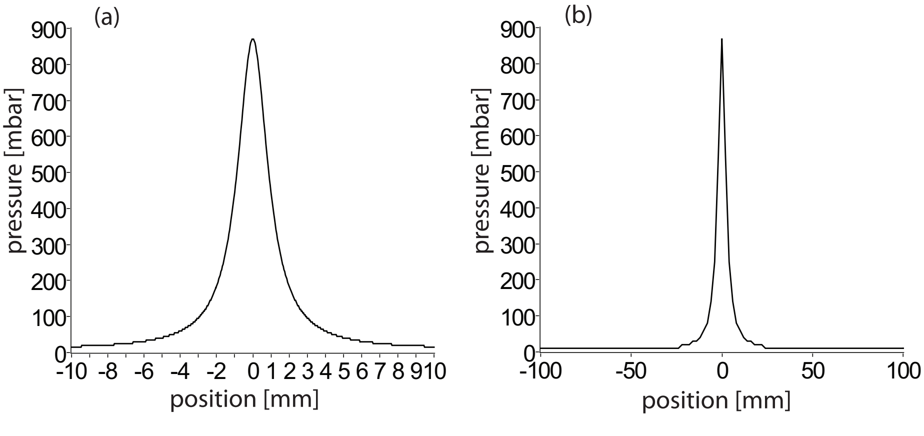

Figure 4.7: Pressure for perfect phase-matching varied from 0 to 900 mbar as function of the cell position varied (a) from -10 to 10 mm and (b) from -100 to 100 mm.

4.4 Quality Parameter

In figure 4.7 no information on the degree of phase matching itself is provided. Therefore, a quality parameter is defined by considering only such settings, in which the phase-matching factor rises above 0.99. Is this condition fulfilled, two values are picked out at fixed times, the first one leading-edge-sided and the second one trailing-edge-sided (again 'far' from the cut-off region) and the difference is calculated.

The range of this parameter is from -1 to 1. Positive values stand for a preference for phase matching on the leading-edge side of of the driving laser pulse. The closer the parameter converges on 1, the better the phase matching on the leading edge and an ionisation gate can be assumed. Similar to that, it behaves for the negative values, where the trailing-edge side is preferred. The closer the parameter is to 0, the more undefinable the resulting phase-matching factor is, since there are the cases included:

- Perfect phase matching during the whole driving laser pulse
- Small differences between the phase matching on leading- and trailing-edge (no cut-off)
- All possibilities, in which the phase-matching factor permanently is lower than 0.99.

In figure 4.8 the quality parameter is plotted for different peak field strengths. The field strengths given before was the field strengths in the harmonic-generation region, here, they are the peak field strength in the focus and the position-dependent field strength is calculated by the behaviour of a Gaussian beam as

$$I(z) = I_{foc} \cdot \frac{1}{\sqrt{1 + (\frac{z}{z_R})^2}}, \tag{4.4}$$

where I_{foc} is the peak field strength in the focus, z_R is the Rayleigh length, the distance between the focus and the distance where the cross section of the beam is doubled and z is the position, where in $z = 0$ is the focus. The bell-shaped graph looks similar to the pressure-position plot in figure 4.7. Following the bell-shaped line, one is in leading-edge phase-match regime. At a certain position, which is dependent on the peak field strength in the focus, phase-matching can theoretically be reached at the trailing edge only (black, blue, turquoise and green array in figure 4.8) but as mentioned above this will be hard to find and has not yet been observed.

The geometrically phase-matched area is not visible in this quality parameter. The field strengths at geometrical phase matching is in a regime, where the cut-off is no longer achieved and the HHG is phase-matched over the whole driving laser pulse, which gives a value near or equal to 0 for the quality parameter.

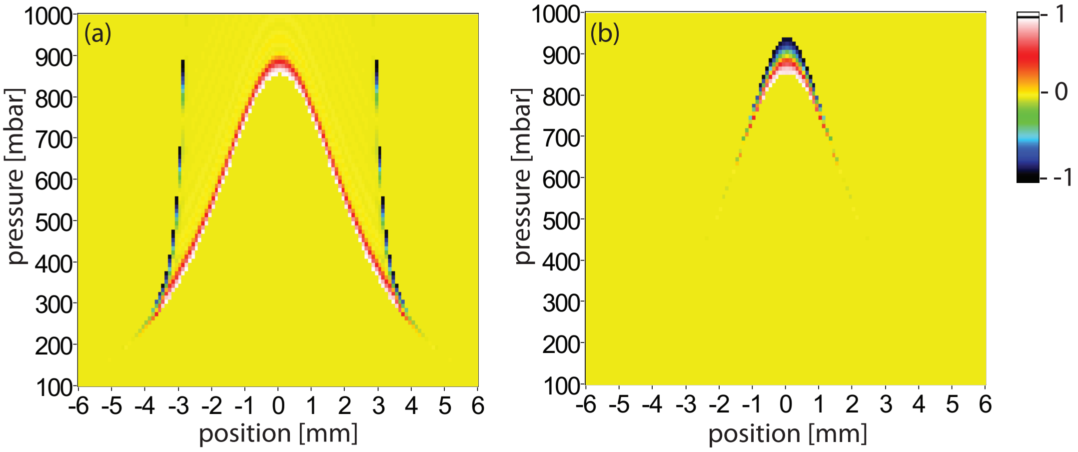

Figure 4.8: Quality parameter as function of pressure and position at (a) 0.11 a.u. and (b) 0.10 a.u. field peak strengths of the fundamental laser pulses.

Part IV

Experimental Setup

5 Experimental Setup

5.1 Laser System

5.1.1 The Titanium:Sapphire Laser

For the experiments in this work a commercially available laser system from Femtolasers [61] was used. The system provides short pulses of less than 30 fs at a central wavelength around 800 nm with a repetition rate of 4 kHz. The laser system is presented in figure 5.1.

Starting point of the system is the oscillator pump laser, a diode pumped solid-state Verdi V6 laser from Coherent [62] that has an output power of 6 W at 532 nm. This pump laser first passes an acusto-optical modulator (AOM), which controls its output intensity, for the CEP stabilisation. The laser is then focussed into a first cavity with a Ti:Sa gain crystal. The pulses from this first cavity are sent through several optics for dispersion control such as dispersion compensating mirrors or simple glass wedges, that are used for the CEP stabilisation, too. The laser already has pulses with pulse lengths less than 12 fs then, and a spectral width of more than 100 nm but the output energy is much too low to use this directly for experiments such as HHG in rare gases. Only several nanojoules output energy can be provided with a high repetition rate of 74 to 78 MHz. Before this beam is further amplified, it is sent through a third-order dispersion-compensating mirror system (TODM). On their way, the pulses propagate through a pulse stretcher (PS), through which the pulses are elongated for further amplification.

Afterwards, the stretched pulses are sent into the second laser cavity. In the round red box in figure 5.1 the second Ti:Sa gain crystal is placed, which has to be cooled down to prevent overheating and it is in a vacuum to obviate condensation on the crystal, on which water drops could act as a lens and focus the laser to strong into the gain crystal. This second Ti:Sa crystal is pumped by another external diode pulse pump laser from Photonics Industries [63] that provides pump laser pulses at 527 nm with a minimal duration of 271 ns and a maximal average power of 57.3 W at 4 kHz repetition rate. The light pulses from the oscillator are led into this second cavity, where they pass the crystal four times on slightly different paths. After the fourth pass, the beam is directed through a Pockels cell, and, afterwards, it passes the gain crystal another five times.

The amplified beam is then reflected into the last part of the laser system, where the beam is re-shortened. It is based on a prism compressor working with four prisms that are traversed twice. The four mirrors in-between the two prism pairs are folding mirrors to keep the system compact. Now, the laser pulses are a bit longer (shorter than 30fs) and have a bandwidth of circa 40 nm. But now the pulses have a repetition rate of 4 kHz at an output energy of 800 μJ corresponded to 30 GW peak power.

5.1.2 Beam line

The pulses provided by the laser system itself are not short enough for the experiments planned. Therefore, the pulses have to be shortened further before they can be coupled into the experiment. At first, the beam is split up into two parts, of which one very small part is led into a CEP controlling system from MenloSystems [64]. The other part is focussed into a thin hollow fibre (length: 1 m, diameter: 250 μm) filled with 1.5 bar argon. In this fibre, the laser pulses are spectrally broadened by self-phase modulation (SPM). As introduced in the fundamentals, the pulses have a significant chirp after being self-phase modulated, which has to be compensated to compress the pulses. This further compression is done with four pairs of chirped mirrors. As mentioned earlier, the dispersion compensation of the chirped mirrors cannot be adapted, but the chirp of the fundamental laser beam can fluctuate from day to day because of external influences as air moisture or a slightly changed beam location. For this reason, the chirped mirrors are built to overcompensate the chirp, thus glass wedges can be inserted to optimise the signal by inserting or taking out propagation distance in glass. Now the laser pulses have a duration of 5-6 fs in an optimal case and a central wavelength of 750 nm at 4 kHz repetition rate. The pulse energy is around 0.4 mJ.

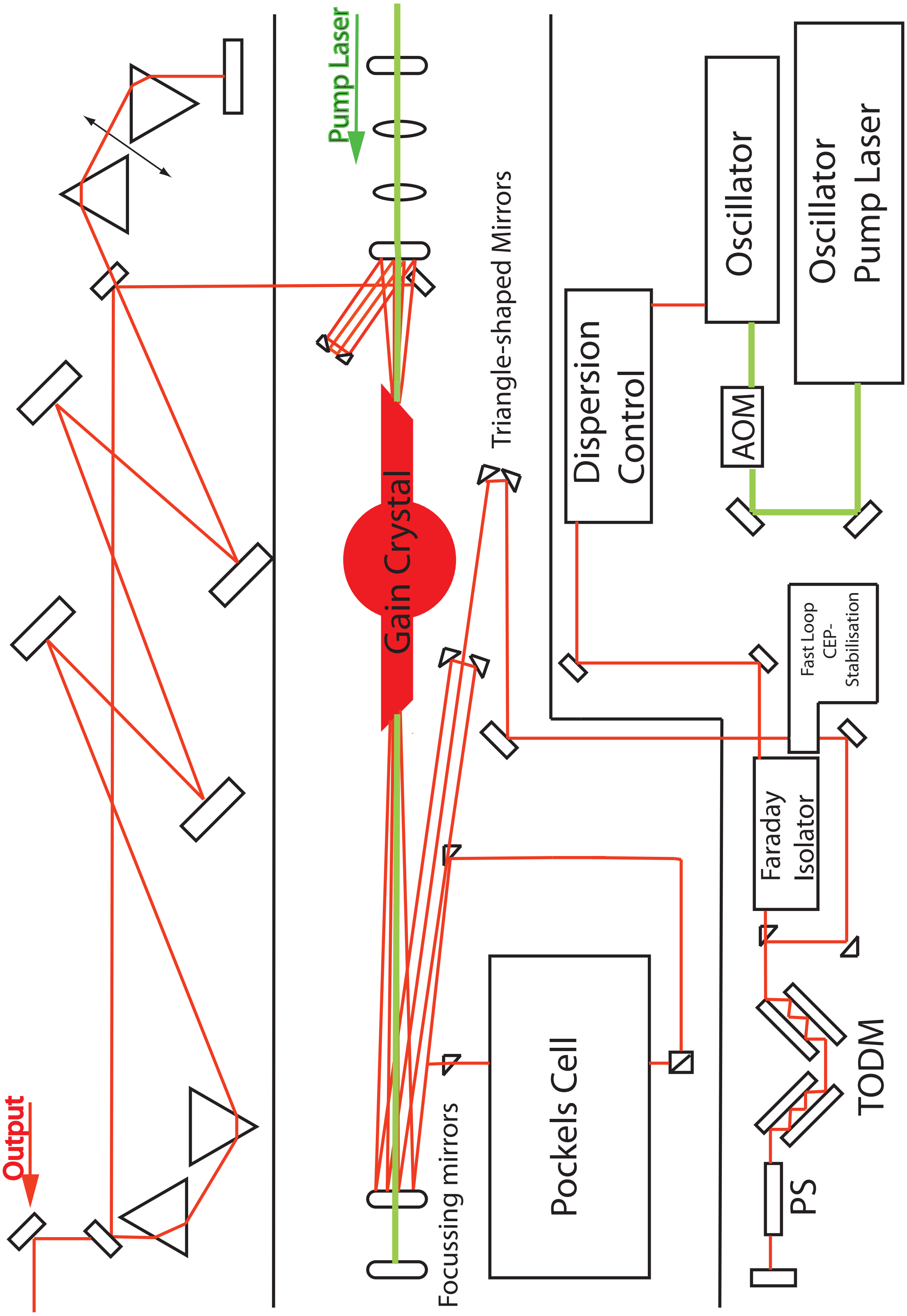

Figure 5.1: Simplified illustration of the laser system used for the experiments in this work.

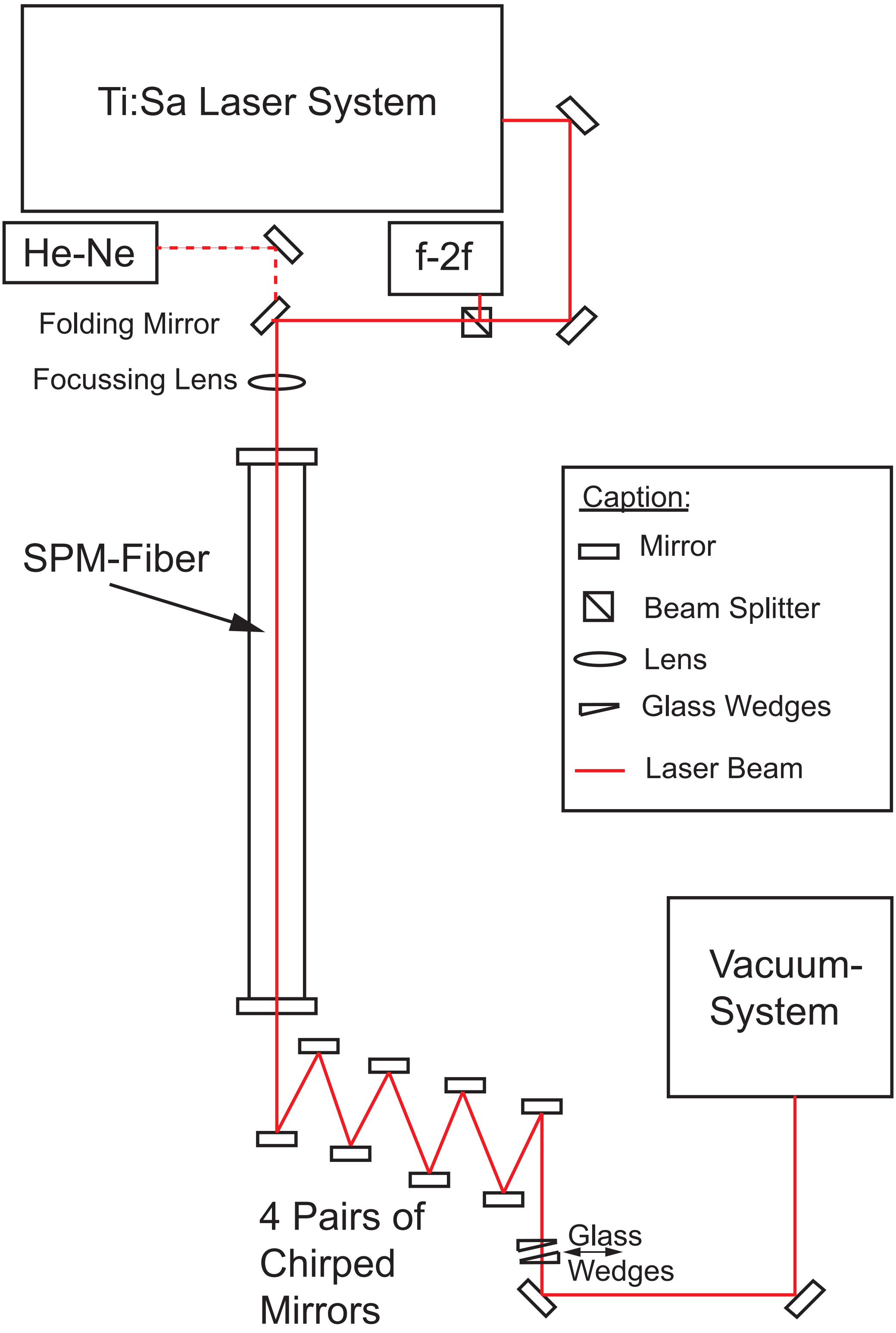

Figure 5.2: Simplified illustration of the beamline between the laser system and the vacuum chambers.

5.2 Vacuum System

5.2.1 Setup Used

Gas Cell for HHG

The vacuum system used for this work is shown in figure 5.5. The laser beam is focussed with a lens with a focal length of 500 mm and coupled into the first vacuum vessel through a thin glass window. This is exerted not planar to the cross section of the beam, but under an angle so that the laser beam hits the glass in Brewster's angle $\alpha_B = 55.5°$ in order to have a minimum of intensity losses through stray light. In this first vessel the gas cell is placed where the HHG occurs. The mount of the generation-cell can be seen in figure 5.3. It consists of an aluminum block, onto which a commercially available three-axis stage is mounted. Onto this stage, a conventional 1 inch mirror support is screwed parallel to the optical table, wherefore a fitting holder for the actual gas-cell is produced. The cell itself can be fixed by sticking it into the holder, where a clamp can be closed via a screw. The gas cell consists of a small steel tube with an inner diameter of 2 mm and a wall thickness of 0.5 mm. Into the wall of the tube, two holes are drilled mechanically and arranged facing each other with a diameter of 100 μm. At the tube's ends flexible PVA tubes are mounted via Swadge Lok connectors. These PVA tubes lead to feed-throughs on the outside of the chamber, where the gas supply can be regulated by a needle valve.

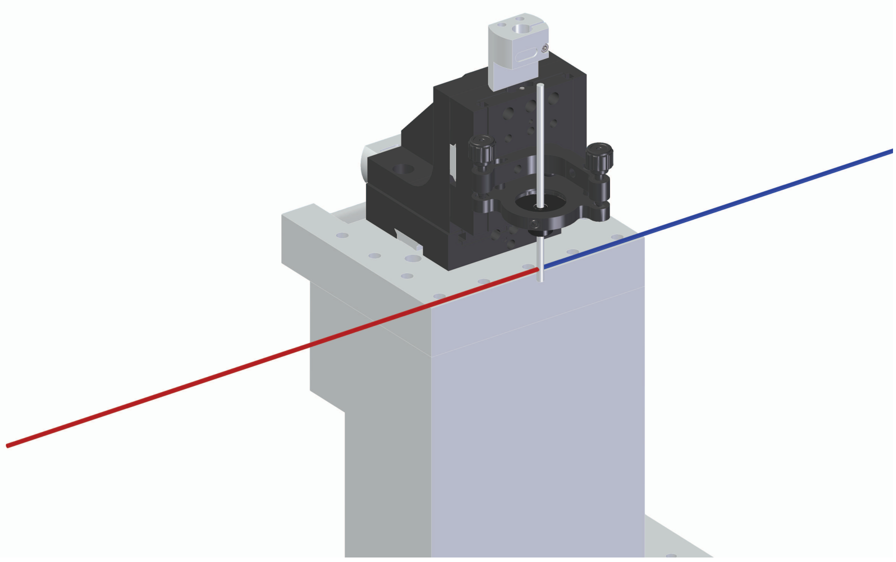

Figure 5.3: Gas cell for HHG.

Spectrometer Chamber and X-Ray CCD Camera

After the HHG, the fundamental laser and the harmonic radiation propagate freely through the next vacuum chambers into the spectrometer chamber. There the beams have to pass thin metal foils. These metal foils are mounted in a box, which is connected to a translation feed-through. As can be seen in figure 5.4 there are two holes in the filter box. At one entry two aluminum foils and at the other opening two zirconium filters are mounted. All four foils are 0.2 μm thick, so that the beams have to pass 0.4 μm of metal altogether. The translation feed-through is used to change the vertical position of the filter box, so it is possible to choose the foil material which is to be set in. For adjustments with the He-Ne-Laser, the filter-box can be totally removed from the beam line.

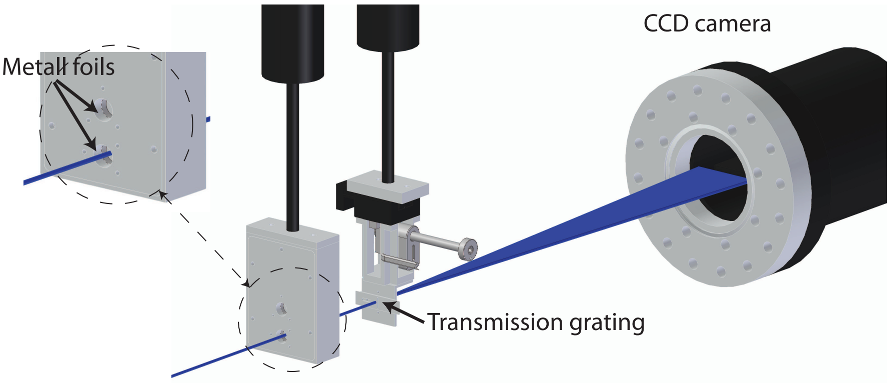

Figure 5.4: Spectrometer chamber with the filter-box, the Si_3N_4-grating and the X-ray CCD camera.

The thin metal foils are used to completely filter out the fundamental laser beam, which would destroy not only the signal but also the grating and the camera. Furthermore, it is possible to select special energy ranges of the harmonic radiation with the foil material (zirconium is transparent for radiation between 60 and 200 eV and aluminum allows for light between 15 and 73 eV to pass). As explained later, especially the aluminum absorption-edge can be used for the calibration of the measured spectra.

The filtered harmonic radiation then hits a transmission grating (100 nm lattice spacing). The spectrally resolved light is then detected by an PIXIS-XO X-ray-CCD-camera from Princton Instruments [65] with a CCD image area size of 26. 8. x 8. 0 mm^2 and 1380 x 400 pixels, with a pixel size of 0.02 x 0.02 mm^2.

5.2.2 Planned Setup Upgrade

The setup used for the experiments in this work was initially the first step and it allows only to observe HHG. But the actual intention is to use the high-harmonic radiation to do spectral interferometric experiments and pump probe experiments in simple molecules.

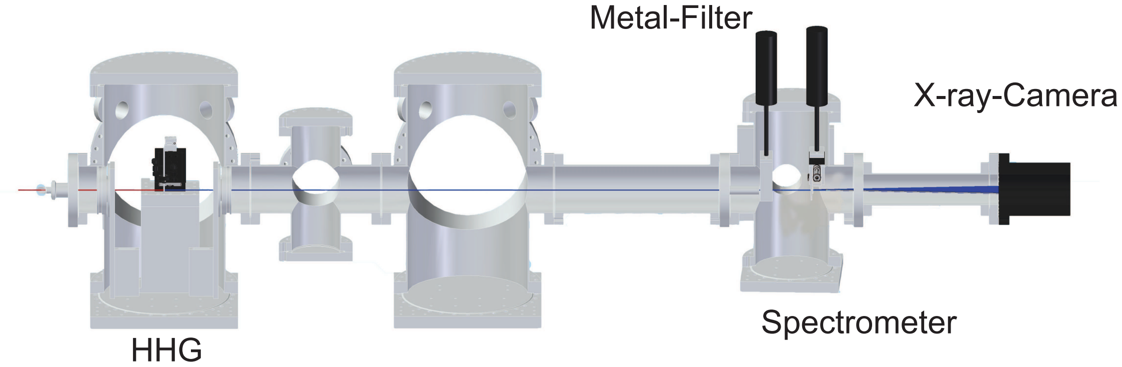

Figure 5.5: Preliminary vacuum setup.

The considered experiments with the upgraded system will be discussed later in the outlook. This first step of the setup was built while parts for the complete configuration were designed and constructed, which consists of the generation cell, followed by a mirror assembly, through which the high-harmonic radiation can be delayed in relation to the infra-red driving laser pulse and refocussed into a second gas cell, in which the target gas is filled. Thereafter, the radiation propagates onto a transmission grating and is observed with an X-ray CCD camera, which will be presented and is shown in figure 5.6.

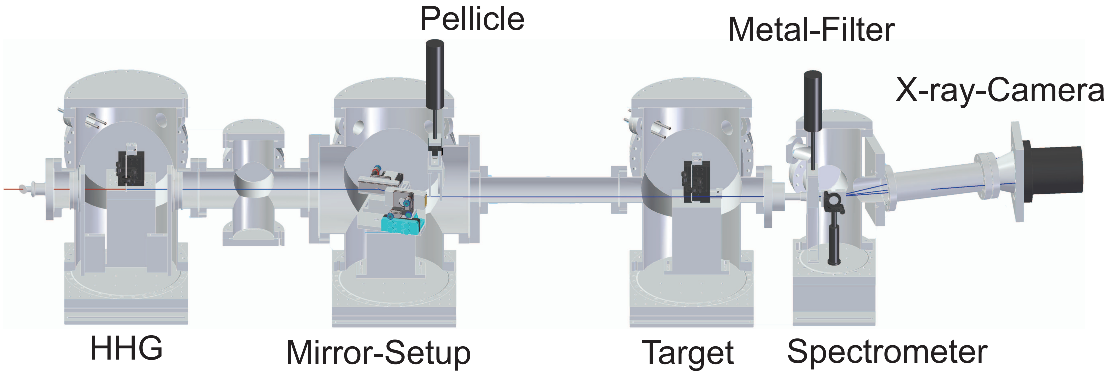

Figure 5.6: Full setup.

HHG and Target

The HHG in this assembly is done with the same construction as described above (see figure 5.3). However, to carry out experiments with a target gas, one needs a second interaction region. It was decided to copy the generation-cell and use it as the gas target for the time-resolved experiments. The fundamental laser beam and the harmonic radiation is focussed into the second cell by a toroidal mirror.

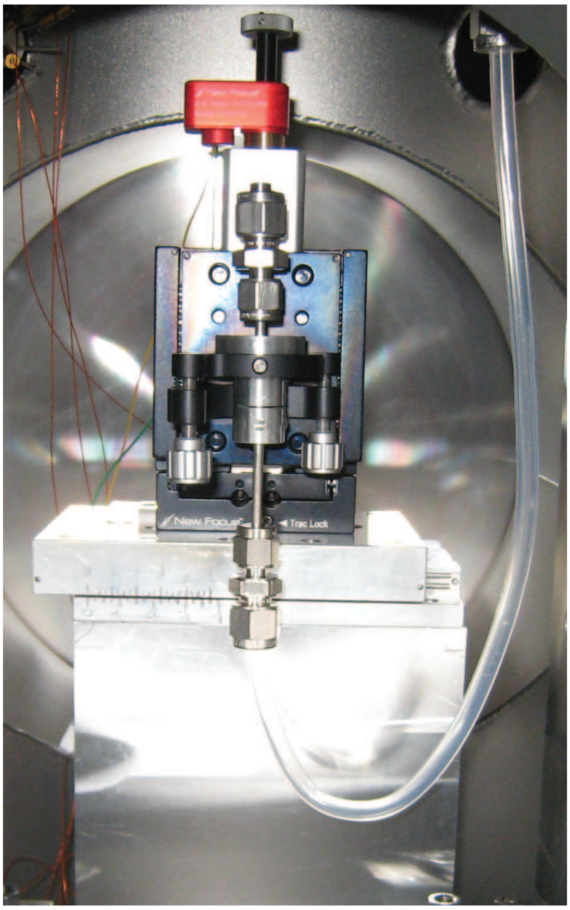

Figure 5.7: Picture of the generation-cell in the HHG vacuum vessel and with a provisional vernier scale to estimate the cell-position.

Mirror Assembly

The mirror assembly is the “core component” of the final setup and shown in figure 5.8. For the pump-probe experiment, it is needed to delay the harmonic radiation against the driving laser pulse. Therefore, a split mirror is used with an outer silver mirror (which is not reflective for the harmonic radiation) with a hole in the middle, where an inner gold mirror is attached. The outer mirror is mounted with an especially designed holding in a common mirror support to adjust its surface planar to the gold mirror. The inner mirror on its part is fixed on a piezo stage to allow for a variation of the distance between the two mirror surfaces. It is possible to move the inner mirror 0.4 μm in 1 nm steps, which corresponds to a modification of the temporal position of the harmonic radiation for 0.4 ps in total in steps of 1.7 as. The stability of the gold mirror was tested and it worked in a quite stable way. Thereafter, both beams are refocussed via a toroidal gold mirror mounted in an especially designed holder for a 4-axis stage.

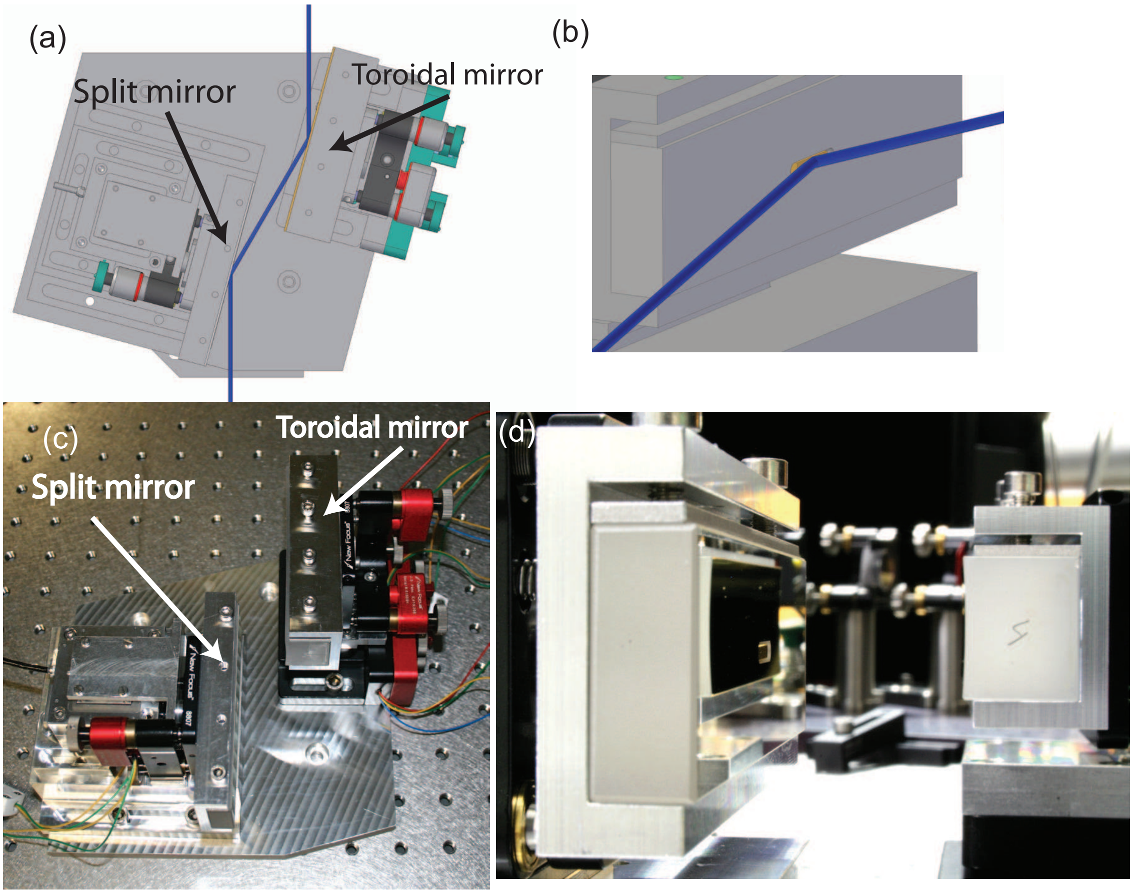

Figure 5.8: Illustration of the mirror assembly as (a) a draft from above, (b) a more detailed view to the split mirror as draft, (c) a photography from above and (d) a view onto the mirrors at the beam plane.

The new idea behind this mirror assembly is to have a monolithic setup, in which both beams propagate into the same direction. It is expected to have a high interferometric stability. Beyond that, the split mirror and the toroidal mirror are both hit at grazing incidence because bandwidth limitations that are associated with the normal incidence on a common multilayer mirror shall be avoided. Figure 5.8(d) shows that the mirrors are planned to be shaped square-like in grazing incidence.

Pellicle

There is a first filter system in the mirror chamber. It consists of a small steel tube with 2 mm diameter, to which a thin metal foil (Al or Zr) of 0.2 μm thickness is installed to partially cut out the fundamental infrared laser beam to prevent disturbing interference in the target region. The metal filter is followed by a commercially available pellicle with a small hole in the middle, which the XUV-Beam can passes through. The pellicle is used to suppress fast diverging low order harmonics. In this filter assembly the possibility to use only the metal filter without the pellicle is integrated.

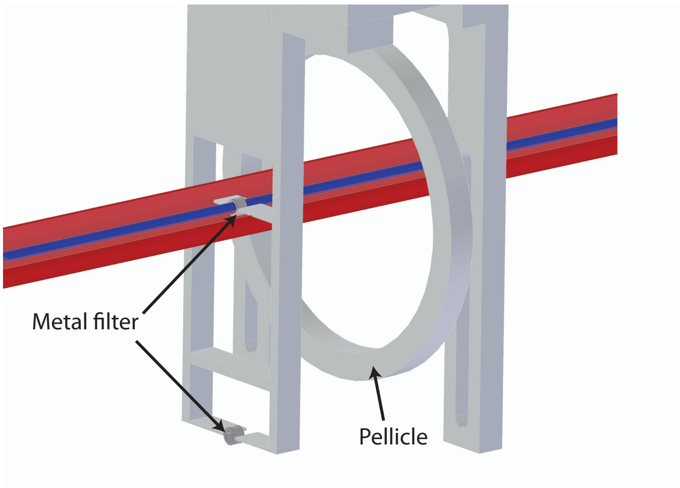

Figure 5.9: Holder for thin metal foils and a pellicle.

Spectrometer Chamber

The last vacuum chamber in the setup is the spectrometer chamber (see figure 5.10). Here, the beams have to pass thin metal filters to totally cut out the IR-Beam. The same filter box as well as the filters described for the setup used are utilised. Thereafter, the filtered XUV-beam hits a reflection grating and is sent to the X-ray CCD-Camera. This camera is connected to the vacuum chamber via an hydroformed bellow and can be moved by a special holding to look at different photon energies in a wide range from ~20 eV to ~120 eV.

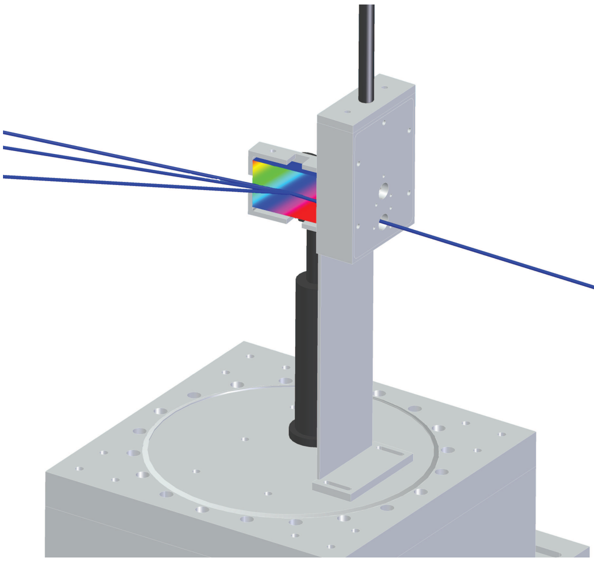

Figure 5.10: Draft of the filter box and the reflection grating in the spectrometer chamber.

Part V

Experimental Results

6 Calibration of the Spectra

In the experiments the harmonic radiation is filtered either by aluminum or zirconium foils to select different energy ranges. Furthermore, especially the absorption edge of the aluminum filter (around 73 eV, or 17.05 nm) can be used to calibrate the spectra. The spectral separation is facilitated by a Si_3N_4 transmission grating with 100 nm lattice spacing. This grating material also absorbs light within the energy range of the observed harmonics (at 12.4 nm, or 100 eV). Therefore, in the measured data, an intensity minimum is visible around 100 eV. The light is detected with a backside-illuminated CCD camera that is sensitive in the XUV range with 1380 × 400 pixels, and a pixel size of 20 μm × 20 μm.

The measured spectra have to be converted from a number of pixels to nanometers of wavelength. To perform this calibration, the 17.05 nm absorption edge of aluminum and the absorption line of the grating material were used. Two pictures are acquired: one with the zirconium filter placed into the beam where the absorption minimum at 12.4 nm is visible and a second one with the aluminum filter at the same camera position where the 17.05 nm absorption edge is visible. Then the pixel numbers of these significant points are read out. The remaining pixels are then interpolated linearly.

Furthermore, the spectra in the energy domain are of interest. Therefore, the spectra have to be converted into the frequency domain at first. Here, one cannot simply change the scale, as done above with the change between the linearly related pixel- and the nanometer-scale, and substitute $\frac{c}{\lambda}$ for ν. For the energy dE passing one slit one obtains

$$dE = S_\nu d\nu = -S_\lambda d\lambda \tag{6.1}$$

$$\Leftrightarrow S_\lambda = -S_\nu \cdot \frac{d\nu}{d\lambda}, \tag{6.2}$$

where S_ν and S_λ are the spectral distributions in the frequency and the wavelength domain, respectively. The derivative in the equation can easily be calculated with the relation $c = \nu\lambda$:

$$\frac{d\nu}{d\lambda} = \frac{d}{d\lambda}\frac{c}{\lambda} \tag{6.3}$$

$$= -\frac{c}{\lambda^2}. \tag{6.4}$$

Now the frequency can be transformed to energy by the linear relation $E = h\nu$. Due to the inverse quadratic dependence of the wavelength in the conversion, the resulting energy bin size is, however, not linear, hence a linear interpolation of the energy scale is necessary. This is particularly important for performing Fourier analysis on the measured photon energy spectra, were an equidistant sampling interval is required by the numerical Fourier transform.

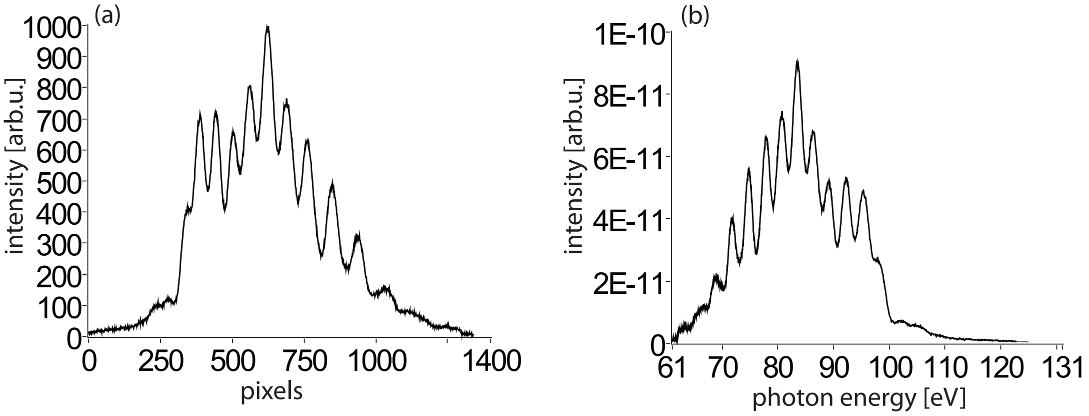

Figure 6.1: Spectrum measured at an unknown z position and with a neon pressure of 125 mbar (a) before and (b) after the calibration from the pixel scale to the photon energy scale.

Pulse Duration and Intensity In the current setup no laser pulse monitoring system is installed. Therefore, we are not able to estimate the pulse durations before or during the measurements. The pulse intensity is also not directly accessible in our system. The averaged continuous-wave (cw) power of the laser is measured before it is coupled into the vacuum system. An upper limit for the intensity of a single pulse can be approximated by

$$I = \frac{P}{\pi \tau f_{rep} w(z)^2}, \tag{6.5}$$

where P is the cw-power, τ the pulse duration, f_{rep} the repetition rate of the pulses and $w(z)$ is the size of the laser beam at position z on the propagation axis and is defined in equation 3.42. In all presented measurements (if not declared elsewise), the averaged power was 1.45±0.02 W, which leads after equation 6.5 to 3.25±0.05 W/cm^2 (which correspond to 0.306±0.002 a.u.), which is much too high.

As it will be shown, the measurements itself provide an opportunity to extract an estimation for the minimum durations of the driving pulses and their intensities we had during the experiments.

7 CEP-independent Measurements

7.1 Structure of the Harmonics

Two-dimensional position resolved spectra (dispersion and spectrometer-slit directions) are shown for two different positions of the gas cell along the propagation axis of the fundamental laser beam in figure 7.1. Picture (a) depicts the harmonic radiation generated in front of and in (b) the generation occurred near the focus. There are clear differences between both images. The spectrum generated near the focus shows a very regular zebra-like structure. The single harmonics have a well-defined and similar width and vertical expansion. On the other hand, substructures appear in the spectrum, in which the generation occurred in front of the focus. The vertical spreading is reduced while there is a spectral broadening of the single harmonics. In addition, the yield of the radiation is much higher.

This effect of different spatio-spectral high-harmonic intensity distributions can be explained by the properties of the different quantum paths, as introduced in section 3.3. In the geometry, in which the gas cell is placed in front of the focus mainly two and even more different quantum paths are contributing to the signal [66]. The radiation emitted by the different paths interferes and interference structures in the measured spectra are visible. As shown above, the longer the quantum paths are, the more sensitive they are to variations in intensity. The nearer the harmonic generation is placed to the focus the less is the contribution of the long quantum paths because they are not phase-matched anymore. The interference patterns are disappearing and the signal seems to be more regular. Furthermore, the fewer quantum paths corresponding to electron trajectories are contributing to the signal the less recombining electrons make a contribution to the resulting signal. The measured yield can, thus, be expected to be lower.

At this point, the measurement of the cell position shall be discussed. In this experimental setup a vernier scale is installed at the translation stage that moves the cell along the beam propagation direction. The focal position was determined by tracing the converging fundamental laser and finding its focus in the vented vacuum vessel and without the gas cell in the beam line. In air the focus is visible due to high intensities in the focus in which the molecules are ionised and a luminescent free-electron plasma is formed. Although the vernier scale can be read out very exactly on less than half a millimeter, an exact determination is not possible in this way. At first, the focus position is slightly changing between the vented and the evacuated system, because of the different focus conditions in air than in the evacuated system as well as for different pressures in the gas cell. Therefore,

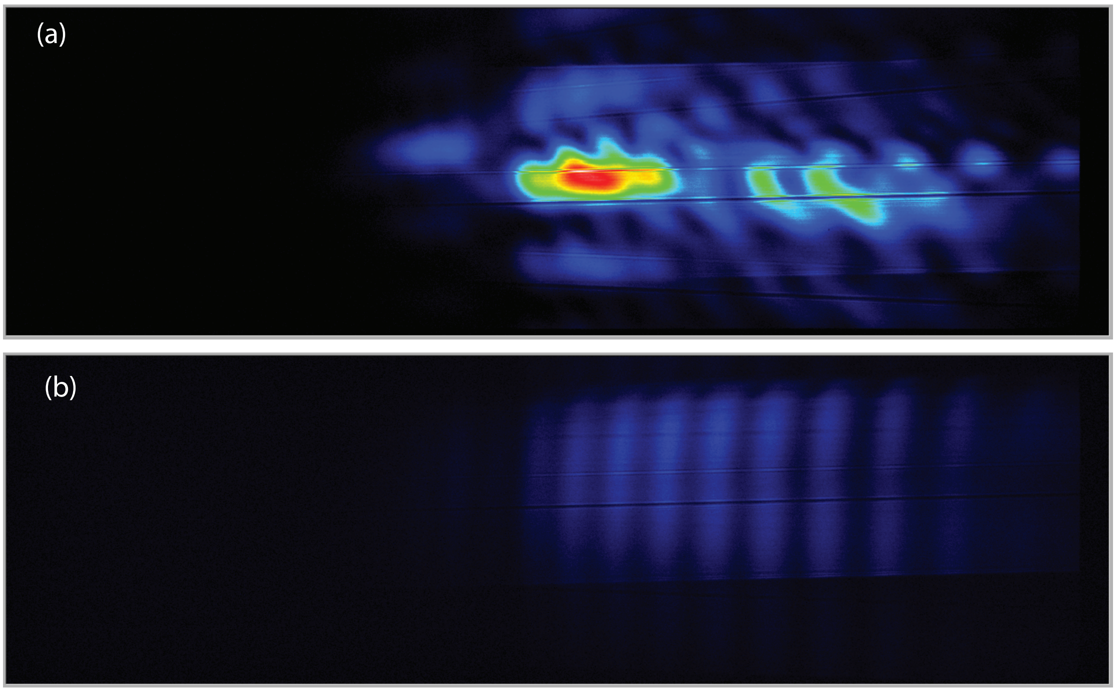

Figure 7.1: Beam profile and harmonic spectrum at 100 mbar neon and (a) 5 mm in front of the focus and (b) 2.5 mm behind the focus.

the insertion of the gas cell in front of the focus has a strong effect on the focal position and the focussing in the gas cell, which will be important later, when the simulation will be compared with the experimental results. The simulation has not included influences on the focussing caused by the gas in the cell.

As soon as the laser hits the gas, some non-linear optical effects may occur that influence the beam propagation and, thus, the position of the focus. Analogously to filamentation [17], self-focussing of the beam, due to the intensity-dependent refractive index and (free-electron) plasma defocussing take place in gases. The strength of these effects is dependent on the pressure in the gas cell, the intensity of the incoming beam, and the position of the cell relative to the laser focus in vacuum. Thus, the effective focal position can change just by changing the pressure. Nevertheless, in the following the denoted z positions are giving with respect to the vacuum focal position.

7.2 Harmonic Yield

In this section, the intensity of the harmonic radiation depending on the gas pressure in the gas cell and its position will be analysed.

7.2.1 Pressure Dependence

For the first measurement presented in this section, the cell position was optimised with respect to the total intensity of the detected signal at a pressure of 24.8 mbar neon. This experiment was carried out before the vernier scale was installed and the cell position could, thus, not be quantified but the cell was placed (far) in front of the focus. The individually acquired single-shot two-dimensional position resolved spectra (dispersion and spectrometer-slit directions) are averaged over the spectrometer-slit direction to obtain one 2D spectrum per adjusted pressure. Thereafter, it is integrated over all energies within the spectrum. As one can see in figure 7.2, the intensity of the harmonic radiation is rising with increasing gas pressure in the interaction region and at low pressures the intensity of the signal increases quadratically with increasing pressure. To clarify this, figure 7.2 (b) shows the low-pressure regime of this and a parabola with apex at 0 pressure and 0 intensity is fitted into the data.

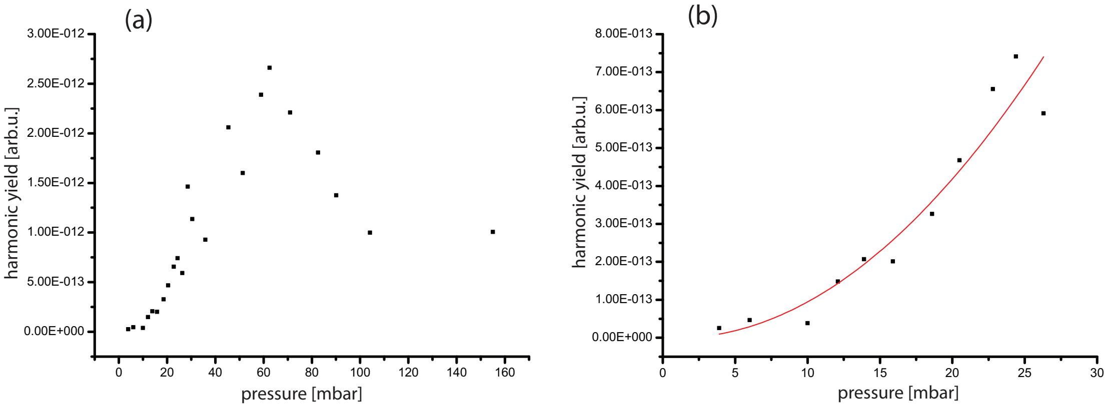

Figure 7.2: (a): Pressure scan at unknown cell position in a regime, in which the HHG is geometrically phase-matched. (b) shows an excerpt of figure (a) and a parabola is fitted to the measured values.

This quadratic increase is a hint that the measurement is done in a regime, in which geometrical phase matching is fulfilled. That means in this setting (for this z-position of the gas cell) the HHG is phase-matched without the introduction of dispersion via the gas and the emerging free-electron plasma. The gas is only needed as generation medium. The intensity of the signal is rising with increasing pressure until, on the one hand, the dispersion introduced in the gas lowers the phase matching and, on the other hand, absorption in neon starts to take place. An absorption limit, at which all harmonic radiation is absorped, can be expected at higher pressures than used in this measurement.

The next data are extracted from the CEP- dependent measurements that are discussed later in detail. For each pressure different spectra for different CEPs were acquired. The CEP is varied over 12.6 rad ($\approx 4\pi$) in steps of 0.2 rad. For the analysis presented in this chapter, the data are integrated again over the energy and then, in addition, it is averaged over all CEP values such that no difference to a floating CEP situation should occur. Three measurements are shown in figure 7.3. Graph (a) is from an experiment performed before the z position of the gas cell could be measured. In (b) the gas cell was placed 6 mm and in (c) 3.75 mm in front of the focus. Unfortunately, the pressure could not be varied in measurement (b) and (c) to pressures as high as the ones shown in graph (a). The drilled 100 μm holes at the input and exit of the gas cell were extended by the fundamental laser and the free-electron plasma within the steel tube. The larger the hole in the gas cell the more gas enters into the vacuum vessel. If the pressure inside the vacuum chamber is too high, the turbo molecular pump shuts down. For these two measurements, it was not possible to see where the yield of the harmonic radiation reaches a maximum but both measurements show a very similar rise of the yield with pressure. In contrast to the geometrically phase-matched regime, in figure 7.3 (b) and (c), a certain gas pressure is needed to obtain phase matching and the harmonic yield stays low until the gas density is balancing more and more the phase mismatch.

The harmonic yield measured in figure 7.3 (a) are much smaller than the yields of the other two measurements (figure 7.3 (b)(c)). One explanation is, that the measurements with known positions (figure 7.3(b) and (c)) are done within the Rayleigh length (=1. 05 cm) of the focussed laser beam. The Rayleigh length is defined as

$$r_R = \frac{\pi w_0^2}{\lambda} \approx 1.05cm, \tag{7.1}$$

where w_0($\approx$50 μm) is the focal waist size of the laser and λ($\approx$ 750 nm) its central wavelength. The other measurement (figure 7.3(a)) is probably done at larger distance to the focus, where the driving-laser intensity and, thus, the harmonic yield is much lower.

7.2.2 Position Dependence

In order to study the influence of the focussing geometry in more detail, the harmonic yield at different positions of the gas cell at fixed gas pressures was recorded and analysed. Three measurements for 60 and 100 mbar of neon in the generation region are shown in figure 7.4. The presented data is extracted from CEP-dependent experiments. It is analysed similarly to the pressure-dependent measurements: The spectra are integrated over the energy and averaged over all CEP values. The two measurements for 100 mbar have a similar peak intensity but their maxima are at different positions. The data was

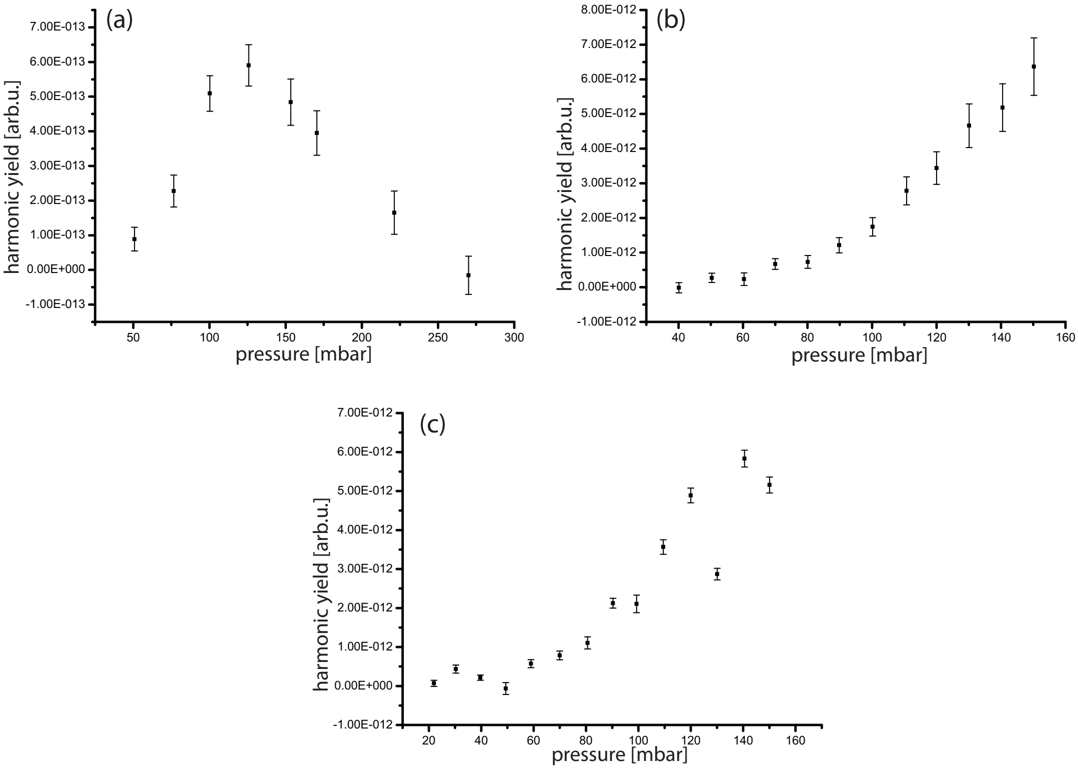

Figure 7.3: Three pressure scans at (a) an unknown position (b) 6 mm and (c) 3.75 mm in front of the focus.

acquired on different days, so some properties as the focal position in vacuum or the pulse properties (pulse duration or peak field strength) may have changed between both measurements. This may have been caused by a slight change of the beam position or a slightly different coupling into the SPM hollow fibre or a non-perfect compression of the laser pulses. This could explain the differences between the measurements but as of now the changes cannot be quantified in our setup.

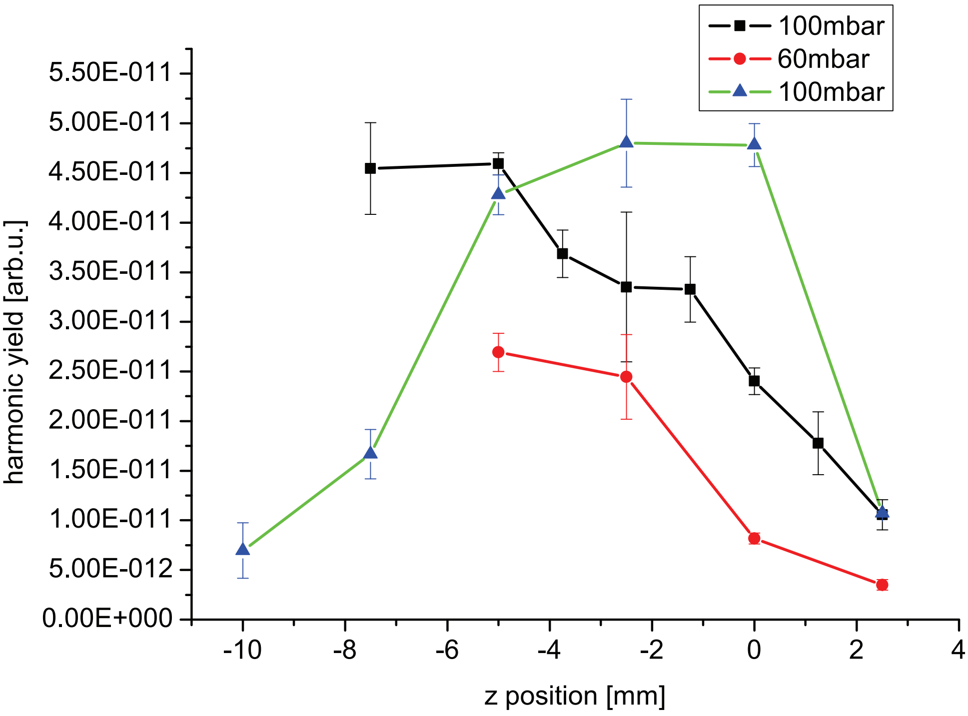

Figure 7.4: Three position scans at 100 and 60 mbar neon.

8 CEP Measurements

8.1 Structure of the Harmonics

To study the CEP-dependence of the high-harmonic spatial beam structure, a certain photon-energy (71 eV for the spectrum measured at z=5 mm in front of and 61.2 eV for z=0.25 mm behind the focus) is cut out of the measured two-dimensional and position resolved spectra (dispersion and spectrometer-slit direction) (see figure 8.1, in which the analysed spectra are shown for one CEP) and the vertical beam profile is analysed for different CEPs of the fundamental laser pulse. The CEP is varied over 12.6 rad in 0.2 rad steps. The measurement was carried out 5 mm in front of the focus (figure 8.2(a)) and 2.5 mm behind the focus (figure 8.2(b)). In both cases, 100 mbar of neon was used in the gas cell. If the harmonic generation occurs in front of the focus, there is a clear CEP-dependence and the local maximum of the harmonic radiation of this photon-energy is moving and changing periodically in intensity in correlation with the CEP. The asymmetry of the structures is likely due to a vertical pressure gradient in the gas cell, since the gas is flowing into the tube from only one direction and the other opening of the tube has an dead end.

This behaviour changes significantly after moving the gas cell behind the focus. There is no CEP-dependence noticeable and the local maximum rather is a plateau than a peak.

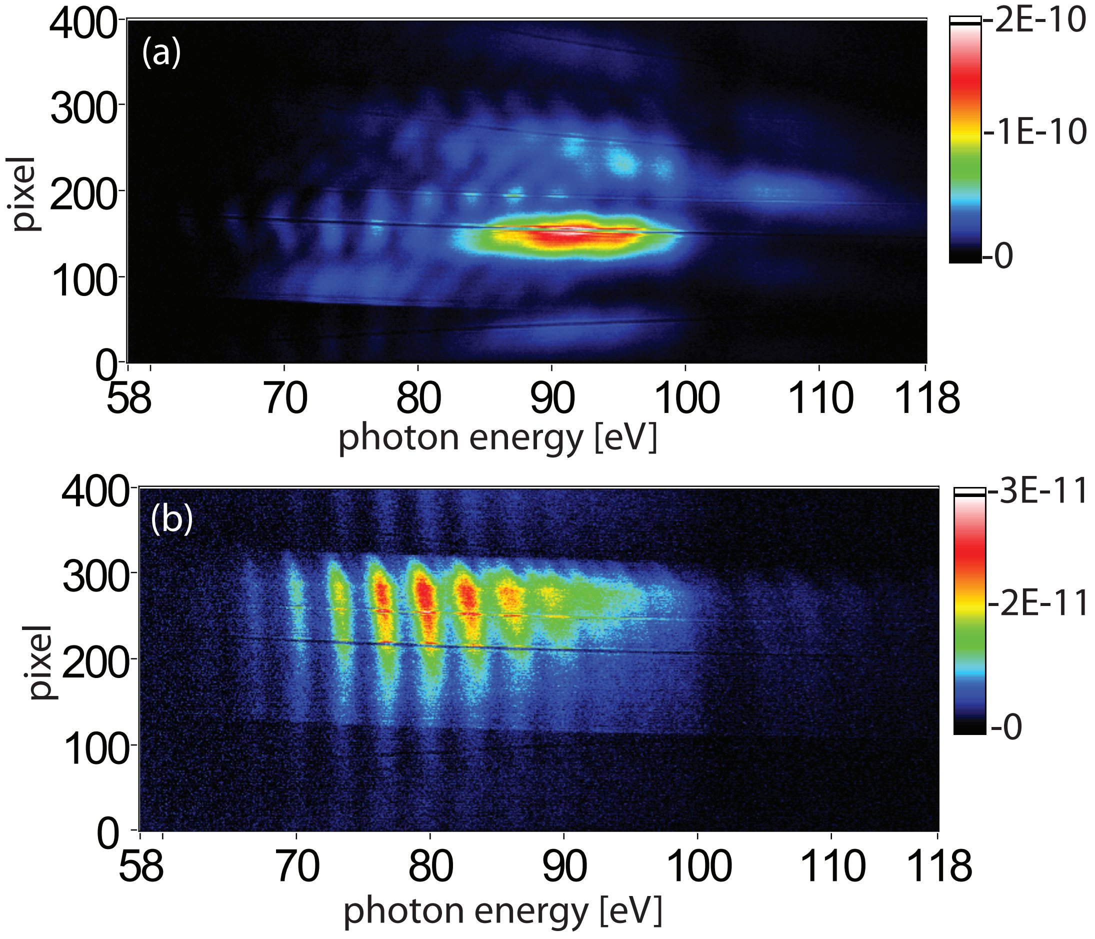

Figure 8.1: Two 2-dimensional and position resolved spectra measured for 100 mbar neon at (a) 5 mm in front of and (b) 2.5 mm behind the focus, both at a relative CEP of -5.0 rad.

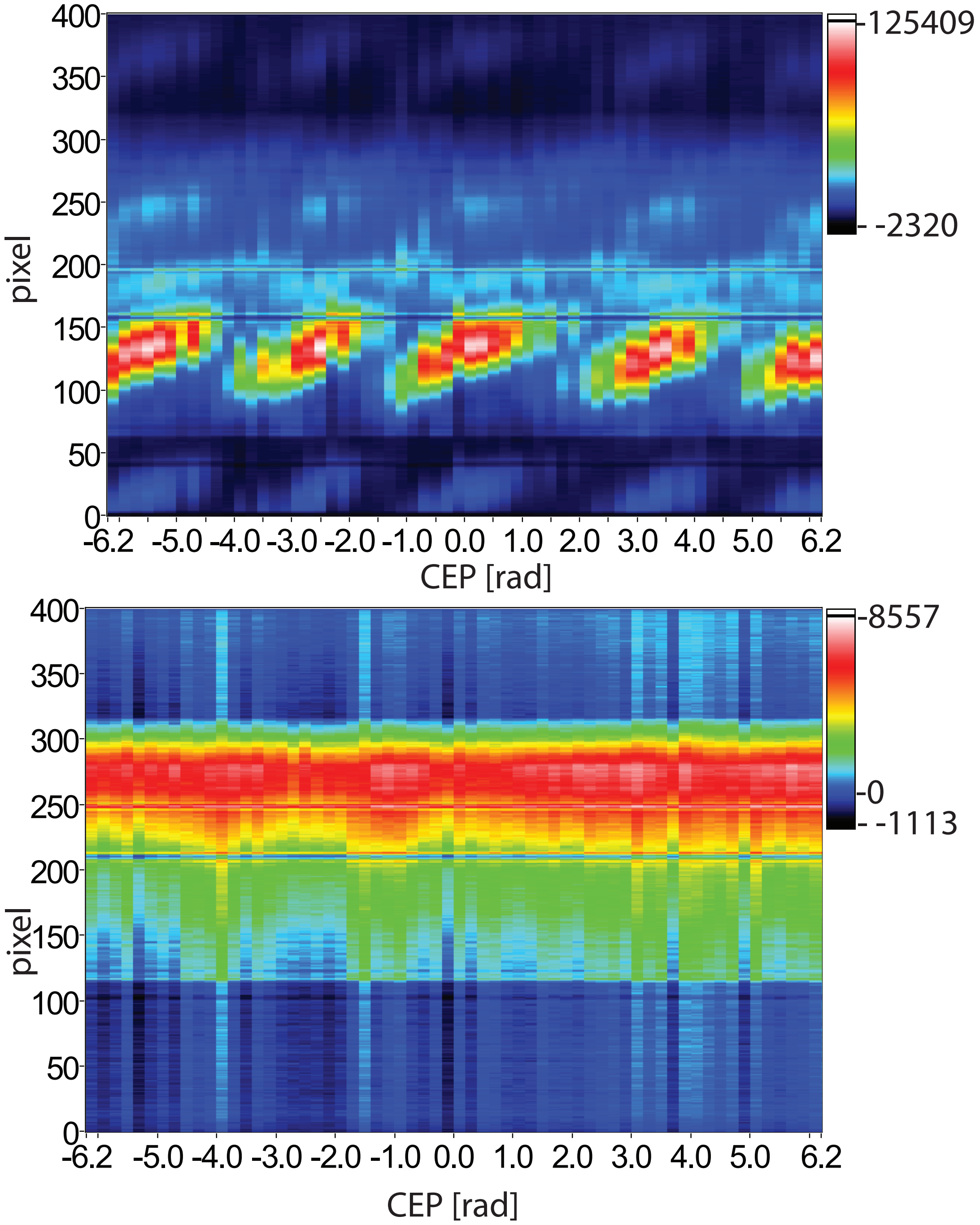

Figure 8.2: Vertical structure of the harmonic spectrum measured with 100 mbar neon inside the gas cell (a) averaged over 1.83 eV starting around 70.12 eV 5 mm in front of and (b) averaged over 1.16 eV starting around 66.65 eV 2.5 mm behind the focus.

8.2 Single Attosecond Pulses

A part of two spectra from measurements at different CEPs are shown in figure 8.3. A modulation is visible in figure 8.3(a) for energies greater than 100 eV, whereas in (b) there is a continuum instead. By looking at all spectra for all different CEPs between -6.2 and +6.4 rad the continuum can be observed at CEPs that have a separation of an integer multiple of π. As mentioned in chapter 3.4.3 a continuum in the high-energy range of a spectrum indicates an isolated attosecond pulse composed of the photon energies available in the continuum. By spectrally selecting this photon-energy range with a filter, it would then be possible to produce a single attosecond pulse.

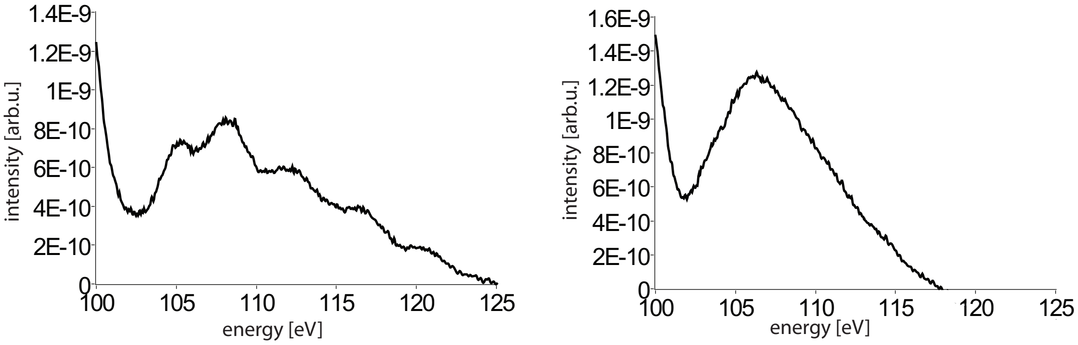

Figure 8.3: Two harmonic spectra measured at 70 mbar of neon in the gas cell and at 6 mm in front of the focus and (a) at a CEP -5.8 rad, at which an interference pattern is visible at the high photon energies and (b) at a CEP of -5.2 rad, at which a continuum appears.

8.3 HCOs

8.3.1 Analysis Method

As introduced before in section 6 the measured data have, on one hand, a low-intensity region around the silicon absorption line and, on the other hand, at higher energies the high-harmonic radiation generally exhibits its cutoff and, thus, lower the intensity. In these spectral regions, structures in the harmonic radiation are hard to observe due to the low intensity. Therefore, the measured two-dimensional position resolved spectra (dispersion and spectrometer-slit directions) have to be normalised in abscissa and ordinate direction. This is done by calculating the mean value of the intensity of every individual spectrum and of every photon-energy for all measured CEPs and divide the intensities at specific CEP and photon-energy by the corresponding mean value.

As mentioned earlier, the half-cycle cutoffs are better observable, if the energy modulation of the high-harmonic spectrum is filtered out. Therefore, a low-pass filter is implemented, which is based on a Fourier transform along the energy axis. At a chosen filter frequency all higher frequency modulations are cut out. This cut-frequency is selected such that the modulation of the high-harmonic radiation just disappears in the spectra transformed back.

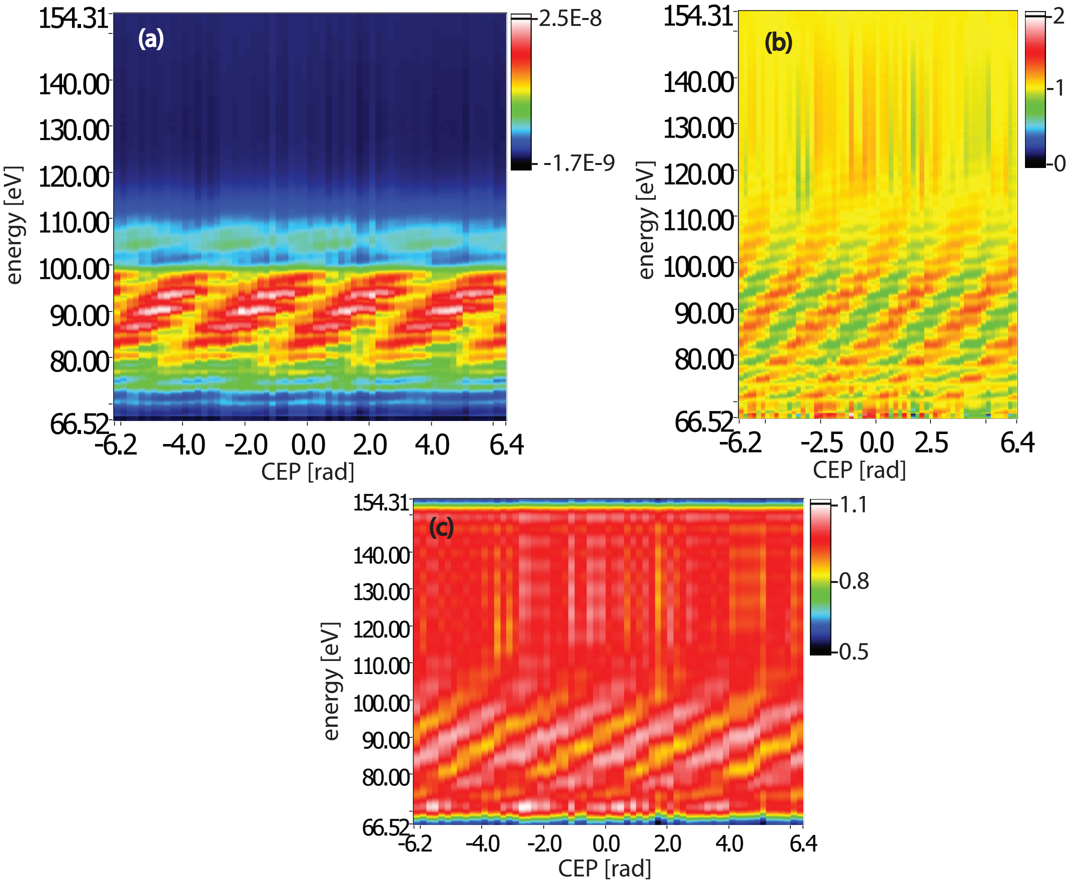

Figure 8.4: Three steps of the analysis process: plot (a) shows the raw data, in which the silicium edge (around 100 eV) is clearly visible; in (b) the data is normalised in horizontal and vertical direction and (c) shows the data after the low-pass filter, in which the harmonic modulation is filtered out.

The CEP-dependent measurements were in general done over a phase difference of $\approx 4\pi$. This implies that the carrier wave crossed the envelope two times, hence in the plots showing the data four half-cycle cutoffs are visible in one measurement. To analyse these half-cycle cutoffs with better statistical significance, the spectra are cut into four equal parts of a width of around 1π and Fourier transformed again but in the perpendicular direction, along the CEP-axis. Then, the imaginary part of the Fourier transform is read out in polar coordinates, that provides the phase. This phase is a measure for the position (along the CEP axis) of the maximum harmonic emission at each photon energy. Unwrapping this phase as a function of photon energy gives the evolution of the half-cycle cutoff maxima as a function of photon energy. The extracted phase is in fact not equal but related to the relative CEP by a factor of roughly -1/2 (as 2π rad of phase shift in each of the 4 segments corresponds to only π rad of CEP). As each segment was chosen slightly shorter than π rad in CEP (3.0 rad), the correct factor was -1/2.093. From this data one can assign a CEP value to each HCO at a given photon energy. The half-cycle cutoff energy can be converted into the instantaneous driving laser pulse field strength using equation 3.59:

$$E_{HCM} = \sqrt{\frac{4m_e\omega_f^2(E_{CO} - I_p)}{3.17e^2}}, \tag{8.1}$$

where E_{CO} is the measured energy of the HCO, $I_p = 21.5645$ eV is the ionisation potential of neon, e is the charge and m_e the mass of an electron, ω_f is the frequency of the fundamental laser pulse and E_{HCM} is its instantaneous field strength. The CEP axis can be converted into a time axis:

$$\Delta t = \frac{t_c}{2\pi}\Delta\phi_{CEP}, \tag{8.2}$$

where $t_c \approx 2.5$ fs is the optical cycle period at the central wavelength 750 nm of the driving laser pulse and $\Delta\phi_{CEP}$ is the change of the CE-phase. In summary, it is possible to extract from a CEP measurement, in which half-cycle cutoffs are visible, a section of the driving laser pulse intensity envelope. The data that will be shown in the following are given in terms of field strength and in atomic units.

8.3.2 HCO Analysis

To model the driving laser pulses extracted from the HCO analysis, a program was written to fit a Gaussian pulse to the measured values. As fit parameter the full width at half maximum (FWHM), the peak field strength of the pulse and the absolute position in time of the measured data were used. To evaluate the fit, a quality parameter was defined

$$\chi^2 = \frac{\sum_i (X_{meas,i} - X_{fit,i})^2}{\overline{|\Delta X|}}, \tag{8.3}$$

where $X_{meas,i}$ is the i-th measured value, and $X_{fit,i}$ the corresponding value on the Gaussian pulse, and $\overline{|\Delta X|}$ is the mean value of the absolute value of all differences between measurement and fit. To find the best fit, the program varied the FWHM from 4 to 15 fs in steps of 1 fs and the peak intensity of the pulse between 0.1 a.u. ($\hat{=}3.51 \cdot 10^{14}$ W/cm^2) and 0.2 a.u. ($\hat{=}1.40 \cdot 10^{15}$ W/cm^2). For every FWHM the best fit was obtained.

Estimation of the FWHM

Two fits for two different FWHM are shown in figure 8.5 for measured data at 100 mbar neon in the gas cell, with the cell placed 6 mm in front of the focus. The analysis of the data opens the possibility to estimate a minimal FWHM that the pulses had in the experiment. At lower FWHM of the Gaussian pulse the data clearly deviates from the pulse. An upper limit for the FWHM for the presented data cannot be found within the considered interval of 4 to 15 fs FWHM.

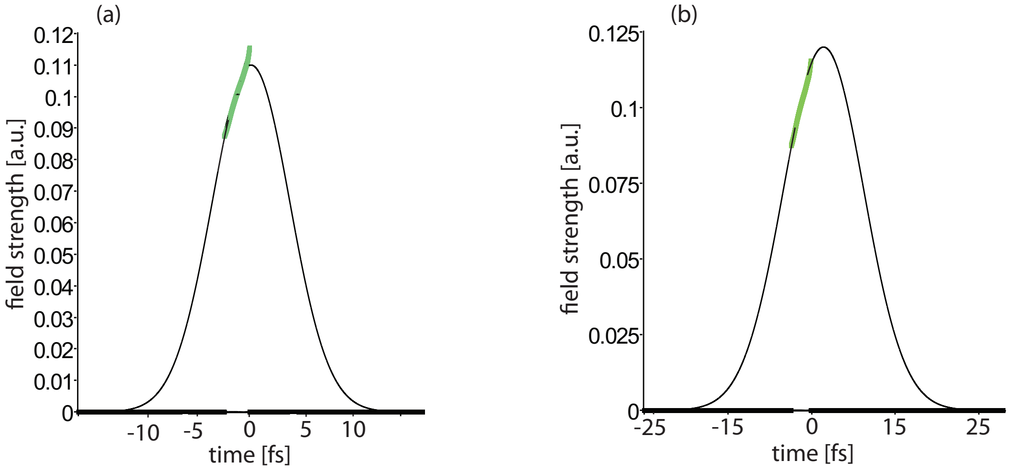

Figure 8.5: Driving laser field strength distribution as function of the pulse time. Measured data (green line) at 100 mbar neon and generated 6 mm in front of the focus plotted with the best fitted Gaussian pulse (black line) for (a) at 6 fs FWHM, in which the field strength profile does not fit the measured values in the whole range and (b) at 8 fs, in which the agreement with the data is optimal.

8.3.3 Pressure Dependence

Mean Field Strength

In this paragraph the CEP dependence of the HCOs shall be analysed for different pressures. Therefore, CEP-scans over 12.6 rad in steps of 0.2 rad at a fixed cell position were performed for different pressures. The measured data are analysed as described in section 8.3.1 to extract the CEP dependence of the HCOs. Afterwards, the mean value of the field strength profile at the leading edge of the laser pulse is calculated, in figure 8.6

plotted as a function of the pressure in the gas cell. Three different measurements are shown, in which two measurements were carried out at a known cell position and the third was performed before the position (vernier) scale was installed in the experiment.

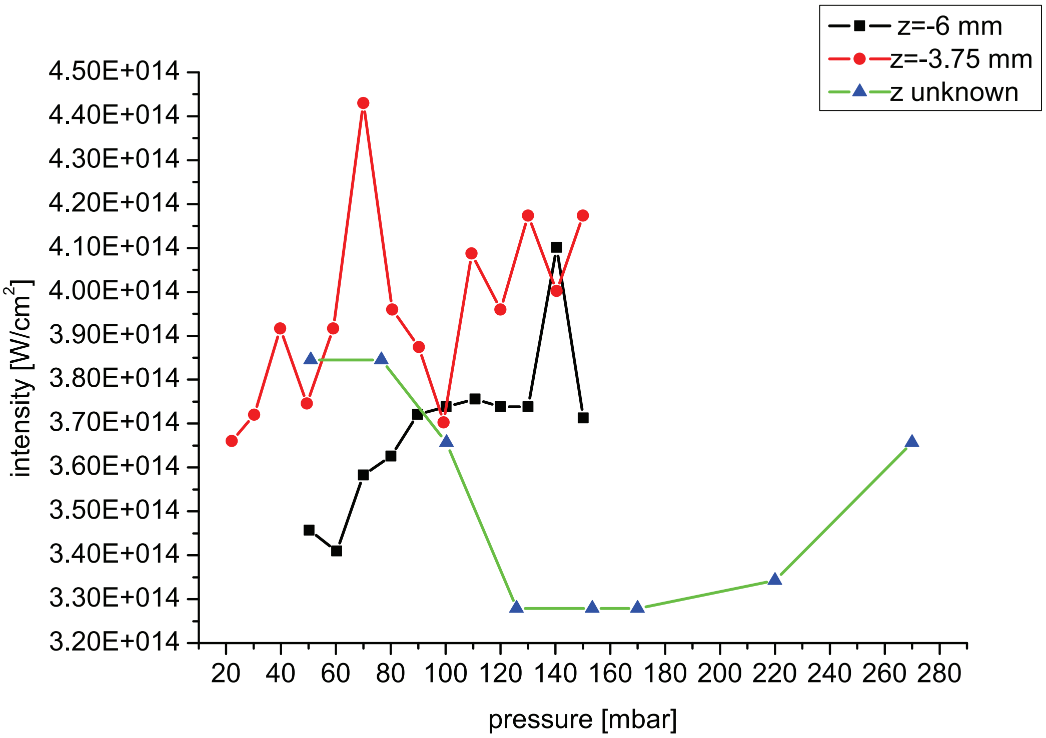

Figure 8.6: The mean field strength as a function of the pressure of the generation gas for three measurements.

Comparing the three measurements, it can be noticed that in the measurements with known position, which are within the Rayleigh length of the undisturbed focus (see section 7.2.1), the trend of increasing field strength with increasing pressure is visible. In contrast to this, the third measurement shows a clear decreasing and then an increase at high pressures.

An explanation of this behaviour could be that in the first two measurements self-focussing is preferred and with rising pressure the strength of the self-focussing is growing and the laser pulses becomes more intense. The black curve shows a saturation for pressures greater than 90 mbar apart from an outlier at 140 mbar.

Partly large fluctuations between neighbouring data points are probably due to variations in the mean field strength of the driving laser pulse. Those are difficult to estimate within the scope of this work, very much at the beginning of the project, only one CEP-dependent measurement could be performed for one pressure.

Slope

Now, the temporal slope of the field strength profile at the leading edge of the laser pulses shall be studied and. Nearly all measured data are lying on a section of the fitted Gaussian pulse that can be estimated as linear, as it is shown in figure 8.5. To analyse the pressure dependency of the slope of the laser pulses, the measured values are fitted with a linear function. The resulting slopes are shown in figure 8.7 as function of the pressure using the same measurements as in the paragraph before.

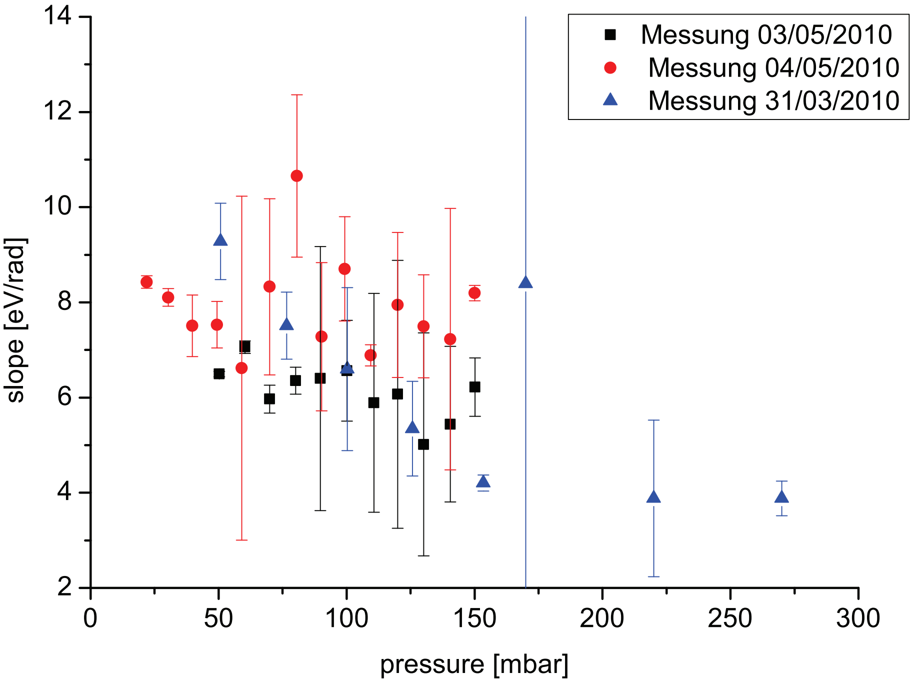

Figure 8.7: Temporal slopes of the field strength profile of the laser pulses as a function of the pressure of the generation gas of three pressure scans.

The slopes are varying between 3.9 and 10.7 eV per rad and are nearly constant within the error bars only a slight trend is visible, which is that the slope is decreasing with increasing pressure. This could be explained by a pulse-shape modification of the driving laser pulse as it hits the generation gas and propagates through it. The effect is small due to the short interaction length of less than 3 mm (compared to interaction lengths on the order of 1 meter typically used for SPM). With increasing pressure, the refractive index of the generation medium is growing and the strength of the effect is rising.

The errors shown in figure 8.7 are estimated via the linear fit. Some of the error bars are huge. The largest error bar (within the blue set of data points) is due to the fact that in the measurement for this value no actual HCOs were visible. The other errors can be explained by artefacts in the phase that is used to calculate the HCO positions. In some measurements some irregularities in the CEP-dependent high-harmonic spectra (from which the HCO is retrieved) are visible, which could be caused by drifts in the CEP if the CEP-stabilisation was not working properly or the CEP changes between the point, where the stabilisation setup is placed and the HHG generation region. In the experimental configuration used here, the CEP detection for stabilisation was located before the beam propagated through the SPM hollow fibre, in which CEP drifts might occur by changing coupling conditions and even by instability of the laser pulse energy. To have a better control over the CEP it is planned to operate a second CEP detection and control unit after the SPM hollow fibre, near to coupling into the vacuum system.

8.3.4 Position Dependence

Mean Field Strength

After analysing the pressure dependence of the field strengths corresponding to the HCO evolution with CEP, the position dependence is studied in more detail. The analysis method used is equal to the one used above. The CEP measurements are done for a fixed pressure and different cell positions. Three position scans are presented in figure 8.8. The black and blue data points were taken at 100 mbar of neon and the red values are measured at 60 mbar neon pressure in the cell.

In this plot no consistent trend can be found. While the field strength at 60 mbar is slightly increasing, the blue data are showing a strong increase and the black values a decrease of the field strength with an increasing position of the cell. What is expected is an increase of the calculated mean field strength with increase peak field strength of the driving laser pulses, that should be the case if the cell is moved towards the focus. It is not possible to find similarities between the two 100 mbar measurements. For the measurement corresponding to the blue data points in figure 8.8 the averaged power laser was temporarily exceptionally high up to 1.47 W. The mean value of the field strength profile corresponding to the CEP-dependent HCO evolution of both measurements in this figure seem to be correlated with the averaged power (see figure 8.9) and less with the chosen z position.

Besides the change of the focal position that will be discussed in the last section of this part, other reasons for the difficulties in the position scans are geometrical problems. The translation stage used to control the z position might not be exactly aligned angularly to the incoming laser beam. In this case, moving the stage might also result in an effective

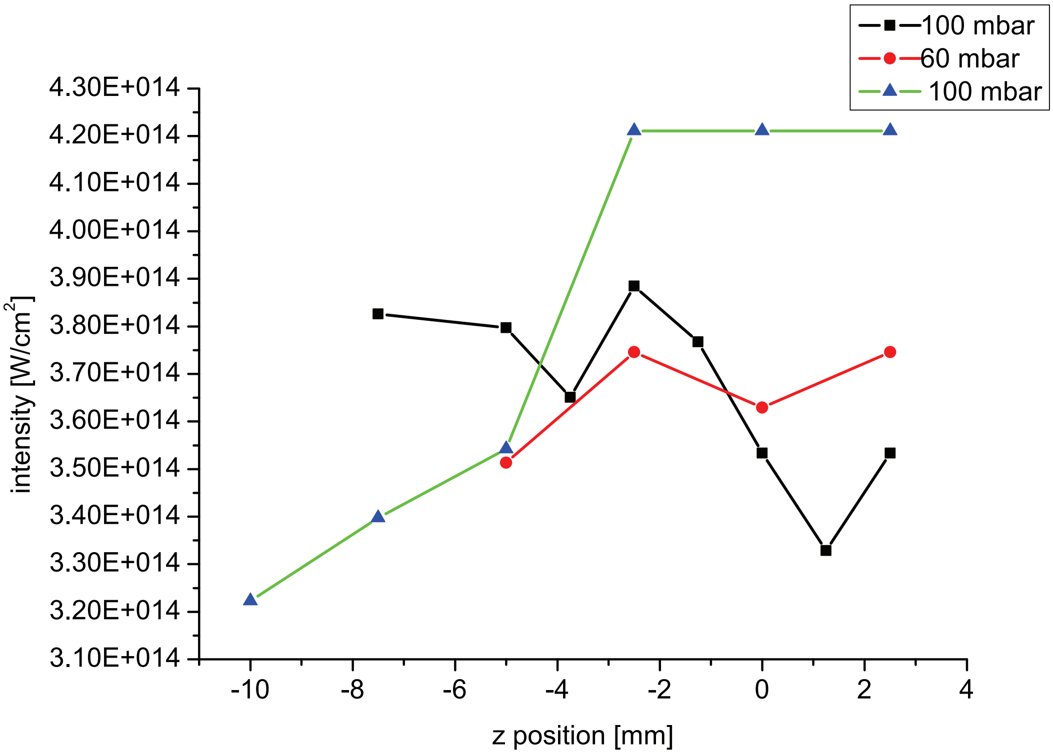

Figure 8.8: The mean value of the field strength profile at the leading edge of the laser pulse as a function of the position of the gas cell for three measurements.

lateral movement of the cell with respect to the focus when moving along the z direction.

Slope

For the position scans it is also possible to extract the slope of the HCO vs. CEP evolutions. Again, the analysis is carried out by using the same methods as described in section 8.3.3. Figure 8.10 shows the results for the measurements. This time the slope is increased by moving towards and beyond the focus. The rising of the slope can be a hint for an increasing intensity, which would be expected when moving the cell towards the focus. However, this measurement should be interpreted carefully because of the strong effects on the focal position already discussed.

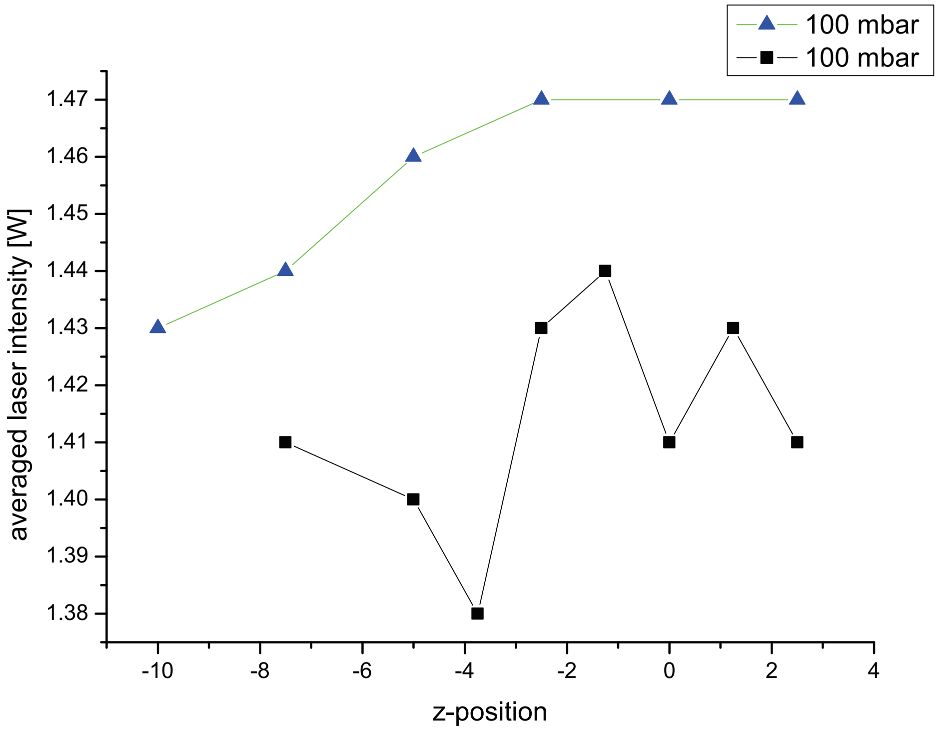

Figure 8.9: Evolution of the averaged power of the laser of the measurements presented in figure 8.8. The colours used corresponds to the colours in the measurements shown in figure 8.8.

8.3.5 Comparison with the Simulation

Finally, it is interesting to compare the measured evolution of the HCOs with the simulation of the ionisation gating presented in part III. The fitting routine shown above provides a Gaussian pulse that can be used for the simulation with its FWHM and the corresponding field strength. Some examples are shown in figure 8.11. The simulated gate is in good agreement with the temporal position and duration of the experimentally observed HCO evolution. In every case, the ionisation gate is closing within a small and fixed field strength range (near 0.12 a.u.). It can be seen that the gate timing and temporal evolution is largely independent on the choice of FWHM for the laser pulse (see figure 8.11).

Pressure Scan

For a more detailed comparison of the simulation and the experimental data, an entire pressure scan is analysed and the results are discussed in the following. The measurement

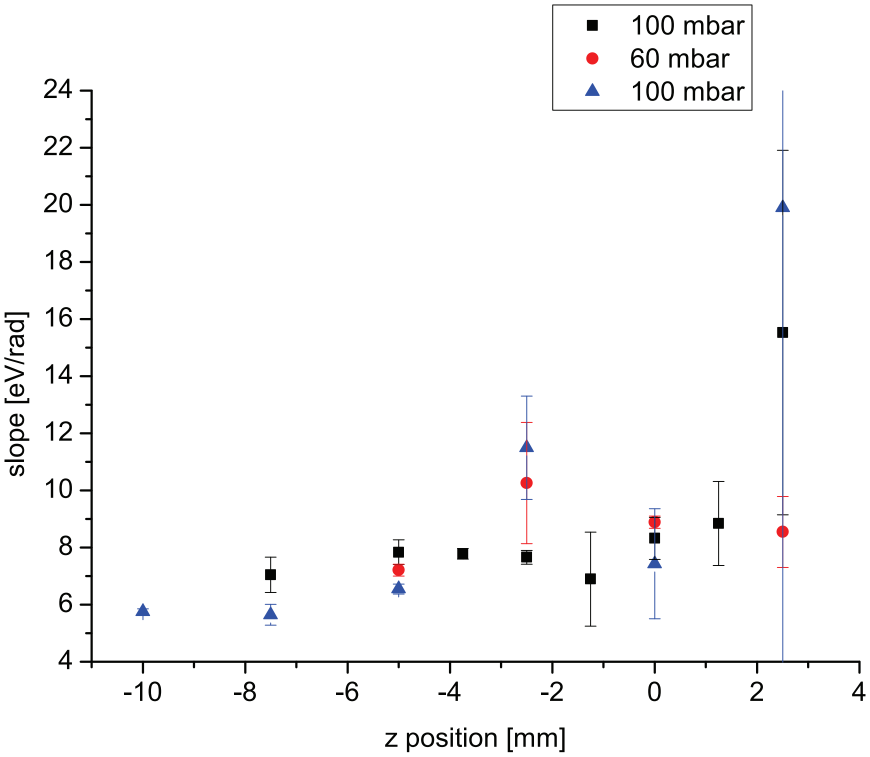

Figure 8.10: Slopes of the HCO vs. CEP evolutions as a function of the position of the gas cell for three position scans.

of the harmonic yield as a function of the pressure is shown in figure 8.12. A peak function is fitted to the data. For the Gaussian fit of the driving laser pulse a duration is chosen, at which all measured values for the different pressures can be fitted using this pulse (cp. section 8.3.2). The peak field strength was estimated by calculating the mean value of the peak field strength for 10 fs FWHM given by the fitting routine at the eight measured pressures. The estimated value for the field strength is 0.128 ± 0.015 a.u. (corresponding to to an laser intensity of $5.75\text{x}10^{14} \pm 0.08\text{x}10^{14}$ W/cm^2).

To adjust the phase-matching factor there are two different approaches. The first way is to estimate an optimal phase-matching gate for all pressures by using the position as a free parameter and the measured pressures and the (as presented in section 8.3.2) estimated field strengths as fixed parameters. The resulting phase-matching factors, measured data and fitted Gaussian pulses are shown in figure 8.14. The pressure is set as measured and the cell position is varied to achieve the best fit. All measured extractions of the leading-edge of the driving laser pulse are in good agreement with the simulated phase-matching gate. The position of the cell has to be adapted for every pressure to obtain the optimal

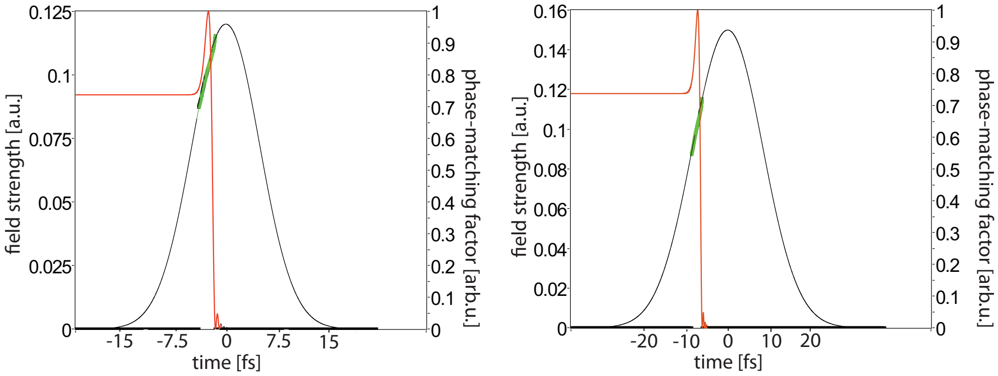

Figure 8.11: Measured values (green) at 100 mbar of neon in the gas cell generated 6 mm in front of the focus fitted to a Gaussian driver pulse with (a) 8 fs FWHM and 0.12 a.u. peak field strength and (b) 13 fs FWHM and 0.15 a.u. peak field strength; the red curve is the phase-matching factor (see section **??**) calculated for the fitted Gaussian pulses and for the generation placed 7.8 mm in front of or after the focus.

phase-matching gate. Similar to the bell-shaped plot in figure 4.7, the closer the cell is placed to the focal position the higher the pressure for optimal phase matching. In the presented case, the variation of the harmonic yield during the measurement is due to the different pressures. The primarily rising yield with increasing pressure (figure 8.12) is thus caused by the increasing number of atoms in the generation region. The decrease at higher pressures is due to growing absorption, a defocussing of the laser beam or other effects on the position of the beam at an increased density of the generation gas.

The second approach is to estimate an optimal gating behaviour only at the maximum of the harmonic yield. The evolution of the yield is then considered to be caused by changes in the phase-matching conditions. The pressure at the maximum in the harmonic yield is approximated with an exponential peak function in figure 8.12. The peak is located at 122.65 mbar. For this, a cell position of 6.8 mm in front of the focus is estimated by visual judgement in the simulation to result in the best phase-matching factor. The results are shown in figure 8.15, and the evolution of the phase-matching factor is similar to figure 8.13(a), at where the phase-matching factor is simulated for the estimated cell position and for different pressures. Between 50 and 150 mbar the extracted gate position is in good agreement with the measured data. For the higher pressures, the opening and the closing of the gate is located at too late times. The HCOs are not (or only barely) visible in the measurement at 170 mbar and at higher pressures, the HCOs appeared again. A small side peak could explain that, which arises in front of the main gate and which lies exactly at the times, for which measured HCO evolutions exist (see the dashed ring in figure 8.15(f)-(h)). The HCOs are not (or only barely) visible in the measurement at 170 mbar and at higher pressures, the HCOs appeared again. One could conclude that the

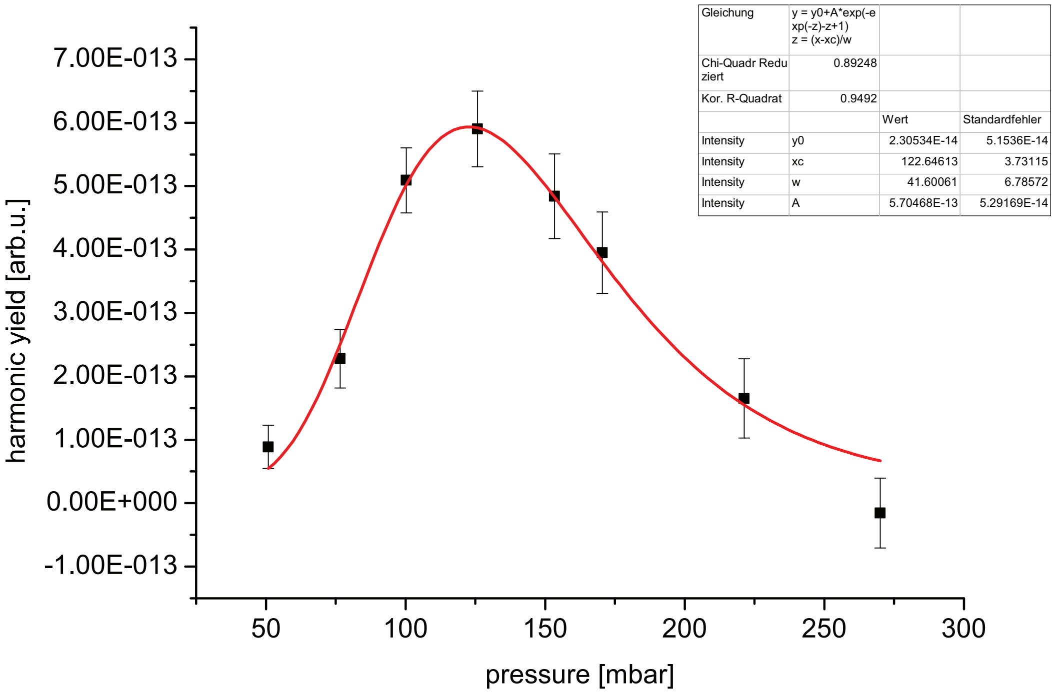

Gleichung	y = y0+A*exp(-exp(-z)-z+1) z = (x-xc)/w		
Chi-Quadr Reduziert	0.89248		
Kor. R-Quadrat	0.9492		
		Wert	Standardfehler
Intensity	y0	2.30534E-14	5.1536E-14
Intensity	xc	122.64613	3.73115
Intensity	w	41.60061	6.78572
Intensity	A	5.70468E-13	5.29169E-14

Figure 8.12: Harmonic yield of a CEP- and pressure scan at unknown cell position and a fit.

time the main peak “opens the gate” is too short to see it in the measured values, but one has to be careful not to overinterpret the data, as approximations such as 1-dimensional beam propagation are used.

Finally, we will compare the harmonic yield expected by the simulation with the measured harmonic yield (figure 8.12). To calculate the harmonic yield in the measurement, the spectra are integrated over all photon energies measured (61 eV to 125 eV). These photon energies are converted into a field strength (0.077 a.u. to 0.125 a.u. corresponding to 2.08x10^{14} W/cm^2 to 5.96x10^{14} W/cm^2) as described in 8.3.1 for HCOs. The phase-matching factor is then integrated over all times, in which the leading-edge of the Gaussian pulse fitted lies in this field strength range. In addition, the phase-matching factor have be multiplied with a weighting factor that is p^2 the squared pressure. The results for the experimental settings are shown in figure 8.13 (b). The qualitative shape of the theoretical curve is very similar to the measurement.

To have the experimental and theoretical yield in one plot, the graphs figure 8.13(b) and 8.12 are normalised to 1 at the maximum. The cell position in the simulation is corrected

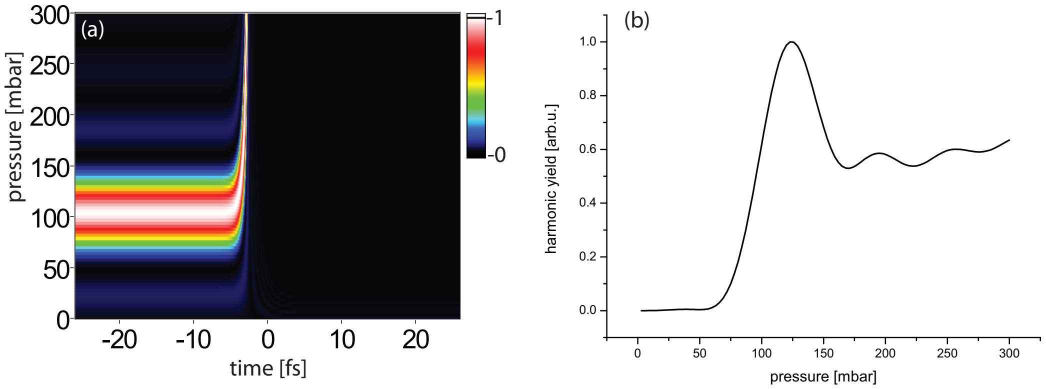

Figure 8.13: (a) Phase-matching factor simulated for different pressures at 6.8 mm in front of the focus and a laser pulse with 10 fs duration and 0.128 peak field strength. (b) Simulated harmonic yield for the same pulse.

to 6.4 mm, because the peak of the measurement and the simulated gate did not overlap with the first z position of 6.8 mm estimated by visual judgement. The result is shown in figure 8.16. The experimentally specified yield is overall higher than the simulated one, however in the high-pressure range the simulated yield decreases initially fast and then it rises again slightly above 160 mbar while the experimental results show an almost linear decrease of the yield. The increase at higher pressure in the simulation is not real and it is caused by neglecting effects such as pressure-dependent defocussing of the fundamental laser beam.

The harmonic yield of a second measurement (figure 7.3(c)) is shown in figure 8.17 along with a simulated yield. In the measurement, the cell was placed 3.75 mm in front of the vacuum focal position. For the simulation, a z position of 6.4 mm is chosen to make the maxima of both curves overlap. The simulation is in very good agreement with the measured data.

In summary, both ways to compare the experiment to the simulation lead to meaningful results. The actual behaviour of the phase matching will most likely be somewhat different, although a moving focus and different phase-matching evolutions as a function of time can be considered to play an important role. Certainly we cannot assume HHG to be always optimally phase-matched nor the focal position to be fixed. The simulation does not include beam-propagation effects such as ionisation-induced defocusing within the gas cell, leading to a change in focal size and z position, and self-phase modulation. The actual focal position cannot be exactly determined. In addition, the disturbed focussing could affect on the Gouy-phase shift and, thus, immediately affect phase matching as well, since the Gouy-phase shift is one of the three main terms that contribute to phase matching. Therefore, the simulation does not perfectly reflect the experiment but nevertheless the comparison shown above provides some deeper insight into the mechanisms of phase matching on ultrashort time scales.

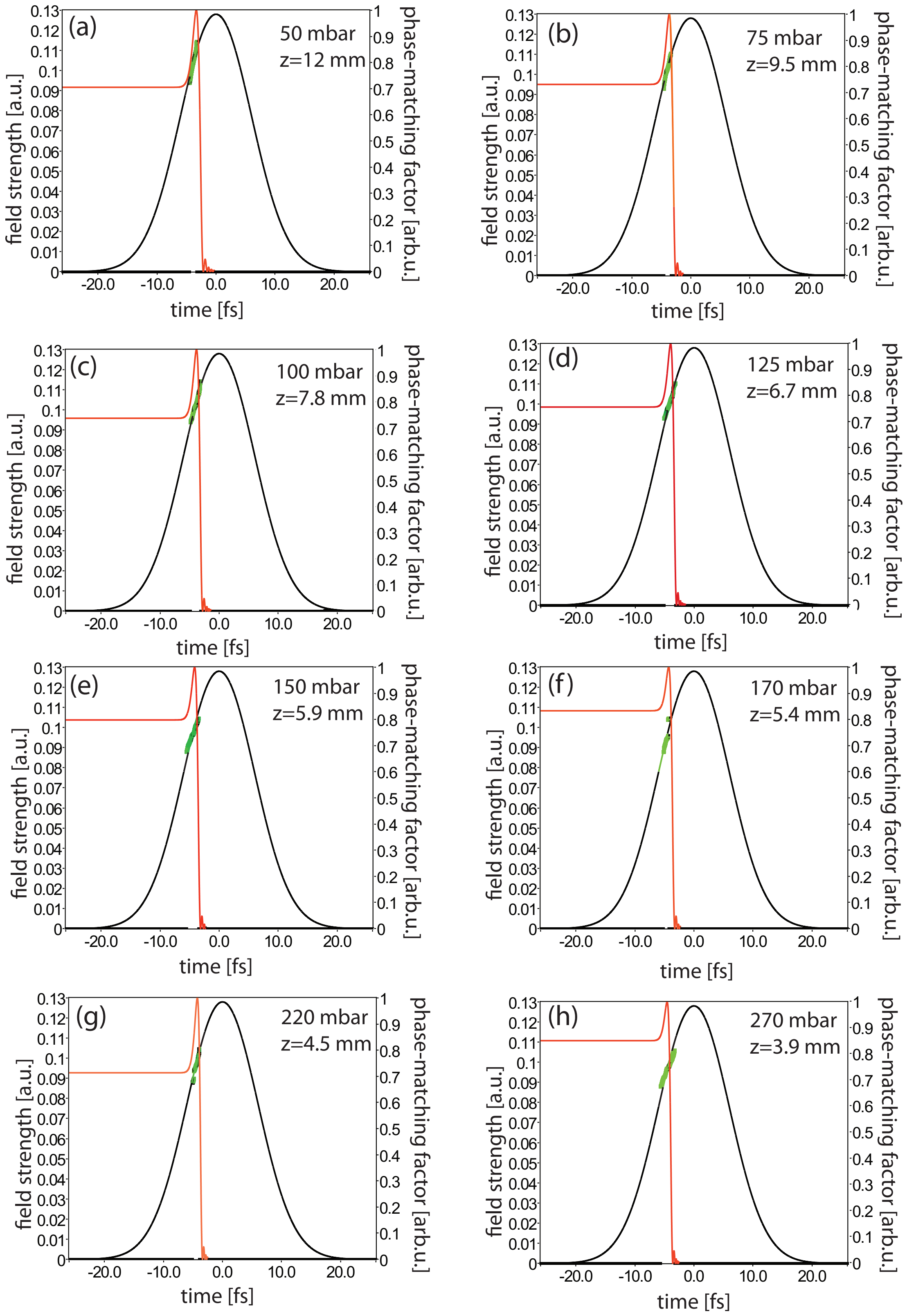

Figure 8.14: Comparison between measured data of figure 8.12 and the simulation. The pulse duration of the Gaussian pulse shown is 10 fs and its peak field strength is 0.128 ± 0.015 a.u.. The settings for pressure and z position are (a) 50 mbar and 12 mm (b) 75 mbar and 9.5 mm (c) 100 mbar and 7.8 mm (d) 125 mbar and 6.7 mm (e) 150 mbar and 5.9 mm (f) 170 mbar and 5.4 mm (g) 220 mbar and 4.5 mm and (h) 270 mbar and 3.9 mm.

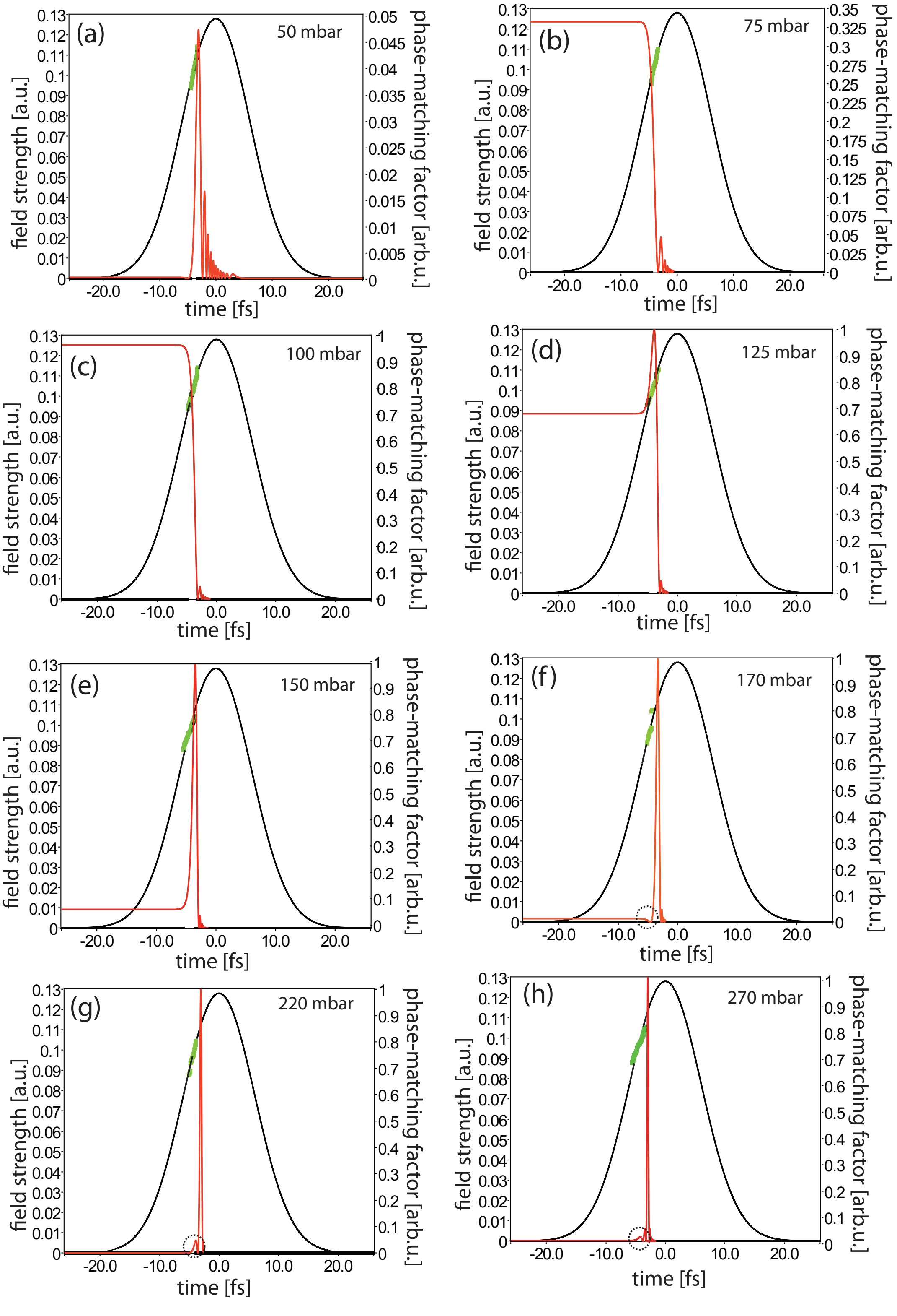

Figure 8.15: Comparison between measured data of figure 8.12 and the simulation. The pulse duration of the Gaussian pulse shown is 10 fs and its peak field strength is 0.128 a.u.. The z position is fixed at 6.8 mm and the pressures are (a) 50 mbar (b) 75 mbar (c) 100 mbar (d) 125 mbar (e) 150 mbar (f) 170 mbar (g) 220 mbar and (h) 270 mbar.

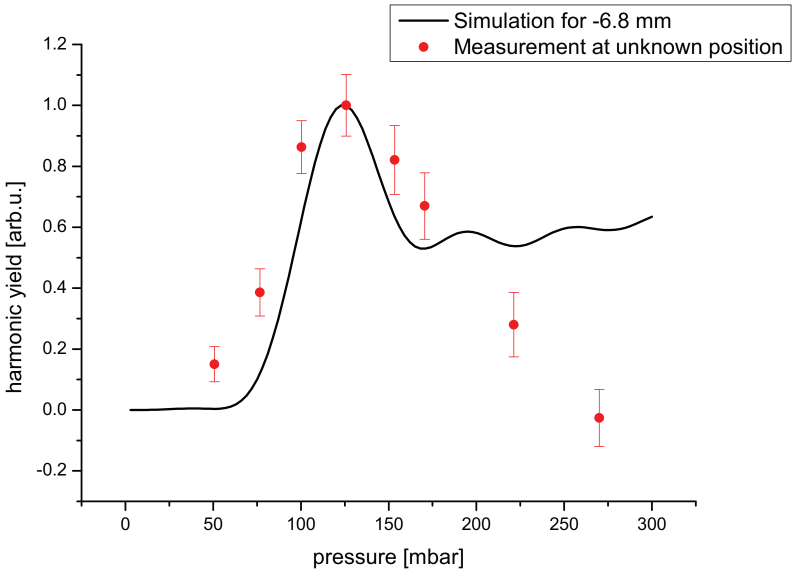

Figure 8.16: Normalised experimental and simulated harmonic yield.

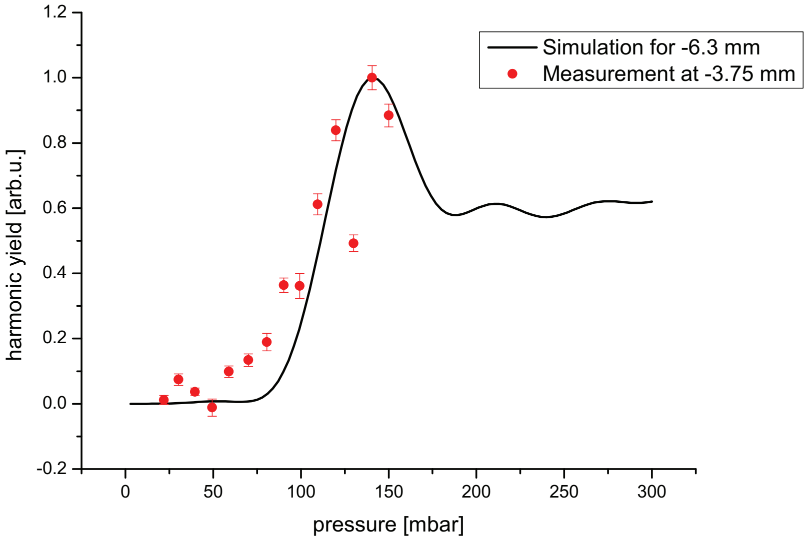

Figure 8.17: Normalised experimental and simulated harmonic yield for the measurment shown in figure 7.3(c).

Part VI

Summary & Outlook

9 Summary & Outlook

In this work the design of a new attosecond spectrometer is presented. This setup is using a commercially available titanium:sapphire laser system that provides CEP-stabilised ultrashort high-intense laser pulses (4-10 fs pulse duration and intensities around 10^{14} W/cm^2) for high-harmonic generation (HHG) to achieve even shorter pulses with durations of a few hundred attoseconds or below. The intention of this new setup is to perform pump-probe experiments with the driving laser pulses and the generated high-harmonic radiation. During the design and the build up of a first step of the originally planned setup, a simulation on phase matching in HHG was implemented. This simulation was used to analyse the properties of the phase-matching process with particular attention on its special role as a gating mechanism in HHG, called ionisation gating. The simulation is used to study the behaviour of this gating for different experimental conditions such as the peak intensity of the driving laser pulse, the pressure of the gaseous generation medium or the position of the gas cell, where HHG occurs.

A preliminary experimental beam line setup was then used to produce and characterise high-harmonic radiation with the newly designed parts. The experiments were carried out with particular focus on the CEP-dependence of the high harmonics. At the right settings for phase matching, for the case that an ionisation gate exists, local maxima can be detected in the measured high-harmonic spectra, which are moving when the CEP is varied. They, called half-cycle cutoffs (HCO), reflect return energies of recolliding electrons within a single half-cycle of the laser field. Following the HCOs for different CEPs, one is able to extract the HHG light-emitting portion of the rising edge of the fundamental pulse to an energy that is defined by the closure of the ionisation gate. While several groups propose the development of the HCOs as possibility to measure the absolute value of the CEP [11, 55], we used these measurements to estimate the FWHM of the driving laser pulses by fitting a Gaussian pulse to the measured data. It was also shown that the simulated ionisation gate is in good agreement with the measured HCO evolution. Furthermore, the yield of the harmonic generation was analysed for different pressures of the generation gas neon and for different positions of the gas cell with respect to the laser focus. Moreover, the high-harmonic beam profile was inspected in the vertical direction depending on whether the generation was placed far away in front of the focal position or near to it and as function of the CEP. Finally, it is shown that it may be possible to generate even isolated attosecond pulses. In general, in every half-cycle of the driving laser pulse a XUV radiation burst is emitted, which results in a train of attosecond pulses. With the ionisation gate, HHG is suppressed after a few cycles on the leading edge. At a certain CEP, a continuum is visible in the spectra instead of the typical high-harmonic spectral modulation separated by two times the fundamental frequency that is due to interference. This continuum represents an energy range, in which only one attosecond burst is dominant and, therefore, no interference is visible. It is possible to extract an isolated attosecond pulse by filtering out the energies of the harmonic radiation, where the continuum does not appear.

The characterised radiation can be used in the final version of the presented experimental setup. In addition to the here-described high-harmonic generation and detection capability a split mirror will be placed into this upgraded system. This mirror will be used to introduce a time-delay between the driving laser pulse and the high-harmonic radiation. Both pulses are focussed with a toroidal mirror into a second gas cell, into which a target gas, such as nitrogen or argon or simple molecules such as hydrogen molecules, can be introduced and time-resolved spectroscopy via pump-probe experiments can be carried out. Examples of such experiments are described in [67].

A future step for this experiment is the insertion of a reaction microscope to obtain additional information about electronic processes in the target molecules besides the resulting spectrum of the harmonic radiation, already measurable in the current setup. These molecules will be located in the centre of the reaction microscope. The pump-pulse excites the molecules and after a time delay the probe-pulse dissociates them. The ions and electrons produced are accelerated via an electric and guided by a magnetic field towards highly precise spatially- and temporally resolving detectors. It is possible to measure the whole momentum space for particles particles at once and measure the electrons and ions produced in coincidence allowing to obtain correlated momentum maps of the emitted electrons.

In addition to the possibility to do time-resolved spectroscopy of quantum dynamics a pulse shaper will be installed into the setup to analyse how the shape of the driving laser pulse affects the behaviour of the molecule and, in particular, the dynamics and breaking of molecular bonds with the final goal of quantum control of electrons. This would then allow to steer chemical reactions to proceed in a certain direction and to suppress undesired reaction products. The first setup of the pulse shaper is a rather simple assembly, consisting of a prism to spectrally disperse the fundamental laser pulse onto a split mirror. By translating one part of this mirror one is able to introduce a phase step at one spectral position (that could be varied). The beam passes the prism again to undo the spectral separation and the thus shaped laser pulse is then used to generate high-harmonic radiation. In first simulations with this pulse shaper, we predict isolated attosecond pulses as well as attosecond double pulses in cases in which both pulses have the same intensity and a variable relative phase. To expand this idea, it is being considered to replace the split mirror by a liquid-crystal pixelated mask to get the opportunity to introduce more complex spectral phase profiles.

Bibliography

[1] TH Maiman. Stimulated optical radiation in ruby. *Nature*, 1960.

[2] A. Scrinzi, M.Y. Ivanov, R. Kienberger, and DM Villeneuve. Attosecond physics. *Journal of Physics B: Atomic, Molecular and Optical Physics*, 39:R1, 2006.

[3] P.A. Franken, AE Hill, CW Peters, and G. Weinreich. Generation of optical harmonics. *Phys. Rev. Lett.*, 7(4):118–119, 1961.

[4] M. Ferray, A. L Huillier, XF Li, LA Lompre, G. Mainfray, and C. Manus. Multiple-harmonic conversion of 1064 nm radiation in rare gases. *Journal of Physics B: Atomic, Molecular and Optical Physics*, 21:L31, 1988.

[5] A. McPherson, G. Gibson, H. Jara, U. Johann, TS Luk, IA McIntyre, K. Boyer, and CK Rhodes. Studies of multiphoton production of vacuum-ultraviolet radiation in the rare gases. *Journal of the Optical Society of America B*, 4(4):595–601, 1987.

[6] RL Carman, DW Forslund, and JM Kindel. Visible harmonic emission as a way of measuring profile steepening. *Phys. Rev. Lett.*, 46(1):29–32, 1981.

[7] PF Moulton. Spectroscopic and laser characteristics of Ti: Al_2O_3. *Journal of the Optical Society of America B*, 3(1):125–133, 1986.

[8] HR Telle, G Steinmeyer, AE Dunlop, J Stenger, DH Sutter, and U Keller. Carrier-envelope offset phase control: A novel concept for absolute optical frequency measurement and ultrashort pulse generation. *Appl. Phys. B: Lasers and Optics*, 69:327–332, 1999.

[9] G. G. Paulus, F. Lindner, H. Walther, A. Baltuška, E. Goulielmakis, M. Lezius, and F. Krausz. Measurement of the phase of few-cycle laser pulses. *Phys. Rev. Lett.*, 91 (25):253004, Dec 2003. doi: 10.1103/PhysRevLett.91.253004.

[10] G.G. Paulus, F. Lindner, H. Walther, A. Baltuška, and F. Krausz. Measurement of the phase of few-cycle laser pulses. *Journal of Modern Optics*, 52(2):221–232, 2005.

[11] CA Haworth, LE Chipperfield, JS Robinson, PL Knight, JP Marangos, and JWG Tisch. Half-cycle cutoffs in harmonic spectra and robust carrier-envelope phase retrieval. *Nature*, 3(1):52–57, 2006.

[12] T. Pfeifer, A. Jullien, M.J. Abel, P.M. Nagel, L. Gallmann, D.M. Neumark, and S.R. Leone. Generating coherent broadband continuum soft-x-ray radiation by attosecond ionization gating. *Nature*, 446:627–632, 2007.

[13] H. Heynau A.J. DeMaria, D.A. Stetser. Mode locking of a nd3+-doped glass laser. *Appl. Phys. Lett.*, 9:174, 1966.

[14] R.J. Collins H.W. Mocker. Mode competition and self-locking effects in a q-switched ruby laser. *Appl. Phys. Lett.*, 7:270, 1965.

[15] K. Jesse. *Femtosekundenlaser: Einfuehrung in die Technologie der ultrakurzen Lichtimpulse.* Springer, 2005.

[16] Markus Werner Sigrist Fritz Kurz Kneubuehl. *Laser.* B. G. Teubner Verlag, 2005.

[17] Georg Gademann. Komprimierung ultrakurzer lichtimpulse mit hilfe der filamentation und eines adaptiven impulskompressors. Master's thesis, Max-Planck Institut fuer Kernphysik Heidelberg, Universitaet Heidelberg, 2007.

[18] J.C. Diels, W. Rudolph, P. Gibbon, F.X. Kaertner, T. Iwazumi, K. Mase, S.H. Gold, G.S. Nusinovich, P.M. Smith, B.E. Carlsten, et al. *Ultrashort Laser Pulse Phenomena: Fundamentals, Techniques, and Applications on a Femotosecond Time Scale.* Inst. Phys., 1996.

[19] BEA Saleh and MC Teich. Fundamentals of photonics., 1991.

[20] FX Kartner. *Few-cycle laser pulse generation and its applications.* Springer Verlag, 2004.

[21] Alexander Sperl. Erzeugung und charakterisierung ultrakurzer lichtimpulse fuer die generation hoher harmonischer strahlung. Master's thesis, Max-Planck Institut fuer Kernphysik Heidelberg, Universitaet Heidelberg, 2009.

[22] D. Meschede. *Optik, Licht und Laser.* Vieweg+ Teubner Verlag, 2008.

[23] DE Spence, PN Kean, and W. Sibbett. 60-fsec pulse generation from a self-mode-locked Ti: sapphire laser. *Optics Letters*, 16(1):42–44, 1991.

[24] A.E. Siegman. Lasers. Mill Valley, 1986.

[25] RL Fork, OE Martinez, and JP Gordon. Negative dispersion using pairs of prisms. *Optics letters*, 9(5):150–152, 1984.

[26] J.P. Gordon and RL Fork. Optical resonator with negative dispersion. *Optics letters*, 9(5):153–155, 1984.

[27] V. Yakovlev and G. Tempea. Optimization of chirped mirrors. *Applied optics*, 41(30): 6514–6520, 2002.

[28] RR Alfano. The supercontinuum laser source, 1989.

[29] Franz X. Kaertner. Ultrafast optics. MIT - OpenCourseWare, 2005.

[30] Thomas Pfeifer. *Adaptive Control of Coherent Soft X-Rays*. PhD thesis, Julius-Maximilians-Universitaet Wuerzburg, 2004.

[31] M. Kakehata, H. Takada, Y. Kobayashi, K. Torizuka, Y. Fujihira, T. Homma, and H. Takahashi. Single-shot measurement of carrier-envelope phase changes by spectral interferometry. *Optics Letters*, 26(18):1436–1438, 2001.

[32] G. Farkas and C. Toth. Proposal for attosecond light pulse generation using laser induced multiple-harmonic conversion processes in rare gases. *Phys. Lett. A*, 168(5-6): 447–450, 1992.

[33] JJ Macklin, JD Kmetec, and CL Gordon III. High-order harmonic generation using intense femtosecond pulses. *Phys. Rev. Lett.*, 70(6):766–769, 1993.

[34] A. L Huillier and P. Balcou. High-order harmonic generation in rare gases with a 1-ps 1053-nm laser. *Phys. Rev. Lett.*, 70(6):774–777, 1993.

[35] J.L. Krause, K.J. Schafer, and K.C. Kulander. High-order harmonic generation from atoms and ions in the high intensity regime. *Phys. Rev. Lett.*, 68(24):3535–3538, 1992.

[36] PB Corkum. Plasma perspective on strong field multiphoton ionization. *Phys. Rev. Lett.*, 71(13):1994–1997, 1993.

[37] KC Kulander, KJ Schafer, and JL Krause. Super-intense laser-atom physics. *NATO Advanced Science Institutes Series*, 316:?, 1993.

[38] M. Lewenstein, P. Balcou, M.Y. Ivanov, A. L Huillier, and PB Corkum. Theory of high-harmonic generation by low-frequency laser fields. *Phys. Rev. A*, 49(3):2117–2132, 1994.

[39] LV Keldysh. Ionization in the field of a strong electromagnetic wave. *Sov. Phys. JETP*, 20(5):1307–1314, 1965.

[40] MV Ammosov, NB Delone, VP Krainov, et al. Tunnel ionization of complex atoms and of atomic ions in an alternating electromagnetic field. *Sov. Phys. JETP*, 64(6): 1191–1194, 1986.

[41] S. Augst, DD Meyerhofer, D. Strickland, and SL Chint. Laser ionization of noble gases by Coulomb-barrier suppression. *Journal of the Optical Society of America B*, 8 (4):858–867, 1991.

[42] G. P. ZHANG. High harmonic generation in atoms, molecules and nanostructures. *International Journal of Modern Physics B: Condensed Matter Physics; Statistical Physics; Applied Physics*, 21(31):5167 – 5185, 2007. ISSN 02179792. URL `http://search.ebscohost.com/login.aspx?direct=true&db=aph&AN=28021583&site=ehost-live`.

[43] M. Lewenstein, P. Salieres, and A. L huillier. Phase of the atomic polarization in high-order harmonic generation. *Phys. Rev. A*, 52(6):4747–4754, 1995.

[44] P. Salieres, B. Carre, L. Le Deroff, F. Grasbon, GG Paulus, H. Walther, R. Kopold, W. Becker, DB Milosevic, A. Sanpera, et al. Feynman's path-integral approach for intense-laser-atom interactions. *Science*, 292(5518):902, 2001.

[45] T. Auguste and P. Salières. Theoretical and experimental analysis of quantum path interferences in high-order harmonic generation. *Phys. Rev. A*, 80:033817, 2009.

[46] P. Balcou, A.S. Dederichs, M.B. Gaarde, and A. L Huillier. Quantum-path analysis and phase matching of high-order harmonic generation and high-order frequency mixing processes in strong laser fields. *Journal of Physics B: Atomic, Molecular and Optical Physics*, 32:2973, 1999.

[47] MB Gaarde, F. Salin, E. Constant, P. Balcou, KJ Schafer, KC Kulander, and A. L Huillier. Spatiotemporal separation of high harmonic radiation into two quantum path components. *Phys. Rev. A*, 59(2):1367–1373, 1999.

[48] P. Salieres, A. L Huillier, and M. Lewenstein. Coherence control of high-order harmonics. *Phys. Rev. Lett.*, 74(19):3776–3779, 1995.

[49] A. L Huillier, P. Balcou, S. Candel, K.J. Schafer, and K.C. Kulander. Calculations of high-order harmonic-generation processes in xenon at 1064 nm. *Phys. Rev. A*, 46(5): 2778–2790, 1992.

[50] M. B. Gaarde, Ph. Antoine, A. L Huillier, K. J. Schafer, and K. C. Kulander. Macroscopic studies of short-pulse high-order harmonic generation using the time-dependent schrödinger equation. *Phys. Rev. A*, 57(6):4553–4560, Jun 1998. doi: 10.1103/PhysRevA.57.4553.

[51] T. Pfeifer, C. Spielmann, and G. Gerber. Femtosecond x-ray science. *Reports on Progress in Physics*, 69:443, 2006.

[52] E. Constant, D. Garzella, P. Breger, E. Mevel, C. Dorrer, C. Le Blanc, F. Salin, and P. Agostini. Optimizing high harmonic generation in absorbing gases: model and experiment. *Phys. Rev. Lett.*, 82(8):1668–1671, 1999.

[53] A. Jullien, T. Pfeifer, MJ Abel, PM Nagel, MJ Bell, DM Neumark, and SR Leone. Ionization phase-match gating for wavelength-tunable isolated attosecond pulse generation. *Appl. Phys. B: Lasers and Optics*, 93(2):433–442, 2008.

[54] V.S. Yakovlev and A. Scrinzi. High harmonic imaging of few-cycle laser pulses. *Phys. Rev. Lett.*, 91(15):153901, 2003.

[55] L.E. Chipperfield et al. The generation and utilisation of half-cycle cut-offs in high harmonic spectra. *Laser & Photonics Reviews*, ?:?, 2009. doi: 10.1002/lpor.200900028. URL `http://dx.doi.org/10.1002/lpor.200900028`.

[56] M.J. Abel, T. Pfeifer, P.M. Nagel, W. Boutu, M.J. Bell, C.P. Steiner, D.M. Neumark, and S.R. Leone. Isolated attosecond pulses from ionization gating of high-harmonic emission. *Chem. Phys.*, 366(1-3):9–14, 2009.

[57] National Instruments Corporation. Labview ni 11500 n mopac expwy, 11500 n mopac expwy. URL `http://www.ni.com/`.

[58] Mikhail Polyanskiy. Refractive index database. URL `http://refractiveindex.info/`.

[59] Lawrence Berkeley Laboratory. Atomic scattering factors. URL `http://henke.lbl.gov/optical_constants/`.

[60] NIST. Periodic system. *National Institute of Standards and Technology, Gaithersburg, MD.* URL `http://www.nist.gov/physlab/index.cfm`.

[61] Femtolasers Produktions GmbH. Fernkorngasse 10, 1100 Vienna. *URL http://www.femtolasers. com*, 18, .

[62] Coherent (Deutschland) GmbH. Dieselstraße 5 b, 64807 dieburg, . URL `http://www.coherent.de/`.

[63] INC. PHOTONICS INDUSTRIES INTERNATIONAL. 390 central avenue, bohemia, ny 11716, usa. URL `http://www.photonix.com/`.

[64] Menlo Systems GmbH. Am klopferspitz 19, d-82152 martinsried, . URL `http://www.menlosystems.com`.

[65] Princeton Instruments New Jersey. 3660 quakerbridge road, trenton, nj 08619 usa. URL `http://www.princetoninstruments.com`.

[66] A. Zair, M. Holler, A. Guandalini, F. Schapper, J. Biegert, L. Gallmann, U. Keller, AS Wyatt, A. Monmayrant, IA Walmsley, et al. Quantum path interferences in high-order harmonic generation. *Phys. Rev. Lett.*, 100(14):143902, 2008.

[67] T. Pfeifer, M.J. Abel, P.M. Nagel, A. Jullien, Z.H. Loh, M. Justine Bell, D.M. Neumark, and S.R. Leone. Time-resolved spectroscopy of attosecond quantum dynamics. *Chem. Phys. lett.*, 463(1-3):11–24, 2008.

A Measurements used - Overview

Date	Measurement	Figures
2010-03-31	CEP- and pressure-scan z unknown	6.1; 7.3(a); 8.6(blue points); 8.7(blue points); 8.12; 8.14; 8.15; 8.16
2010-04-01	pressure-scan z unknown	7.2
2010-04-28	CEP- and z-scan at 100 mbar neon	7.4(black points); 8.8(black points); 8.9(black points) 8.10(black points);
2010-04-29	CEP- z-scan at 60 and 100 mbar neon	7.4(red and black points); 8.1; 8.2; 8.8(red and blue points); 8.9(blue points), 8.10(red and blue points)
2010-04-30	z-scan with 100 mbar neon and stable CEP at 0 rad	7.1
2010-05-03	CEP- and pressure scan at z=6 mm in front of the focus	7.3(b); 8.3; 8.5; 8.6(black points); 8.7(black points); 8.11
2010-05-04	CEP-and pressure scan at z=3.75 mm in front of the focus	7.3(c); 8.6(red points); 8.7(red points); 8.17

Figure A.1: Overview over all measurements shown within this work.

B Acknowledgements

At this point I would like to thank all people who helped and supported me during my studies and the work on this thesis. I especially owe thanks to:

- **Dr. Thomas Pfeifer** for offering me the opportunity to be a part of his InterAtto group and introducing me to the fascinating field of high-harmonic generation and attosecond spectroscopy. I would like to thank him for always being there and spending time to patiently discuss problems. He taught me so much during the last year.
- **Christian Ott** for all his patience and support, especially for practical advice in the lab, for the programming of the simulation and for the program that was used to design the new parts for our setup.
- **Robert Heck, Martin Laux, Anja Marschar, Yogesh Patil, Philipp Raith** and **Iris Schlegel** for all the fruitful discussions and for the nice time we had during the last year in the lab, the office and even besides the physics.
- **Vanessa Bangert, Simone Kulikowski** and **Julia Will** for proofreading this thesis in regard to my English.
- **Prof. Joachim Ullrich** for spending time being the secondary reviewer for this work.
- to all members and friends of the Ullrich group and the whole institute for the great working atmosphere that made it easy to enjoy the work every day.
- all my friends and my girlfriend **Silvia Hofheinz** supporting me during my studies and giving some distraction in stressful times.
- **Michael Schneider** from Vienna and **Christian Thome** from Saarbrücken for very helpful discussions.

Finally and exceptionally, I want to thank my family for their support during my studies. My studies would not have been possible without their help.

Erklärung:

Ich versichere, dass ich diese Arbeit selbstständig verfasst habe und keine anderen als die angegebenen Quellen und Hilfsmittel benutzt habe.

Heidelberg, den 04.09.2010 ....